Carnegie Mellon University

CARNEGIE INSTITUTE OF TECHNOLOGY

THESIS

SUBMITTED IN PARTIAL FULFILLMENT OF THE REQUIREMENTS

FOR THE DEGREE OF Doctor of Philosophy

TITLE

TUNING NEAR FIELD RADIATION BY NANOPHOTONICS MATERIALS

PRESENTED BY **JIAWEI SHI**

ACCEPTED BY THE DEPARTMENT OF

MECHANICAL ENGINEERING

_____ _____

ADVISOR, MAJOR PROFESSOR DATE

_____ _____

DEPARTMENT HEAD DATE

APPROVED BY THE COLLEGE COUNCIL

_____ _____

DEAN DATE

TUNING NEAR FIELD RADIATION BY NANOPHOTONIC MATERIALS

Submitted in partial fulfillment of the requirements for

the degree of

Doctor of Philosophy

in

Mechanical Engineering

Jiawei Shi

B.S., Optical Information Science and Technology, Northwestern Polytechnical University, 2009

M.S., Optical Engineering, Huazhong University of Science and Technology, 2011

Carnegie Mellon University

Pittsburgh, Pennsylvania

April, 2015

ACKNOWLEDGEMENTS

Sitting at the Chicago O'Hare International Airport, I'm waiting for the flight back to Pittsburgh. It is such a coincidence that, four years ago, it is right at this airport that I first landed on this country and started my journey as a PhD student at CMU. Making a connection at the same airport at this graduating season, it reminds me of all these colorful experiences in US, in CMU. And, I have so many people and things to acknowledge at this special moment.

First, of course, I'd like to thank my PhD advisor Professor Sheng Shen for his careful guidance both on research and life. I benefit so much from the discussion with him and his encouragement, which helped me come over lots of obstacles in pursuing research goals. As one of his first class students, I have this special honor to witness how he led us to start the research at CMU from only two empty lab benches, which is such a precious and encouraging memory. Studying and researching in Professor Shen's group is the best education that I received at CMU. And, Professor Shen also serves as the chair of my committee. He spent so much time and energy on me from the very beginning to the very end! A simple thank you can never express my great appreciation to him. He told me that the best way to appreciate is to do a good job in my future career. And, I will always try!

I also would like to thank all my lab mates and office mates for their companion. I can't list all their names, here are some of them: Pengfei Li, Baoan Liu,

Francisco Ramirez, Kevin Parrish, Wee Liat Ong, Shubhaditya Majumdar, Ivy Yu, Simon Lu, Ankit Jain, Keith Regner, Emrecan Soylemez, Vitali Brand, Zonghui Su, Justin Freedman, Lien Chin Wei, Seong Jin An, Pratiti Mandal, Siddharth Babu, et al. Lots of them joined the PhD program in the same year as me. We hung out together, took qualify exam together, sit in the same office, and did experiment in the same lab… They are all brilliant and with interestingly different characters, and I learnt a lot from them, having lots of fun!

Using this opportunity, I also would like to thank other three professors in my committee. They are Professor Shi-Chune Yao, Professor Alan McGaughey, Professor Robert Davis. It is my great honor to have them on my committee. Here, I have a small story for each of them:

I knew Professor Yao from the heat transfer class. There is no need to mention how awesome his lecture is. I'd like to tell a small story. In the week of the final exam, I suffered from appendicitis and was at hospital, so I wrote him an email. Professor Yao replied very soon and told me to take as long time as I needed to recover and don't worry about the exam. After I went out of the hospital, he arranged me a makeup exam and let me take the exam in his warm and spacious office. He asked my recovery and encouraged me to struggle through. All these happened in my first winter at Pittsburgh. His kindness and smile will always be deeply in my heart and encourage me! Professor Yao also served as the committee member for my PhD qualify exam, it is my great honor to always have him witness my important moments at CMU.

Professor Alan McGaughey is an expert in nanoscale transport phenomena. Moreover, from the mouth of his students, I know that he is a world class human being. I will always remember one scene about Alan in a shiny summer afternoon. I was sitting beside the bench in Schenley Park, feeling pretty low for something. When I raised my head, I saw Alan walking down the trail toward my direction. Right then, the sun shines onto his face, together with his fast gait, it makes him look so energetic! I don't know why I was so encouraged by this scene, but it did!

Professor Robert Davis is a famous and highly respected material scientist. I first knew him because I wanted to use the Hall Effect measurement in his lab. After nervously knocking on his door, it turns out that he is unexpectedly friendly. After a brief talk, he not only allowed me to use that equipment, but also gave me advices on how to carry out an accurate measurement. As a member of the academy of engineering, his willingness to help an unknown graduate student deeply affected me and set a great example for us all!

I also would like to thank my landlord Bob and my neighbors: Patrick, Eric, Mike and Audrey! With Bob, I don't need to buy breakfast myself. He always bought orange juice and croissant from the Sam's club. Every time when I travel, he will always drive me to the airport and pick me up. I remember one time he got up at 4:00 am in order to give me a ride. With his help, my spoken English also improved a lot! It is a great experience to live in the Edgewood borough!

The deepest appreciation goes to my dear parents and my dear girlfriend. My

family locates in a small, quiet and beautiful village in the eastern part of China, with lots of rivers passing by. After I studied and traveled lots of cities, objectively speaking, my home town is the most beautiful and most livable place I've ever been. I'm so lucky to start the earliest memories in such a beautiful place! I'm the only kid of my parents, with the privilege to enjoy all their loves. Although they earn very low salaries, they worked so hard to put me through college and support me all the way through! One of the happiest times every week is to have video talks with them through QQ. My girlfriend Xin and I met right on the CMU campus. I don't know why it always feels so comfortable being together with her. Although she is younger than me, she is more mentally mature. Without her support, tolerance and encouragement, I cannot insist to this point. I'm really lucky to have her in my life!

My Ph.D. program has been funded by the Dean's fellowship, Professor Shen's start-up and the funding from the National Science Foundation and Defense Advanced Research Projects Agency.

ABSTRACT

TUNING NEAR RADIATION BY NANOPHOTONIC MATERIALS

by

Jiawei Shi

Chair: Sheng Shen

Although blackbody radiation described by Planck's law is commonly regarded as the maximum of thermal radiation, thermal energy transfer in the near-field can exceed the blackbody limit due to the contribution from evanescent waves. This novel thermal transport mechanism has important practical implications in a variety of technologies, e.g., thermophotovoltaic energy conversion, radiative cooling, thermal infrared imaging, and heat assisted magnetic recording. In recent years, the underlying physics of this phenomenon has been actively investigated, however, on the experiment side, there is limited progress except several initial demonstrations.

During my time as a graduate student, I've been focusing on realizing the tuning of the near field radiation experimentally by adjusting the optical properties of materials. For the first project, I investigated theoretically and experimentally the near field radiation properties of doped silicon at different doping concentrations, which provides a scheme for tuning near field radiation. In the second project, the near field

radiation properties of hyperbolic metamaterials are investigated. Hyperbolic metamaterials is demonstrated to work as a broad band thermal extractor. At the same gap between an emitter and an absorber, the near field radiation can be enhanced by around one order of magnitude with the thermal extractor added in between. For the third project, the near field radiation properties of ultrathin metallic films are investigated. It is demonstrated both theoretically and experimentally that the near field radiation from metallic films on top of silicon substrate can be tuned to different intensities by changing the thickness of the metallic films. This phenomenon can be explained by the special surface plasmon mode along the thin metallic film and the screening effect of metals.

TABLE OF CONTENTS

LIST OF TABLES

LIST OF FIGURES

NOMENCLATURE

ε	electric permittivity
μ	magnetic permeability
D	electric displacement
B	magnetic field
E	electric field
J	current density
c	speed of light in vacuum
k	wave vector
t	time
ω	radial frequency
K	in-plane component of the wave vector
γ	wave vector component normal to the interface
λ	wavelength
τ	scattering time
h	Planck constant
k_B	Boltzmann constant
E_F	Fermi energy
T	temperature
S	Poynting vector
G	near field radiative conductance
ΔT	temperature difference
n	electron density

p	hole density
ρ	charge density
d	distance
r	radius
h	heat transfer coefficient
u	displacement of atoms from equilibrium position
m	atom weight
w	line width
e	line width
m_e	effective mass of electrons
m_h	effective mass of holes

Abbreviations

CMP	chemical mechanical planarization
SEM	scanning electron microscope
AFM	atomic force microscope
MWAs	metal wires arrays
SiC	truncated Callaway
MEMS	microelectromechanical systems
LHS	left hand side
SiNx	silicon nitride
LDOS	local density of states
PLDOS	photon local density of states
VO2	vanadium oxide
HMs	hyperbolic metamaterials

AAO	anodic aluminum oxide
LOCOS	local oxidation of silicon
ILD	interlayer dielectrics
STI	shallow trench isolation
RIE	reactive ion etching
GUI	graphic user interface
ICP	inductively coupled plasma
NFRHT	near field radiative heat transfer
IMI	insulator/metal/insulator
MIM	metal/insulator/metal
EBPVD	Electron beam physical vapor deposition
ALD	atomic layer deposition
BOE	buffered oxide etching
HF	hydrogen fluoride
DGF	dyadic Green’s function

CHAPTERS

1 Theoretical foundation of near field radiation

1.1 Overview

As one of the basic modes of heat transfer, thermal radiation is ubiquitous: any object with a temperature higher than 0 K radiates electromagnetic waves to the surrounding environment[1]. For example, human body radiates electromagnetic waves that are mainly in the infrared range. This is why an infrared camera can capture the human body image even at night. The origination of thermal radiation is attributed to the thermal oscillation of the charged particles inside the materials. For instance, there are electrons in metals and ions in dielectrics. As long as the temperature of the material is not absolute 0 K, those charged particles will inevitably experience thermal oscillations, which emit electromagnetic waves. So, thermal radiation is essentially a collection of electromagnetic waves with different wavelengths. Also, the radiation spectrum is determined by the temperature of the object as well as the properties of the composing materials[2]–[4] .

Depending on the distance between two interacting bodies, thermal radiation can be categorized into two types: one is the far field thermal radiation; the other is the near field radiation[5]. When the distance between two objects is much larger than the characteristic wavelength of the thermal radiation, the radiation falls into the far field

range, within which the Planck's blackbody radiation law and Wien's displacement law work pretty well. As shown by Figure 1.1 (a), in the far field when the incident angle of the light is smaller than the critical angle, partial reflection and partial reflection will happen across the interface. The transmitted light is able to propagate through the gap and reach the opposing body. When the incident angle is larger than the critical angle, the total reflection occurs. As we know, for the total reflection, electromagnetic waves exist in the form of evanescent waves across the gap between the two bodies, which decays exponentially from the interface. The decay length of the evanescent wave is comparable to the characteristic wave length of the radiation. In the far-field, the characteristic wavelength is much smaller than the distance between two interacting objects, so the evanescent waves cannot contribute to the radiative heat exchange between two bodies. In comparison, as shown in Figure 1.1 (b), when the distance between two objects is comparable or even smaller than the distance between the two objects, the evanescent waves from the total reflection is able to reach the opposing object before getting totally attenuated, so that evanescent waves are also making huge contributions to the radiative heat transfer between two interacting objects. Since Planck's law does not consider the contribution from evanescent waves, it cannot deal with the radiation problems in the near field range. When it comes to the near field radiation, it is necessary to introduce different tools and methods.

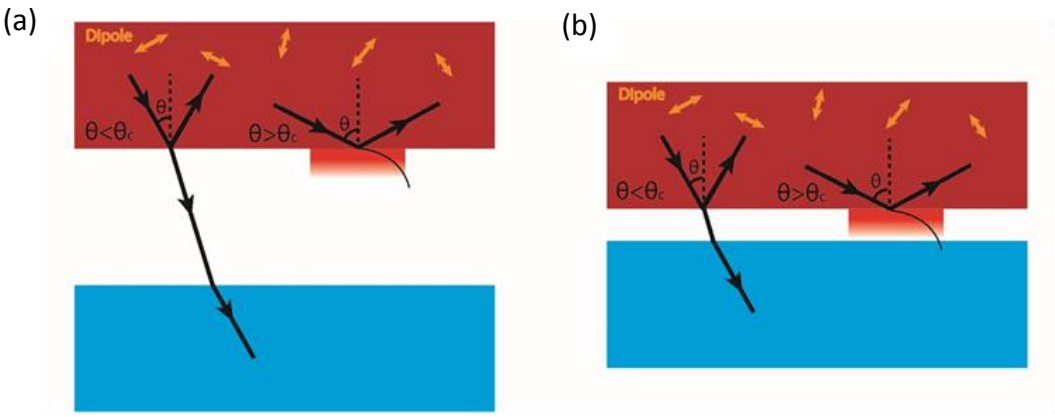

Figure 1.1: (a) Far field thermal radiation when the distance between two objects is much larger than the central wavelength of the thermal radiation. (b) Near field thermal radiation when the distance between two objects is comparable or even smaller than the central wavelength of the thermal radiation.

1.2 Electromagnetic surface waves

Electromagnetic surface waves are hybrid waves that propagate along the interface and decay exponentially from the interface in the vertical direction. There are mainly two types of electromagnetic surface waves: one is the surface plasmon polaritons, the other is the surface phonon polaritons[6][7]. Surface plasmon polaritons are due to the coupling between the electromagnetic wave and the charge oscillations along the interface, which usually exists on the metal surface[8]–[10]. Surface phonon polaritons are due to the coupling between electromagnetic waves and optical phonons, which usually exists on the surface of polar dielectrics, such as SiO_2, SiC[11].

To better explain the origin and properties of those electromagnetic surface waves,

let's first start with the Maxwell equations in the frequency domain[12]–[14]:

$$\nabla \times \vec{E}(\vec{r},\omega) = i\omega\vec{B}(\vec{r},\omega) \quad [1]$$

$$\nabla \times \vec{H}(\vec{r},\omega) = -i\omega\vec{D}(\vec{r},\omega) + \vec{J}(\vec{r},\omega) \quad [2]$$

$$\nabla \cdot \vec{D}(\vec{r},\omega) = \rho \quad [3]$$

$$\nabla \cdot \vec{B}(\vec{r},\omega) = 0 \quad [4]$$

Where $\vec{E}$ is the electric field, $\vec{H}$ is the magnetic field, $\vec{D}$ is the electric displacement, $\vec{B}$ is the magnetic flux density, $\vec{J}$ is the current density, ρ is the charge density. By taking curl on both sides of equation [1], we can get the so called Helmholtz equation

$$\nabla^2\vec{E} + k^2\vec{E} = 0 \quad [5]$$

The Helmholtz equation can serve as the governing equation for the electric field. Combined with boundary conditions, we can solve the electric field. From the electric field, using Equation [2] we can calculate the magnetic field. Here, the boundary conditions for the electromagnetic field in the vector form are[12]:

$$\overrightarrow{D_1} \cdot \vec{n} - \overrightarrow{D_2} \cdot \vec{n} = \rho_s \quad [6]$$

$$\vec{n} \times \overrightarrow{E_1} - \vec{n} \times \overrightarrow{E_2} = 0 \quad [7]$$

$$\overrightarrow{B_1} \cdot \vec{n} - \overrightarrow{B_2} \cdot \vec{n} = 0 \quad [8]$$

$$\vec{n} \times \overrightarrow{H_1} - \vec{n} \times \overrightarrow{H_2} = \vec{J} \quad [9]$$

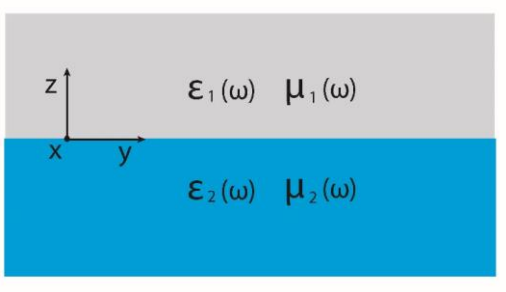

Figure 1.2: Two different mediums separated by a plane interface. The coordinate and the electrical and magnetic properties are used in the derivation.

As shown in Figure 1.2, let's explore the properties of surface wave from the case of a plane interface separating two different mediums with dielectric constant of ε_1, ε_1, and magnetic constant of μ_1, μ_2. The base of the Cartesian coordinate is denoted by three vectors $\vec{x}$, $\vec{y}$ and $\vec{z}$. Any point in the plane can be represented as $\vec{r} = y\vec{y} + z\vec{z} = (\vec{R},\ \gamma)$, where $\vec{R} = y\vec{y}$. Correspondingly, the wave vector can be denoted as $\vec{k} = k_y\vec{y} + k_z\vec{z} = (\vec{K},\ \gamma)$, where $\vec{K} = k_y\vec{y}$. Since the surface wave is a special form of electromagnetic wave, it should be a particular solution of Maxwell's equations. To satisfy the equation [5], the electric field in both media should be cast in the form[12] [13]

$$\overrightarrow{E_1}(\vec{r},\omega) = \begin{pmatrix} E_{x,1} \\ E_{y,1} \\ E_{z,1} \end{pmatrix} exp[i(\vec{K}\cdot\vec{R} + \gamma_1 z)\ ] \qquad [10]$$

$$\overrightarrow{E_2}(\vec{r},\omega) = \begin{pmatrix} E_{x,2} \\ E_{y,2} \\ E_{z,2} \end{pmatrix} exp[i(\vec{K}\cdot\vec{R} + \gamma_2 z)\ ] \qquad [11]$$

where $\gamma_1^2 = \varepsilon_1\mu_1 k_0^2 - K^2$ and $\gamma_2^2 = \varepsilon_2\mu_2 k_0^2 - K^2$

Now let's analyze the electric field by polarization: s (TE) and p (TM) polarization. For TE mode, the electric field has the forms on both sides of the interface:

$$\overrightarrow{E^{TE}}(\vec{r},\omega) = \begin{pmatrix} E_x \\ 0 \\ 0 \end{pmatrix} exp[i(\vec{K}\cdot\vec{R} + \gamma z)\,] \quad [12]$$

$$\overrightarrow{E^{TM}}(\vec{r},\omega) = \begin{pmatrix} 0 \\ E_y \\ E_z \end{pmatrix} exp[i(\vec{K}\cdot\vec{R} + \gamma z)\,] \quad [13]$$

According to the boundary conditions listed in equation [6] and [7], as well as equation [3], we can obtain the following equation for s polarization.

$$\mu_1\gamma_2 + \mu_2\gamma_1 = 0 \quad [14]$$

Correspondingly, we can have a similar equation to p polarization

$$\varepsilon_1\gamma_2 + \varepsilon_2\gamma_1 = 0 \quad [15]$$

For non-magnetic materials ($\mu = 0$), since γ and $Im(\gamma)$ are always positive, equation [13] can't be satisfied. In other words, there exists no surface wave with s polarization. In comparison, because the electric permittivity ε_1 and ε_2 can be negative, equation [14] can still be satisfied. So, we come to an important conclusion: electromagnetic surface waves exist in the form of p polarization. Here is the dispersion relation for p-polarization.

$$K^2 = \frac{\omega^2}{c^2}\frac{\varepsilon_1\varepsilon_2[\varepsilon_2\mu_1 - \varepsilon_1\mu_2]}{\varepsilon_2^2 - \varepsilon_1^2} \quad [16]$$

In the case of $\mu_1 = \mu_2 = 1$ and $\varepsilon_1 = 1$, equation [16] becomes

$$K = \frac{\omega}{c}\sqrt{\frac{\varepsilon_2(\omega)}{\varepsilon_2(\omega)+1}} \qquad [17]$$

For frequencies that satisfy $\varepsilon_2(\omega)+1=0$, K will become very large. This corresponds to the excitation of surface waves. Taking the vacuum-medium interface as an example, in order to excite surface waves, there are two basic conditions that need to be met: (1) For the excitation wave, the wave vector must be very large. (2) For the medium property, the electric permittivity needs to be around -1 at certain frequencies. The dielectric function of different materials will be discussed in detail in chapter 3.

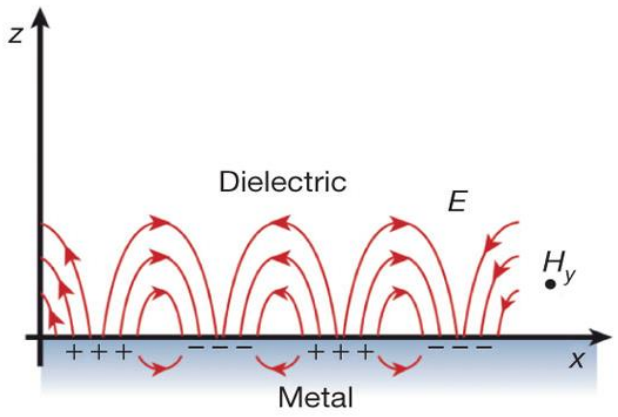

Figure 1.3: Schematic of surface plasma polaritons. This is due to the coupling between electromagnetic waves and surface electron oscillation[15].

1.3 Methods for calculating the near field radiation

1.3.1 Fluctuation dissipation theorem

Inside materials at certain temperature, the charges such as electrons, ions are

undergoing random oscillations. Those random oscillations can be treated as random current sources, which will radiate electromagnetic waves to the surrounding environment. In order to calculate this spontaneous radiation attributed to random current sources, two basic problems need to be solved: one is the statistical properties of the random current sources; the other is the radiation properties dictated by the specific macroscopic structure of the bulk.

The fluctuation dissipation theorem solves the first problem by giving the correlation between current sources[3][16]–[18]:

$$\langle j_k(\vec{r},\omega) j_l^*(\vec{r}',\omega')\rangle = \frac{2\omega}{\pi}\varepsilon_0\varepsilon''(\omega)\Theta(\omega,T)\delta(\vec{r}-\vec{r}')\delta_{kl}\delta(\omega-\omega') \quad [18]$$

$$\Theta(\omega,T) = \hbar\omega\left(\frac{1}{2}+\frac{1}{exp(\hbar\omega/k_BT-1)}\right) \quad [19]$$

The angle bracket $\langle\ \rangle$ denotes the statistical ensemble average, $\Theta(\omega,T)$ denotes the mean energy of an oscillator in thermal equilibrium at temperature T and ε'' is the imaginary part of the dielectric constant ε. $\delta_{kl}$is the Kronecker delta function, which indicates that different components of the current source are independent from each other. $\delta(\vec{r}-\vec{r}')$ and $\delta(\omega-\omega')$ are Dirac delta functions.

1.3.2 Dyadic Green's function for electrodynamics

In classical electrodynamics, the dyadic Green's function serves as the linear coefficient connecting the source and the field. The following two equations give the definitions of two different dyadic Green's tensors:

$$\vec{E}(\vec{r},\omega) = i\mu_0\omega \int d^3\vec{r}'\, \overleftrightarrow{G}^{EE}(\vec{r},\vec{r}',\omega)\vec{j}(\vec{r}',\omega) \quad [20]$$

$$\vec{H}(\vec{r},\omega) = \int d^3\,\vec{r}'\overleftrightarrow{G}^{HE}(\vec{r},\vec{r}',\omega)\vec{j}(\vec{r}',\omega) \quad [21]$$

Green's function of several simple structures can be found in analytical form. The magnetic field can be easily calculated from the electric field.

1.3.3 Electromagnetic energy density

The electromagnetic energy density is the sum the electric energy density and the magnetic energy density, which can be calculated by this formula[13]:

$$\langle U(\vec{r},\omega)\rangle = \frac{\varepsilon_0}{2}\langle\left|\vec{E}(\vec{r},\omega)\right|^2\rangle + \langle\left|\vec{H}(\vec{r},\omega)\right|^2\rangle \quad [22]$$

$\vec{\mathrm{E}}(\vec{\mathrm{r}},\mathrm{t})$ and $\vec{\mathrm{H}}(\vec{\mathrm{r}},\mathrm{t})$ in the above equation can all be calculated by using Equation [20] and [21]. Using the fluctuation dissipation theorem, we can calculate the energy density from the trace of the dyadic Green's function[3]:

$$U(\vec{r},\omega) = \frac{\hbar\omega}{exp(\hbar\omega/k_BT)-1}\frac{\omega}{\pi c^2}\,\mathrm{ImTr}\left[\overleftrightarrow{G}^{EE}(\vec{r},\vec{r},\omega) + \overleftrightarrow{G}^{HH}(\vec{r},\vec{r},\omega)\right] \quad [23]$$

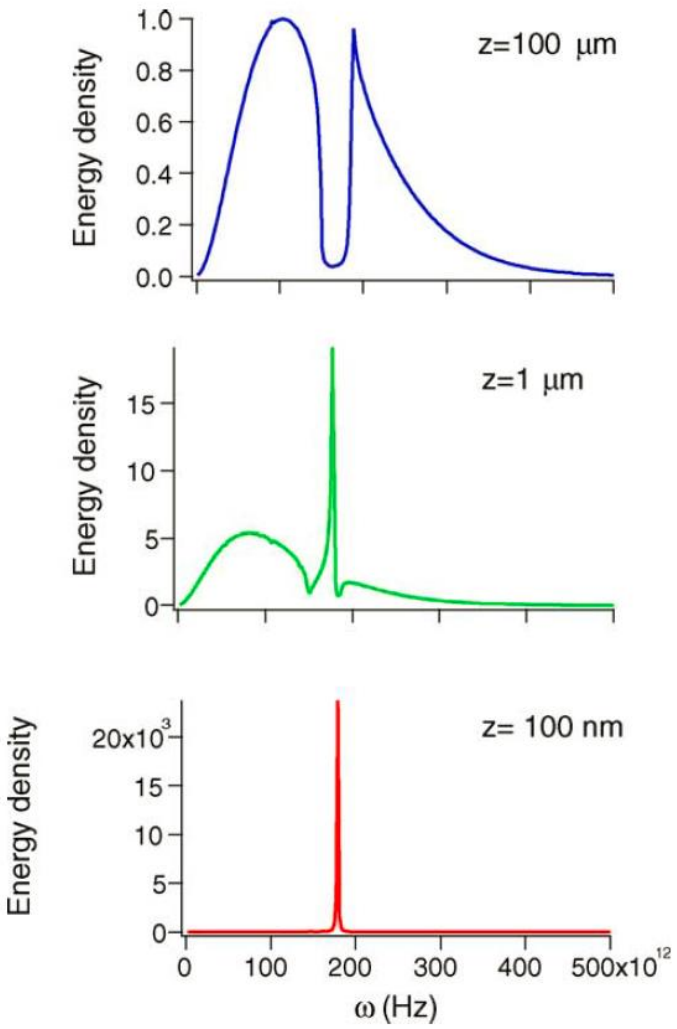

Figure 1.4: Electromagnetic energy density at different distance from the interface [3].

1.3.4 Local density of states

In solid state and condensed matter physics, density of states (DOS) is a very fundamental and a well-defined concept[19]. For a non-uniform system, the concept of local density of states (LDOS) is introduced[20]. For our discussion, let's first get a clear definition of the LDOS in electrodynamics.

$$U(\vec{r},\omega) = \rho(\vec{r},\omega)\frac{\hbar\omega}{exp(\hbar\omega/k_BT)-1} \quad [24]$$

where $U(\vec{r},\omega)$ is the local density of electromagnetic energy at a given point $\vec{r}$, $\rho(\vec{r},\omega)$ denotes the LDOS at point $\vec{r}$. The rest part is the mean energy of each state at temperature T. From this equation, we can see that the energy density is the product between the LDOS and the mean energy at that state.

$$\rho(\vec{r},\omega) = \frac{\omega}{\pi c^2}\mathrm{ImTr}\left[\overleftrightarrow{G}^{EE}(\vec{r},\vec{r},\omega) + \overleftrightarrow{G}^{HH}(\vec{r},\vec{r},\omega)\right] \quad [25]$$

1.3.5 Thermal emission from a planar interface

For the structure shown in figure 1.1, the radiation from the material in the bottom half space can be calculated through the Poynting vector $\vec{S} = \vec{E} \times \vec{H}$. For electromagnetic waves at certain frequency, the time average of the Poynting vector can be calculated by[13]

$$\vec{S}(\vec{r},\omega) = \frac{1}{2}Re\left(\vec{E}(\vec{r},\omega) \times \vec{H}(\vec{r},\omega)\right) \quad [26]$$

To calculate the value of the $\vec{S}$ from the above equation, we need to first know the values of $\vec{E}(\vec{r},\omega)$ and $\vec{H}(\vec{r},\omega)$. Plugging equations [20] and [21] into Equation [26], we can get

$$\begin{aligned}&\langle E_i(\vec{r},\omega)H_j^*(\vec{r},\omega)\rangle \\ &= \langle i\mu_0\omega \int G_{ik}^{EE}(\vec{r},\vec{r}')G_{jl}^{HE}(\vec{r},\vec{r}'')j_k(\vec{r}',\omega)j_l^*(\vec{r}'',\omega)d^3\vec{r}'d^3\vec{r}''\rangle\end{aligned} \quad [27]$$

Then, by plugging equation [18] into the previous formula, we can get

$$\langle E_i(\vec{r},\omega)H_j^*(\vec{r},\omega)\rangle = \frac{i\Theta(\omega,T)\omega^2}{\pi c^2}\int \varepsilon''(\vec{r}')G_{ik}^{EE}(\vec{r},\vec{r}')G_{jk}^{HE}(\vec{r},\vec{r}')d^3\vec{r}' \qquad [28]$$

In this way, we have got the general expression of the radiation flux from a plane interface separating the material and the vacuum.

1.3.6 The Derjaguin approximation

In chapter 2, the experiment setup that we built is based on a sphere-plate geometry. In order to use the previously introduced method for calculating parallel plates, Derjaguin approximation is applied to discretize the spherical surface to a set of rings, as shown in Figure 1.5.

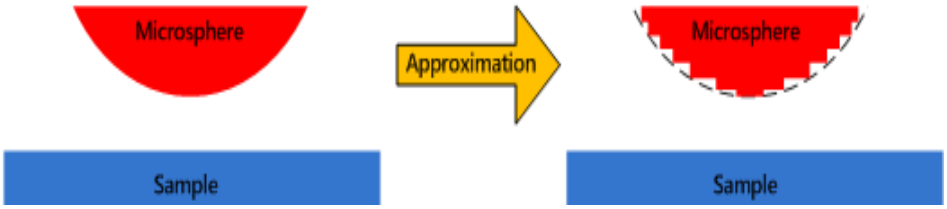

Figure 1.5: The side view of the Derjaguin approximation, in which the spherical surface is discretized into a set of rings.

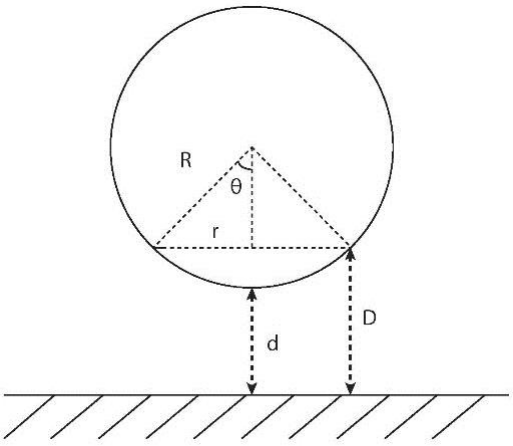

Figure 1.6: Cross section of the sphere-plate geometry. The parameters used in equation [29] are all marked in this schematic.

G is used to denote the thermal conductance between the sphere and the plate. *h(x)* is used to denote the radiative heat transfer coefficient between two parallel plate with a separating distance of x. A schematic is drawn for the clarity of discussion (Figure 1.6), R represents the diameter of the sphere, *d* represents the distance between the bottom of sphere and the plate, *r* represents the radius of a randomly chosen ring. D represents the distance from the plate to the ring with a radius of *r*. Derjaguin approximation[21] is carried by use of the following equation:

$$G = \int_0^R h(D)\, 2\pi r dr = \int_0^R h(d + R - \sqrt{R^2 - r^2})\, 2\pi r dr \qquad [29]$$

In summary, there are two major steps of calculating the radiative thermal conductance between the microsphere and the plate: (1) calculate the variation of *h* versus gap size (2) plug the *h* values to carry out the Derjaguin approximation.

1.4 Summary

In this chapter, I introduce the basic theoretical foundation for near field radiation. I start from the basic concept of thermal radiation, which is later divided into two major categories: one is far field thermal radiation, the other is the near field thermal radiation. In order to better explain the concept of near field radiation, the concept of surface wave is introduced by use of basic classical electromagnetic theory. From the

dispersion relation of the surface waves, it becomes clear that there exists a type of electromagnetic wave that is evanescent on both sides of the interface, which contributes to the near field radiation. In order to quantitatively describe properties of the near field radiation, dyadic Green's function and the fluctuation dissipation theorem are applied to calculate the electromagnetic field near the surface of the material. The concept of LDOS is also introduced to quantify the energy density. Based on those foundations, the radiation emission from a semi-infinite structure is calculated. In the end, in order to connect the parallel plate geometry with the sphere plate geometry, the Derjaguin approximation is introduced in detail.

2 Experiment techniques

As introduced in the first chapter, researchers have carried out extensive theoretical work to study the near field radiation between two bodies with different material properties and geometries. Similarly, on the experiment side, significant progress has been made in the past decades. Many advanced experiment techniques have been developed to measure the near field radiation between different materials with different geometries. At this stage, the technique for measuring the near field radiation has become more and more mature. Researchers are taking one step further to tune or even to control the intensity of the near field radiation. During my PhD research, I set up an experiment system for near field radiation measurement. This system makes full use of a bi-material cantilever technology, which is extremely sensitive to heat transfer.

The aim of this chapter is to give a brief overview of the near field radiation experiment techniques as well as the recent progress on experimentally tuning the near field radiation. Then, I'll introduce in detail the near field radiation measurement technology that I've been working on during the past several years.

2.1 Brief review of experiment techniques

In order to investigate the near field radiation, one of the most important procedures is to create nano scale or micro scale gaps between two objects. There are mainly two geometries that are used to realize such gaps: one is the sphere-plate

geometry, the other is the parallel plate geometry. Our experiment setup is based on the sphere-plate geometry. Compared with the parallel plate geometry, it is much easier to maintain nanoscale gaps using the sphere-plate structure. On the other side, parallel plate geometry might have more significance in terms of real applications, since it might directly lead to the fabrication of near field heat transfer devices with large areas. So, although it is very challenging to maintain two parallel plates at very small gaps, researchers have successfully developed several setups based on this geometry. In the following two sections, I'm going to give a brief introduction to some representative experimental works based on those two geometries respectively.

2.1.1 Experiment setups bases on parallel plate geometry

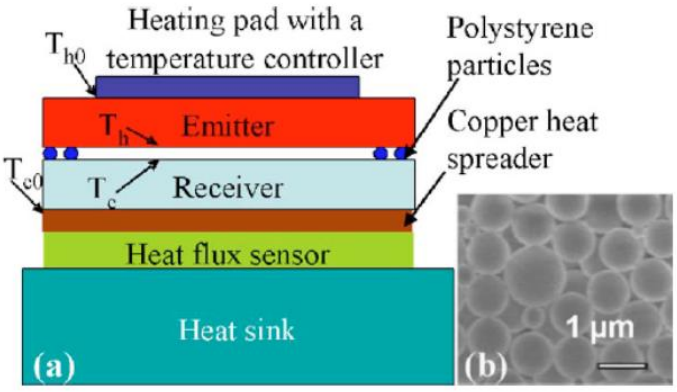

Figure 2.1: The schematic of the experiment setup built by Hu et al. Polystyrene particles with a diameter of ~ 1μm were used to separate two glass plates at micron scale gaps [22].

Hu et al. carried out the near field radiation measurement based on a structure of two parallel glass plates (as shown in Figure 2.1)[22]. Polystyrene particles with an

average diameter of ~ 1μm were used to separate two glass plates at micron scale gaps. Since the thermal conductivity of the polystyrene is very low, they assume its contribution to the heat transfer process is negligible and the near field radiation process dominates. Heating pad with a temperature controller is put on top of the hot plate. The temperature of the hot pad is then monitored using a platinum resistance temperature detector. Using this feedback controlling, the authors claim that the temperature variation can be controlled within the range of 1ºC. After taking into consideration of the gap size deviation caused by the surface roughness of the plate, the measurement results fit pretty well with theoretical calculation at a gap size of ~1.6 μm. Compared with the sphere plate geometry, although such parallel plates geometry provides no flexibility of adjusting the gap size between the two plates, it does have deep significance of practicality by demonstrating near field radiation enhancement in a very large sample area.

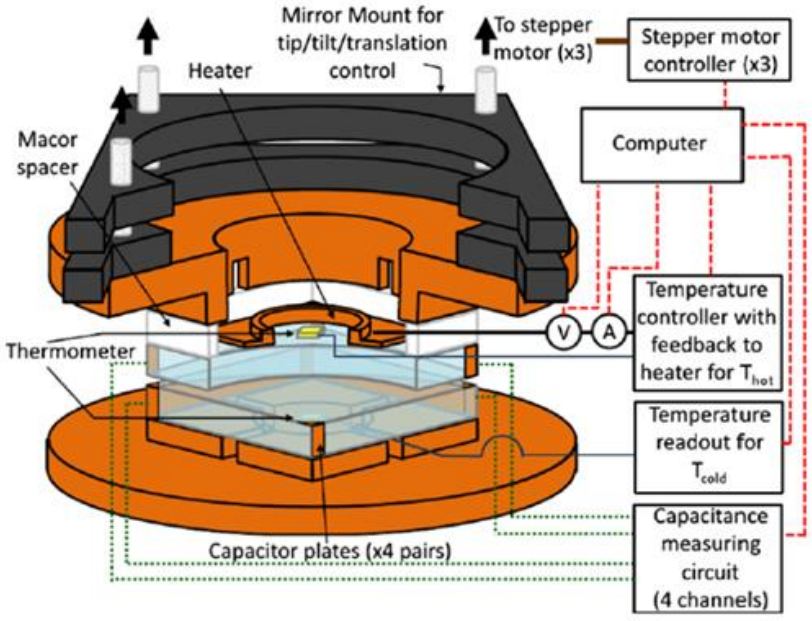

Figure 2.2: The schematic of the experiment setup built by Ottens et al. Two plates made of sapphire are maintained parallel to each other by depositing capacitor films on the four corners of the plate [23].

Similar to Hu et al.'s experiment setup, Ottens et al. carried out a similar near field radiation measurement between two parallel plates (as shown in Figure 2.2)[23]. The two parallel plates have a dimension of 50×50×5 mm^3 and are made of sapphire. Compared with Hu et al.'s setup, this setup has made a major improvement by enabling the continuous variation of the separating gap between the two parallel plates. Instead of sandwiching polystyrene microspheres between the two plates, a pure gap is maintained between the two sapphire plates without the support of any other objects in between the two plates. This is achieved by use of capacitance sensors combined with stepper motors. What they do is to deposit 200 nm thick copper layers on the four corners of the plate, which serve as the electrodes for capacitors. Capacitance measuring circuit is built to monitor the capacitance in real time, and stepper motors allows the adjustment of the gap size as well as the tilting of the plate. Apparently, this experiment setup provides more flexibility compared with the preceding setup by allowing the continuous adjustment of the gap size from 2 μm to 100 μm.

2.1.2 Experiment setups based on sphere-plate geometry

In the section, I'll introduce three most representative near field radiation measurement setups based on sphere-plate geometry. Those experiments will be introduced in an order that will provide a clear thread of the evolvement of the sphere-plate geometry based experiment setups.

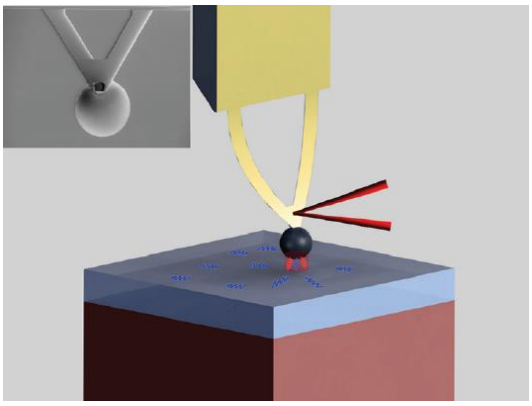

Figure 2.3: The schematic of the experiment setup built by Shen et al. This is a typical setup base on the sphere-plate geometry. A microsphere of 100 μm diameter is attached onto the tip of a triangular shaped cantilever. Both the microsphere and the sample plate are made silicon dioxide[11].

Shen et al. first carried out a robust experiment to demonstrate the surface phonon mediated near field radiation enhancement. As shown in Figure 2.3, their experiment setup is based on a sphere-plate geometry[11]. A microsphere of 100 μm diameter is attached onto the tip of a triangular shaped cantilever. The sample is loaded on a piezoelectric translation stage, which will approach the microsphere in nanometer steps during the measurement. Apparently, such sphere-plate geometry makes it more convenient to achieve a nanoscale gap. In this design, the laser has two important functions: (1) it serves as the light source for the optical deflection system. (2) It is also used to heat up the tip of the cantilever, as well as the microsphere attached onto the tip of the cantilever. Since the experiment setup I built is directly evolved from this setup, the detail of this type of setup will be introduced in detail in section 2.

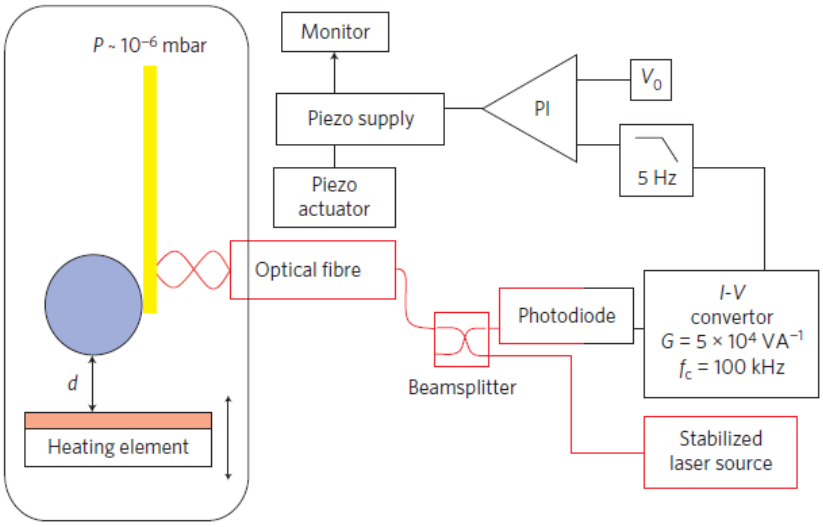

Figure 2.4: The schematic of the experiment setup built by E. Rousseau et al. This setup is extremely similar to the setup shown in Figure **2.3** except two major differences: (1) The sample plate is heated up rather than the microsphere. (2) Instead of using an optical deflection system, they use an optical fiber interferometer to monitor the displacement the cantilever[21].

Similar to Shen et al.'s experiment design, Rousseau et al. also developed a near field radiation measurement setup which makes use of the bi-material effect of the cantilever[21]. Compared with Shen et al.'s design, they made two major improvements: (1) instead of using optical deflection system, they developed a fiber-actuator system to directly measure the deflection of the cantilever. As shown in Figure **2.4**, an optical fiber is used to shine laser on to the tip of the cantilever. And, the reflected laser from the cantilever will couple back into the fiber and form an interference pattern with the original laser. The intensity of the interfered laser pattern will change when the distance between the fiber tip and the cantilever tip variate.

During the measurement, the cantilever will deflect due to the near field radiation, so the distance between the cantilever tip and the fiber tip will change corresponding. Because of the feedback loop in the fiber-actuator system, by keeping the laser power of the interference pattern constant, they are able to control the piezoelectric translation stage to move the same distance as the deflection of the cantilever. In other words, this feedback loop system enables the piezoelectric translation stage to trace the deflection of the cantilever in real time. (2) Instead of heating the tip of cantilever using laser, they choose to heat up the sample. Considering the challenge to maintain a stable incident laser power onto to the cantilever tip, such design will largely make the system adjustment more convenient.

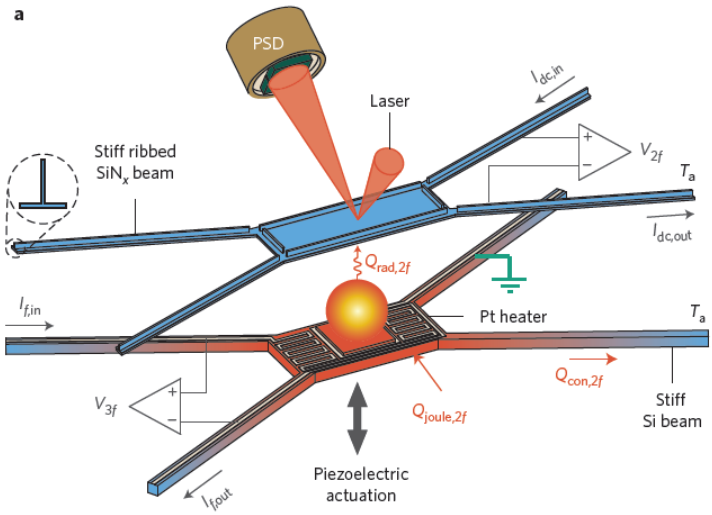

Figure 2.5: The schematic of the experiment setup built by Bai Song et al. The upper plate serves as the receiver; the lower plate serves as the emitter with a microsphere loaded on top of it. The emitter is loaded onto a piezoelectric translation stage to adjust the distance between the emitter and the receiver. A laser beam is shined on to the top

surface of the receiver to detect the collision point between the microsphere and the receiver plate. *This figure is cited from Bai Song et al.'s paper.*[24]

The latest progress on the near field radiation measurement might be Bai Song et al.'s work published 2015[24]. They developed an experimental platform as shown in Figure 2.5 to study the thickness dependence of near field radiation. Their device consists of an emitter and a receiver, which is forms a sphere-plate geometry. The emitter is a microsphere with a diameter of 50 μm, which is attached onto the top of the silicon plate. The silicon plate is suspended through four stiff silicon beams, and a platinum resistance heater-thermometer is fabricated on the silicon plate to heat up the microsphere as well as measure the temperature. The receiver has a similar four beam suspension structure as the heater which is made from SiN_x. A platinum resistance heater-thermometer is also fabricated on the receiver to monitor the temperature variation. The temperature measurement resolution is ~50 μK when modulated at 2 Hz, which makes it capable of detecting heat current as small as ~100 pW. During the measurement, the emitter temperature is sinusoidally modulated at a frequency of 2 Hz. The resulted radiation from the emitter will also oscillate in the same frequency, which will result in temperature oscillation in the opposing receiver. By introducing temperature modulation, they are able to apply lock-in to enhance the temperature resolution, which is one great improvement compared with previously developed experiment setups.

2.1.3 Experiment setups based on integrated nanostructures

The dimension of the preceding two experiment setups are all at macroscopic scale. However, since the near field radiation enhancement happens at nanoscale, it is highly possible that nanoscale radiation will also find its application in integrated nanostructures. Recently, St-Gelais et al. demonstrated for the first time the strong near field radiation enhancement in the integrated nanostructures[25]. As shown in Figure, two parallel nanobeams with a length of 200 μm and a cross section of 500 nm × 1.1 μm are fabricated through multiple steps of nanofabrication. One beam is fixed with a Pt resistor deposited on top of it, which serves as the heater; the other beam is suspended which serves as the cool side. The distance between the nanobeams can be adjusted electrostatically by adjusting the actuating voltage. When gap between the two nanobeams is changed, the temperature of the hot beam and the cool beam will change correspondingly. The temperature of the beams can be calculated from the electrical resistance from the Pt resistor, because the resistance of Pt changes corresponding with the temperature variation. Using this setup, the authors are able to adjust the gap from the initial separation of ~700 nm down to ~200 nm. Such on-chip near field radiation structure might have great potential of application in the development of nanostructure thermal devices, such as thermal rectifier, thermal transistor, and etc.

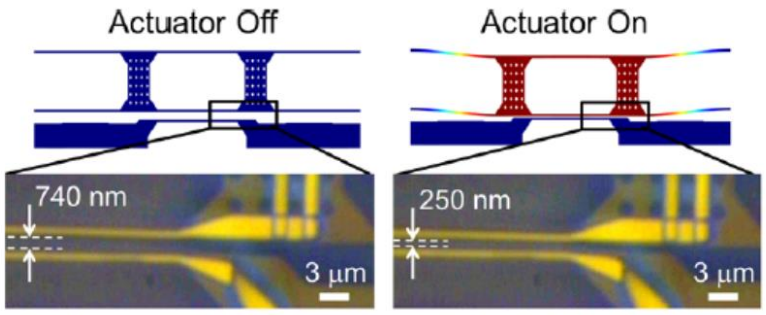

Figure 2.6: The schematic of the experiment setup built by St-Gelais et al. Two parallel nanobeams are integrated to a nanostructure. One nanobeam is fixed; the other nanobeam can be moved so that the distance between the two nanobeams can be adjusted. [25].

As a summary of this section, I have introduced experiment setups based on the parallel plate structure for which the sample size is at macroscopic scale. Another experiment setup integrated with on-chip nanostructure, which demonstrates the application of near field radiation at another scale. Together with the experiment setup that we developed in our own lab, hopefully I have given a quick review of the near field radiation measurement setups.

2.1.4 Experimental progresses on tuning the near field radiation

As introduced in the previous section, researchers have spent lots of time and resources to develop different experiment setups to demonstrate the concept of the near field radiation. Those efforts have expedited the maturing the experiment technique. At this stage, there is a trend that researchers are switching their focus to realizing the tuning of this near field radiation intensity. Lots of theoretical schemes

have been proposed, and some initial demonstrations have been published. Since the focus of this thesis on tuning near field radiation, it is really necessary to introduce the progress in this research topic.

P.J. van Zwol et al. first experimentally demonstrated the tuning of the near field radiation by use of the phase transition of VO_2[26][27]. By increasing the temperature, VO_2 will experience the phase change from insulator to metal. Its phase transition temperature is around 68°C. Most importantly, such phase transition will entail the changing of the surface polaritons status, which will directly affect the photon local density of states near the surface. As shown in Figure 2.7, their measurement shows that the insulator phase provides a higher near field radiation signal compared with the metal phase, which complies well with the theoretical predictions. In the insulator phase, the surface can support surface phonon polaritons which locates in the infrared range, so that the energy coupling between the microsphere and the sample can be stronger than that of the metal phase.

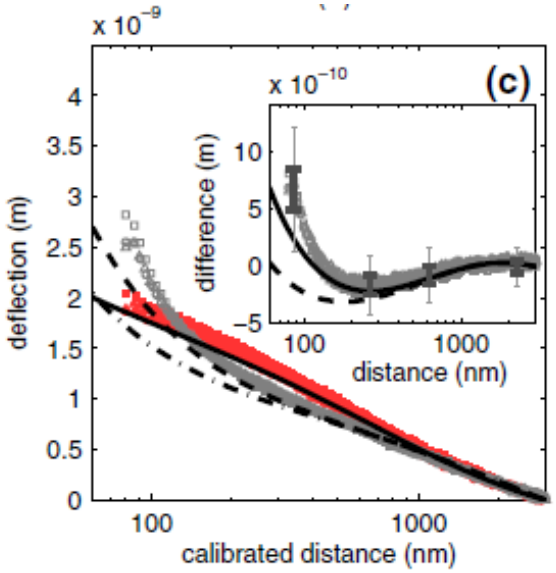

Figure 2.7: The open symbols represent the measurement signal from the insulating phase, while the closed symbols represent the metallic phase[27].

Except the above introduced experiment which is based on VO_2's the metal-insulator transition, P.J. van Zwol et al. also carry out another experiment to realize the tuning the near field radiation, which makes use of the thermally excited plasma in graphene [28]–[31]. Figure 2.8 shows the measurement results for a bare SiC substrate and two SiC substrates covered with 2 layers of graphene and 6 layers of graphene respectively. It shows that the near field radiation can be greatly enhances by simply adding layers of graphene on top of a substrate. As far as I know, this is the first application of graphene in near field radiation.

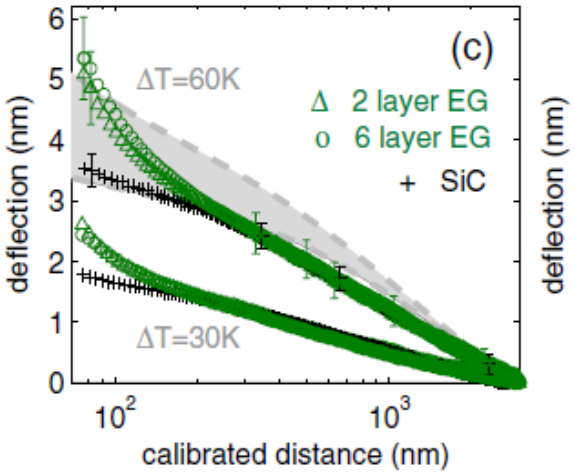

Figure 2.8: The black symbols represent the measurement signal from bare SiC substrate. The green triangular and the circular symbols represent the measurement signal of the SiC substrate covered with 2 layers of epitaxial graphene and 5 layers of epitaxial graphene[28].

Since researchers have just started switching the investigation on tuning the near field radiation, there is still not many published works available up to this point. For the preceding two cases that I introduced, they all use the mechanism of adjusting the surface polaritons. Inspired by these works, I carried out the experiment on tuning the near field radiation by use of doped silicon, which will be introduced in chapter 3. Actually, there is another mechanism that is proposed to achieve the tuning of the near field radiation, which is to tailor the electromagnetic properties of the material to accommodate radiations with extremely large wave vectors. I have also carried out experiment to verify this mechanism by use of hyperbolic metamaterials, which will be introduced in chapter 4.

2.2 Experimental setup developed in our lab

In this section, I will introduce in detail how do I carry out the near field radiation measurement using the system developed in our own lab, including the measurement details, system calibration, data process and uncertainty analysis.

2.2.1 Introduction to the optical deflection system

The experiment setup we developed to measure the near field radiation is actually inspired by the AFM technology. Compared with traditional AFM, one major improvement we make is to attach a microsphere onto the tip of the AFM cantilever, as shown in Figure 2.9 (a) and (b). The microsphere is made from fused SiO2 with a diameter of ~100 μm. The reason why we do it this way is because it is very

challenging to maintain two parallel plates at nanoscale gaps, while it is relatively easier to maintain the distance between a microsphere and plate at extremely small gaps. So, basically what we measured is nanoscale radiation between a microsphere and a sample plate. The cantilever applied here is the PNP-DB (NANO WORLD), which has a rectangular/diving board shape with a width of 40 μm and a length of 200 μm. It consists of a silicon nitride layer with 430 nm thickness and a gold layer with 70 nm thickness. Since the thermal expansion coefficients of those two materials are different, when the heat power transferring through the cantilever changes, the cantilever will bend correspondingly. And the resolution of the cantilever is measured to be as small as 0.1 nW[32][33].

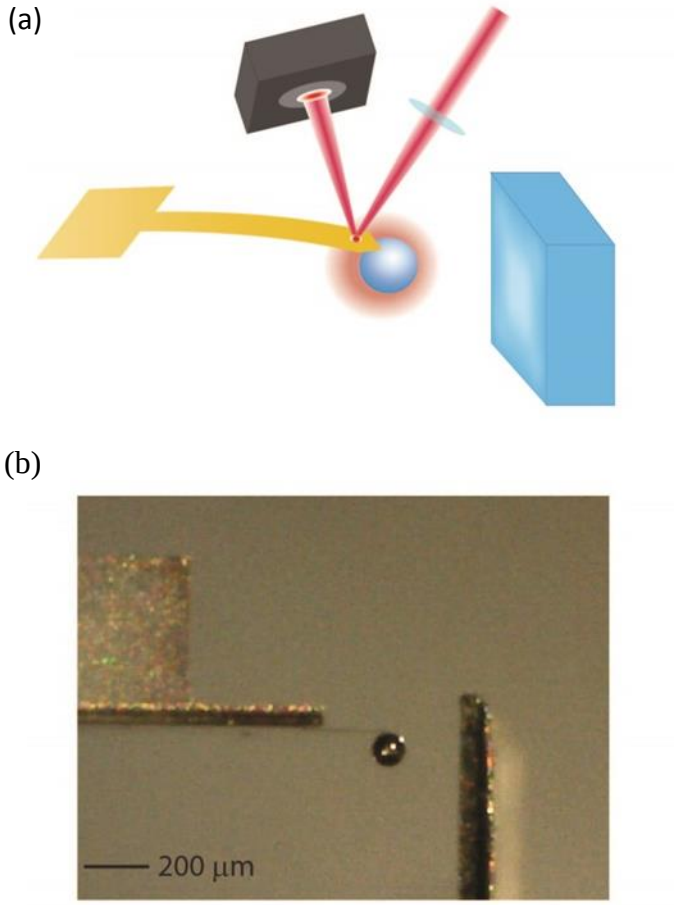

Figure 2.9: Experimental setup for near-field thermal measurements. (a) Schematic of the experiment setup that shows the relative position between the optical deflection system and the sample. (b) Optical image of the setup, which is apparently are sphere-plate geometry.

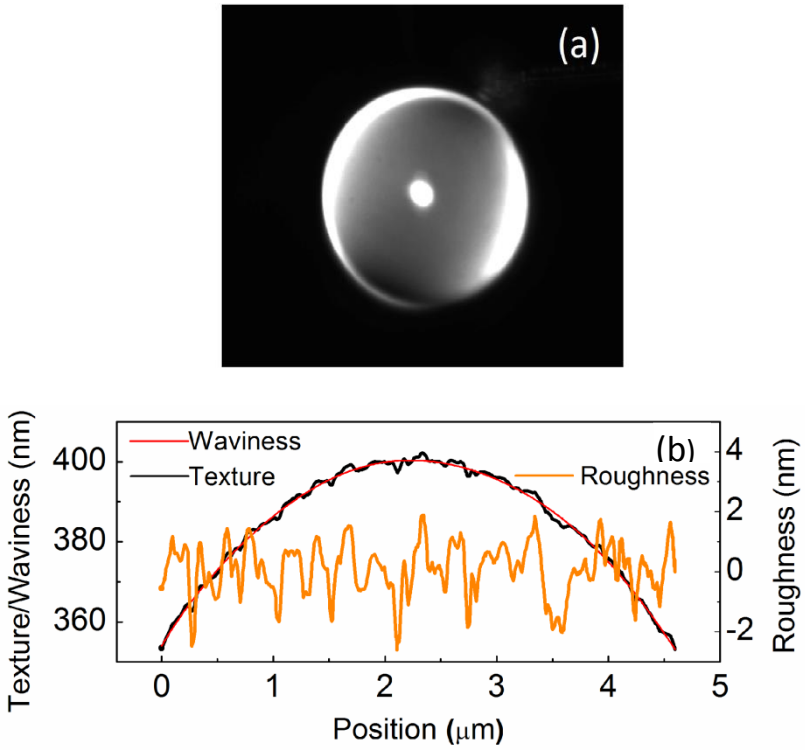

Figure 2.10: (a) The optical image of the microsphere. (b) The 1D roughness (the orange curve) is obtained by subtracting the 1D waviness (the red curve) from the 1D texture (the black curve) of the microsphere surface.

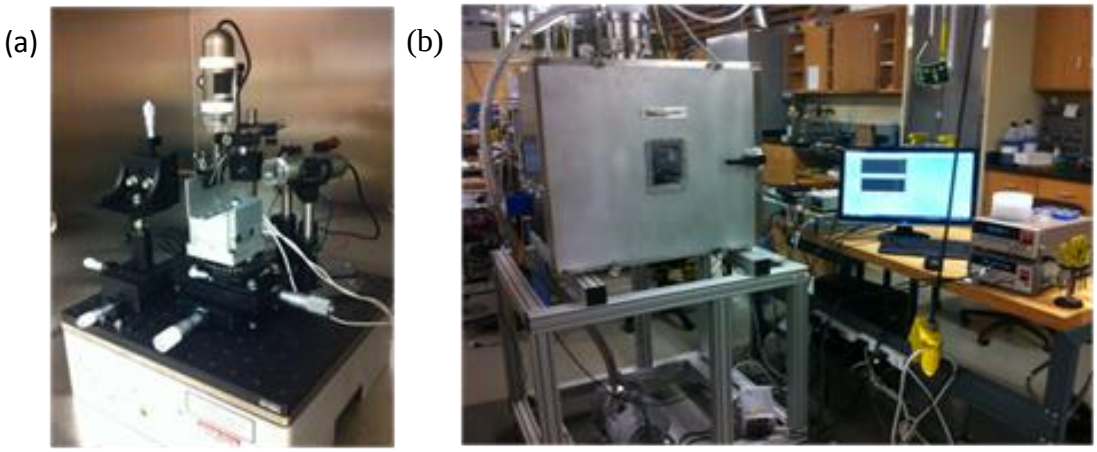

Figure 2.11: (a) The optical deflection measuring system is put on a vibration isolator, and all of them are put in the vacuum chamber shown in (b). (b) A panorama of our experiment system, the steel box on the left is the vacuum chamber.

An optical deflection system is constructed to monitor the bending of the cantilever. As shown by the schematic in Figure 2.9 (a), a laser is shined onto the tip of the cantilever. Then, it is reflected from the cantilever and shine onto a position sensing detector (On-Trak). This way the bending of the cantilever can be accurately detected by recording the position of the laser spot from the reflected laser beam. The tip of the cantilever, together with the microsphere, is heated up to ~50 °C by the laser, while the sample substrate is still maintained at ambient temperature. When the sphere approaches the substrate, the heat flow radiated from the microsphere to the substrate greatly increases due to the near-field radiative heat transfer between the microsphere and the sample substrate. The resulting temperature change of the sphere causes the bending of the cantilever, which is monitored by the optical deflection system which I introduced before. In our experiment, the gap between the sphere and the substrate is continuously reduced at a speed of 20 nm/s in order to minimize the influence of thermal drift of the AFM cantilever. As shown in the inset of Figure 2.12, the deflection signal of the cantilever, which also represents the near-field heat transfer signal, increases as the gap decreases with time. In Figure 2.12, the sharp change in the slope of cantilever deflection signals indicates the mechanical contact between the sphere and the substrate, thereby providing a reference to precisely determine the substrate-sphere separation. By further zooming in the collision range, a clear jump in

the deflection signal can be observed (as shown in Figure 2.13). It should be noticed that, in order to clearly define the nanoscale gap between the microsphere and the substrate, the surface roughness of both the microsphere and sample substrate is required to be as small as possible. The one dimensional (1D) roughness of the microsphere surface is measured to be ~4 nm (As shown in Figure 2.12 (b)). And, you will see in following chapters, confining the surface roughness of the sample substrate in an acceptable range is always one thing that we pay special attention.

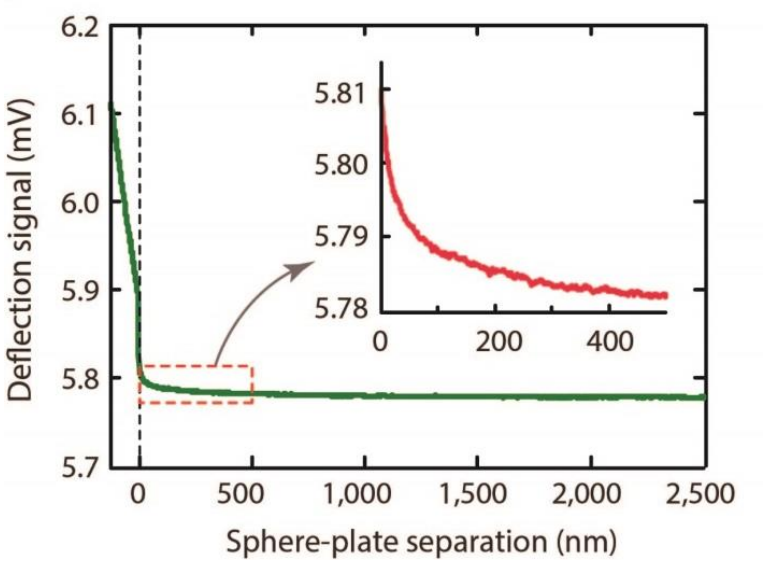

Figure 2.12: Typical cantilever deflection signals when the sphere approaches the substrate. The contact point between the sphere and the plate is marked by the vertical dashed black line. Inset: Deflection signals close to the contact point.

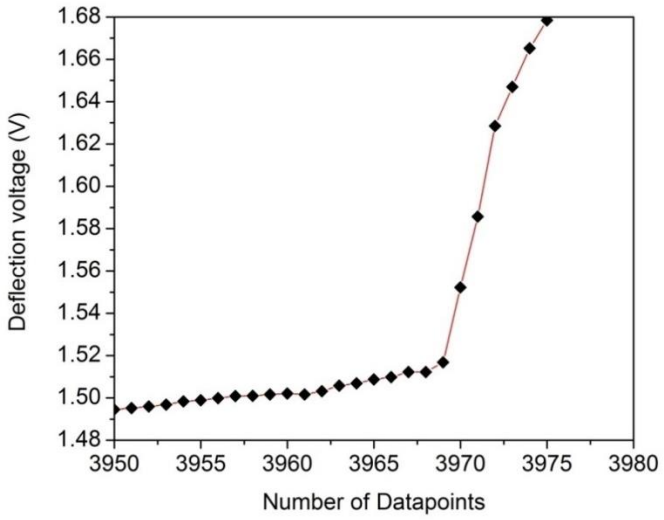

Figure 2.13: The deflection signal jumps up when the sphere collide with the sample plate.

Since the laser plays a pivotal role in the optical deflection system, it is really necessary to introduce in detail how we set up the optical system in our experiment. Since the laser not only serves as the light source in the optical deflection system but also serves as the heat source by heating up the microsphere, it is critical to maintain its incident power onto the cantilever as stable as possible. As shown in Figure 2.14, in our experiment, we managed to control the reflected laser power from the cantilever within the range of 1 mV. The more stable the laser power, the less vibration noise in the cantilever, and the more stable the temperature of the microsphere. The laser diode that we use is the Hitachi HL 6312G. The laser power will be fluctuate severely without introducing a feedback control loop. Here, we employed the laser controller from THORLABS (LDC 200 C). Under its constant power output mode, we are able to control fluctuation of the laser power in an acceptable range.

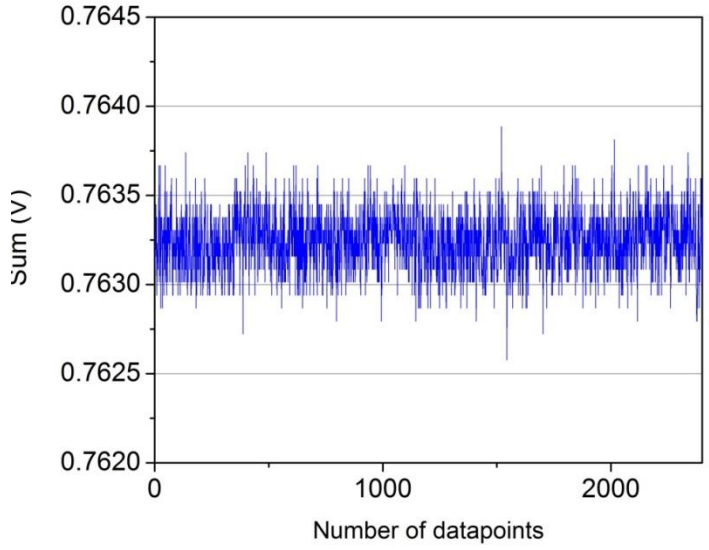

Figure 2.14 The Sum signal from the reflected laser beam. Its fluctuation is adjusted to be in the range of 1 mV.

All samples to be measured are attached along the edge of a copper plate in a vertical row. The copper plate is then loaded onto a 3D piezoelectric translation stage (MadCity Labs, Nano-3D200) with a step resolution of 1 nm. The piezoelectric translation stage is placed onto a motorized 3D micromanipulator with a traveling distance of 25 mm in all three axes (Sutter Instrument). The step resolution of the 3D micromanipulator is 1 μm. During our measurements, the samples can be switched conveniently by changing the height of the copper plate using the micromanipulator. By adding the 3D micromanipulator, it saves the trouble of pumping down the system and loading the sample every time when the sample needs to be changed, which greatly enhanced the measurement efficiency. The entire setup is placed on a mechanical vibration isolator. In order to eliminate the influence from the convection, the measurement is conducted under a vacuum level of 1×10^{6} Torr. The vacuum is

achieved by two stage pumping: the first stage/roughing pump is carried out by a scroll pump (Edwards XDS 5), the second stage/high vacuum pump is carried out by a turbo molecular pump (Pfeiffer TMH 260). Figure 2.11 shows the layout of the optical deflection system, as well as the vacuum chamber used to accommodate the whole system.

2.2.2 The beam theory

As introduced in the previous section, the cantilever used in this experiment is made of two layers of materials (gold and silicon nitride). Any temperature distribution away from the neutral temperature T_0 along the cantilever will result in the deflection of the cantilever due to the difference in thermal expansion coefficients of those two materials. According to the beam theory, the relation between the cantilever deflection and the temperature distribution is governed by the following equation:

$$\frac{d^2Z}{d^2x} = 6(\gamma_2 - \gamma_1)\frac{t_1 + t_2}{t_2^2 K}(T(x) - T_0) \qquad [30]$$

where x is the location along the cantilever, $Z(x)$ is the deflection of the cantilever at location x. γ is the thermal expansion coefficient, t is the thickness of one consisting layer of the cantilever, $T(x)$ is the temperature distribution along the cantilever, *K* is a constant determined by the thickness ratio of the two consisting layers and the Young's modulus of the two consisting materials, the equation for calculating *K* can be found in reference[33][34].

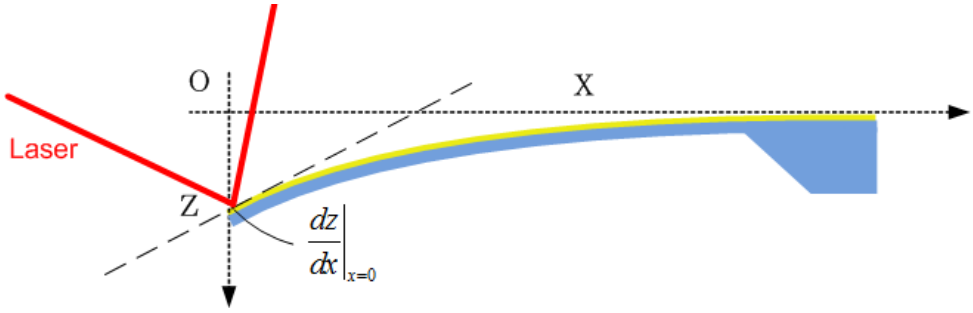

Figure 2.15: The schematic of the optical deflection system for monitoring the bending of the bi-material cantilever.

After knowing the governing equation (equation [30]), in order to solve $Z(x)$, we first need to know the temperature distribution $(T(x) - T_0)$ as well as the boundary conditions. As shown in Figure 2.15, we define the coordinate of the cantilever base as $x = l$. And the freely suspended end of the cantilever is defined as $x = 0$. Let's define G as the thermal conductance of the cantilever, P as the power transporting along the cantilever, and the temperature at the base $(x = l)$ is T_0. It should be noticed that: the power transporting along the cantilever is not always equal to the total absorbed laser power; it is only in the far field where P equals to the total absorbed laser power. Basically, the cantilever can be modeled as a thermal fin. By solving the 1D steady state heat conduction equation, we can get the temperature distribution along the beam:

$$T(x) - T_0 = \left(1 - \frac{x}{l}\right)\frac{P}{G} \qquad [31]$$

For the boundary condition, since the base of the cantilever is fixed at $x = l$, we can have $Z(l) = 0$, and $dz/dx = 0$ at the base. Combined with the calculated temperature

distribution, we can get the cantilever deflection distribution from equation (1)

$$\frac{dZ}{dx}\Big|_{x=0} = \frac{-3lPH}{G} \qquad [32]$$

where H is a constant determined by cantilever properties, the detailed equation for calculating H can be found in Reference[33][35]. It should be noticed that what the optical deflection system measure is actually the slope of the cantilever at the tip, which is the LHS of Equation [32]. The first step of the following data process is to get P. Before doing that, we need to know the values of l, H and G. l is the length of the cantilever which is 200 um, and H can be directly calculated from the cantilever properties. The method of calculating G will be introduced in the following section.

2.2.3 Thermal conductance of the bi-material cantilever

The measurement of thermal conductance of the cantilever (G) is suggested to be carried out before measuring samples. The process also serves as the system calibration. Before we start our discussion, let's first define several variables. φ will be used to denote the slope of the cantilever at certain location along the cantilever. S_T is used to denote the cantilever's sensitivity towards the base temperature. S_P is used to denote the cantilever's sensitivity toward the absorbed laser power. Here is the definition for S_T and S_P:

$$S_T = \frac{\partial \varphi_{tip}}{\partial T_b}, \qquad S_P = \frac{\partial \varphi_{tip}}{\partial P} \qquad [33]$$

According to the derivation given in reference[33], the thermal of conductance of the cantilever can be calculated from the ratio between the values of S_T and S_P

measured in the vacuum condition.

$$\left(\frac{S_T}{S_P}\right)_{vacuum} = 2G \quad [34]$$

In order to measure the cantilever's sensitivity towards base temperature, S_T, a mini heater is attached onto the base of the cantilever to heat the cantilever, so that the base temperature of the cantilever can be adjusted. A K-type thermal couple is attached to the area very close to the base of the cantilever to measure the base temperature. The cantilever's sensitivity to the absorbed laser power, S_P, can be measured by adjusting the laser power.

2.2.4 The near field radiative conductance between the microsphere and the sample

The near-field radiative conductance G_{NFR} can be calculated by:

$$G_{NFR} = \frac{\Delta P_{NFR}}{\Delta T} \quad [35]$$

Here, ΔP_{NFR} and ΔT need to be measured, respectively.

In our near-field measurements, the total heat flow absorbed from the laser P_{absorb} is conserved, so

$$P_{NFR} + P_{cantilever} = P_{absorb} = C_1 \quad [36]$$

$$\Delta P_{NFR} = -\Delta P_{cantilever} \quad [37]$$

In order to measure $\Delta P_{cantilever}$, we must first know the relation between $\Delta P_{cantilever}$ and Δx. Therefore, we carried out a calibration in the far field where $P_{NFR} = 0$, and

$$\Delta P_{cantilever} = \Delta P_{absorb} = \frac{\alpha}{1-\alpha}\Delta P_{reflect} \quad [38]$$

According to Reference [35], $\Delta P_{cantilever}$ is linear with Δx:

$$\Delta P_{cantilever} = R_{p-x}\Delta x \quad [39]$$

Combine Equation [38] and [39], we have

$$R_{p-x} = \frac{\Delta P_{cantilever}}{\Delta x} = \frac{\alpha}{1-\alpha}\frac{\Delta P_{reflect}}{\Delta x} \quad [40]$$

$\frac{\Delta P_{reflect}}{\Delta x}$ can be measured by changing ΔP_{sum}. After this calibration in the far field, R_{p-x} can be obtained, which enables the calculation of ΔP_{NFR}:

$$\Delta P_{NFR} = -\Delta P_{cantilever} = -R_{p-x}\Delta x \quad [41]$$

Thus far we have described how to calculate ΔP_{NFR} from Δx. For calculating ΔT, we approximate $P_{cantilever} \approx P_{absorb}$, considering $P_{NFR} << P_{cantilever}$. The derivation for ΔT is given below:

$$\left.\begin{aligned} G_{cantilever} &= \frac{P_{cantilever}}{\Delta T} \\ G_{cantilever} &= 0.5\frac{S_T}{S_P} \end{aligned}\right\} \Rightarrow \Delta T = \frac{2S_P}{S_T}P_{cantilever} \approx \frac{2S_P}{S_T}P_{absorb} = \frac{2\alpha}{1-\alpha}\frac{S_P}{S_T}P_{reflect} \quad [42]$$

Finally, through Equation [41] and [42], G_{NFR} can be calculated:

$$G_{NFR} = \frac{\Delta P_{NFR}}{\Delta T} = \frac{\alpha - 1}{2\alpha}\frac{S_T R_{p-x}\Delta x}{S_P P_{reflect}} \quad [43]$$

2.2.5 The uncertainty analysis for the measurement result

Based on Equation [43], the total uncertainty of G_{NFR} can be derived from the uncertainty propagation rule:

$$\left(\frac{e(G_{NFR})}{G_{NFR}}\right)^2=\left(\frac{e(S_T)}{S_T}\right)^2+\left(\frac{e(R_{p-x})}{R_{p-x}}\right)^2+\left(\frac{e(S_P)}{S_P}\right)^2+\left(\frac{e(P_{reflect})}{P_{reflect}}\right)^2 \quad [44]$$

In our measurements, the uncertainty of R_{p-x}, S_T, S_P and $P_{reflect}$ are:

$$\frac{e(R_{p-x})}{R_{p-x}}\approx 2\%,\ \frac{e(P_{reflect})}{P_{reflect}}\approx 0.04\%,\frac{e(S_P)}{S_P}\approx 2\%,\ \frac{e(S_T)}{S_T}\approx 3\% \quad [45]$$

Substitute [45] into [44], the total measurement uncertainty can be obtained:

$$\frac{e(G_{NFR})}{G_{NFR}}\approx 7\% \quad [46]$$

Now, let take a radiative conductance of 6 *nW/K* for example,

$$(G_{NFR})_{max}\approx 6nW/K \quad [47]$$

So the largest measurement uncertainty ranges for G_{NFR} is:

$$(e(G_{NFR}))_{max}\approx (G_{NFR})_{max}\,7\%\approx 0.42\ \ nW/K \quad [48]$$

From the above example, we can see that the measurement uncertainty is ~0.5 nW/K.

2.3 Summary

In the chapter, I tried to give a brief of the experiment techniques for near field radiation measurement. Different representative experiments are categorized based on its geometry: the parallel plate geometry and the sphere plate geometry. Special attention has been paid to the most recent development of the experiment technique. Based on that, combined with the topic of this thesis, I have also reviewed the experiment progress on tuning the near field radiation, which is an emerging research realm empowered by the maturing of different experiment technique.

After obtaining a panorama of different experiment techniques, I introduced in detail the experiment setup developed in our own lab which is based on an optical deflection system. Since the bi-material cantilever plays a pivotal role, the beam theory for describing the cantilever is introduced in the very beginning. After introducing the experiment setup, for data processing, the procedures of system calibration are introduced in detail, including the calculation of the thermal conductance of the cantilever and the radiative heat transfer coefficient between the microsphere and the plate. Moreover, the uncertainty analysis of the measurement results is also carried out.

3 Tuning near field radiation by doped silicon

3.1 Overview

As introduced in Chapter 1 and Chapter 2, radiative heat transfer between bodies can be significantly enhanced beyond Planck's law in the near-field due to photon tunneling mediated by electromagnetic surface waves. With the development of this realm, nowadays control of near-field radiative heat flux has become another hot research topic after the initial demonstrations. It has been theoretically predicted that NFRHT can be controlled using nanoporous materials[36], thin films[37][38], and graphene sheets, or by adjusting the material temperature[39], surface roughness[40], and metal-insulator transition. In contrast to a large number of theoretical studies, there exist few experiments that demonstrate the tuning of near field radiation. The initial experiment was recently carried out based on tuning the metal-insulator transition in phase change materials. One unique characteristic of doped semiconductors is that their plasma frequency can be tuned by modifying the carrier concentration. Theoretical calculations have shown that doping concentration can dramatically affect the near field radiation between two parallel semi-infinite doped silicon plates at different temperatures. Very recently, van Zwol et al. measured the near field radiation between a glass microsphere and two thin silicon films with different carrier concentrations, but detailed theoretical analysis was not provided[30], and the trend of near field radiation versus carrier concentration was still unclear as only two samples were measured. Up to the point of the proposal of this work, there is still no

comprehensive investigation of the near field radiation properties of doped silicon. Meanwhile, silicon is a fundamental and strategic material in semiconductor industry. As the feature size of silicon based MEMS devices, microchips, or other nanostructures keeps shrinking, nanoscale heat transfer analysis as well as nanoscale thermal management become more and more important. And, I believe that researches on investigating the near field radiation properties of doped silicon will have huge impact to the silicon industry in the near future. Such consideration gives me strong motivation to pursue this work.

One of the most interesting properties of doped silicon is that its properties, especially electrical properties, can be flexibly tuned in a very large range by adding dopant and changing the doping concentration. To quantitatively describe the impact of doping on the electrical properties of doped silicon, Drude model is usually applied to describe how the doping concentration affects the electrical dielectric function of doped silicon. Before applying the Drude model, the dopant (Boron, Phosphorus, and etc.) concentrations as well as the carrier (electron and hole) concentrations need to be known. Considering that not all the dopants are ionized, we need to first figure out how to get the relation between the dopant concentration and carrier concentration. The operation details will be introduced in a separate section for Drude model. As introduced in Chapter 1, there exists surface plasmon polariton in metal. Similarly, there could also exist surface plasmon polaritons in doped silicon as long as the carrier concentration is high enough. Since the dielectric function of silicon can be tuned by changing the carrier concentration, doped silicon provides the opportunity to overcome

this challenge due to the tunability of its surface plasma frequency.

In this chapter, I will provide a comprehensive analysis for tuning near field radiative heat transfer through changing the carrier concentration of both p-type and n-type bulk silicon[41]. Our theoretical calculations showed that the heat flow between doped silicon and silicon dioxide (SiO_2) which also supports surface excitations can be tuned by matching or deviating their resonant frequencies through changing the doping concentration of silicon. By use of the experiment setup introduced in the Chapter 2, we measured near-field radiation between a glass (SiO_2) microsphere and silicon plates with different doping concentrations at gap sizes ranging from 60 nm to 10 μm. Near field radiation measurements are carried out on multiple bulk silicon samples with different doping concentrations. The measured near field conductance agrees well with theoretical predictions, which demonstrates a tuning range from 2 nW/K to 6 nW/K at a gap of 60 nm.

3.2 Electronic properties of semiconductors

The reason why the near field radiation signal can be tuned by use of doped silicon is because its carrier concentration can be tuned through changing the dopant concentration. So, it's necessary to first recall some semiconductor fundamentals on how to calculate the carrier concentration from the dopant concentration. The method is actually pretty standard: the carrier concentration can be obtained by multiplying the density of states and the carrier distribution function. For Fermions, the carrier distribution obeys the Fermi-Dirac distribution. Here comes the major problem: to use

the Fermi-Dirac distribution, the Fermi energy (EF) needs to be first solved. In other words, for the same type of semiconductor with the same type of dopant, the Fermi energy is different for different dopant concentration. So, the problems becomes solving the Fermi energy corresponding to certain dopant concentration, which is the aim this section. To go through the whole process, let's start from some basic concepts such as density of states, carrier distribution function. Based on that, we can take one step further to calculate the Fermi level and the carrier concentration.

3.2.1 Density of states

The concept of density of states in semiconductors is used to describe the number of states per energy interval that could be occupied. Using the particle in a box model, we can get the density of states in the infinite potential well[42]:

$$g(E) = \frac{8\pi\sqrt{2}}{h^3} m^{*\frac{3}{2}} \sqrt{E} \qquad [49]$$

where g(E) represents the density of states at energy level E, h is the Planck constant, m* is the effective mass of the carrier (electron or hole). The reason for using the concept of effective mass is to take into consideration the periodic potential from the lattice. The formula can be applied to those free carriers in semiconductor as well. For electrons in the conduction band, the density of states can be calculated by

$$g_c(E) = \frac{8\pi\sqrt{2}}{h^3} m^{*\frac{3}{2}} \sqrt{E - E_c} \qquad [50]$$

where $g_c(E)$ represents the density of states for electrons in the conduction band. E_c

represents the energy at the bottom of the conduction band.

Similarly the density of holes in the valence band can be calculated using

$$g_v(E) = \frac{8\pi\sqrt{2}}{h^3} m^{*\frac{3}{2}} \sqrt{E_c - E} \quad [51]$$

where $g_v(E)$ represents the density of states for electrons in the conduction band. E_v represents the energy at the top of the conduction band.

3.2.2 Carrier distribution functions

After knowing the density of states for electrons and holes, to know the carrier density, we still need to know the occupation of those states. Electrons and holes are all known as Fermions, which obey the Pauli Exclusion Principle. The occupancy of energy states of Fermions are described by the Fermi-Dirac distribution function.

$$f(E) = \frac{1}{1 + e^{(E-E_F)/kT}} \quad [52]$$

where *f(E)* represents the probability of occupying the energy state E, E_F represents the Fermi energy, k is the Boltzmann constant, T represents the temperature. For the case of T=0K, when $E < E_F$, $f(E) = 1$; When $E > E_F$, $f(E) = 0$. So, the distribution function becomes a step function, which means all the energy states below E_F are fully occupied at the temperature of 0 K. This also gives the definition of Fermi energy.

3.2.3 Carrier density

After knowing the density of states and the Fermi distribution function, to calculate the occupied density of states, we only need to multiply the function for

density of states and the distribution function. Based on Equation [51] and [52], the electron density per unit volume and energy can be calculated by:

$$n(E) = g_c(E)f(E) \quad [53]$$

To calculate the density of holes, the situation is a little bit different. Since holes correspond to empty states unoccupied by electrons, its distribution function is $1 - f(E)$. So, we can use the following equation to calculate the hole density per unit volume and energy:

$$p(E) = g_v(E)(1 - f(E)) \quad [54]$$

By integrating equation [53] and [54], we can get the electron density and hole density, respectively.

$$n = \int_{E_c}^{\infty} n(E)dE = \int_{E_c}^{\infty} g_c(E)f(E)dE \quad [55]$$

$$p = \int_{E_c}^{\infty} p(E)dE = \int_{E_c}^{\infty} g_v(E)(1 - f(E))dE \quad [56]$$

Now, let assume the entire crystal is electrically neutral, which means the number of positive charge and the number of negative charge are equal. The positive charge is the sum of holes and ionized donors; the negative charge is the sum of electrons and ionized acceptors. Based on this assumption, we can get the following general equation:

$$n + N_A^- = p + N_D^+ \quad [57]$$

where N_A^- represents the concentration of the ionized acceptors, and N_D^+represents the concentration of the ionized donors. N_D^+ can be calculated by subtrating the unionized donor concentration from the total donor concentration.

$$N_D^+ = N_D - N_D\left(1 + \frac{1}{g_c}\exp(\frac{E_D - E_F}{kT})\right)^{-1} \quad [58]$$

where N_D is the total donor concentration, E_D is the donor energy level, and g_c represents the spin degeneracy of the donor. Similarly, N_A^- can also be calculated through similar Equation[43].

$$N_A^- = N_A - N_A\left(1 + \frac{1}{g_v}\exp(\frac{E_F - E_A}{kT})\right)^{-1} \quad [59]$$

where N_A is the total acceptor concentration, E_A is the donor energy level, and g_v represents the spin degeneracy of the acceptor.

By plugging Equation [55], [56], [58] and [59] into equation [9], we can get a transcendental equation. By solving this transcendental equation, we can solve the Fermi energy. Up to this point, I have introduced the steps of calculating the Fermi energy, so that we can get the relation between the dopant concentration and the carrier concentration.

3.3 Drude model for doped silicon

Fluctuation dissipation theorem (FDT) and Green's tensor are widely employed to calculate the radiative response from a body in the near field [3][44]. The FDT describes the statistical properties of random currents, while the Green's tensor enables us to calculate the electromagnetic response for a given geometry. In our calculation, all the materials are assumed to be isotropic and non-magnetic. The Drude model is used to describe the dielectric function of doped silicon[45]:

$$\varepsilon(\omega) = \varepsilon_{bl} - \frac{N_e e^2/\varepsilon_0 \, {m_e}^*}{\omega^2 + i\omega/\tau_e} - \frac{N_h e^2/\varepsilon_0 \, {m_h}^*}{\omega^2 + i\omega/\tau_h} \quad [60]$$

where the first term on the right hand side ε_{bl} represents the dielectric function of intrinsic silicon[46]. The second term is the Drude term for transitions in the conduction band (free electrons). The third term is the Drude term for transitions in the valence band (free holes). N_e and N_h are carrier concentrations for electrons and holes, ${m_e}^*$ and ${m_h}^*$ are effective masses of electrons and holes for conductivity calculation, and τ_e and τ_h are scattering times for free electrons and holes, respectively. Here, we take the values of effective mass as ${m_e}^* = 0.27m_0$ and ${m_h}^* = 0.37m_0$, where m_0 is free electron mass[45].

It can be seen from equation [60] that it is necessary to first determine carrier concentrations (N_e and N_h) and scattering times (τ_e and τ_h) in order to obtain a proper expression for $\varepsilon(\omega)$. When the doping concentration is low, complete ionization can be achieved. However, when the doping concentration is very high (>10^{19}/cm^3), the

dopants cannot be completely ionized. In this calculation, a general analysis is applied to account for both complete and incomplete ionizations based on charge neutrality[43]. This method is valid for both non-degenerately and degenerately doped silicon. Although scattering time is the most important parameter in the Drude model, it is difficult to calculate directly. The scattering time used here is extracted from the empirical expression for mobility[47].

In the present work, both carrier concentration and scattering time are determined by Hall effect measurements, which enables us to directly compare theoretical calculations with experimental measurements. The scattering time and the mobility are related by this equation:

$$\tau = \frac{m^* \mu}{e} \quad [61]$$

The mobility μ can be directly measured by Hall Effect measurement or directly calculated from empirical equations. In our calculation, we get the value of μ from following equation:

$$\mu = \mu_{min} + \frac{\mu_{max} - \mu_{min}}{1 + \left(\frac{N}{N_r}\right)^{\alpha}} \quad [62]$$

where μ_{max}, μ_{min}, N_r and α are all fitting parameters, N is the doping concentration. The value of those parameters can be found in Reference [42].

3.4 Theoretical analysis of the near field radiation from doped silicon

At thermal equilibrium, the fluctuation of electrons or ions in materials induces random currents, which radiate electromagnetic waves to the surroundings. For instance, the radiation from a medium to vacuum can be divided into three modes by comparing the values of β and k_0. Here, β denotes the component of wave vector parallel to the interface between the medium and vacuum, k0 denotes the wave vector in vacuum. When $\beta<k_0$, there are propagating waves on both sides of the interface, which are responsible for the far field thermal radiation from the medium. When $k_0<\beta<nk_0$, where n represents the refractive index of the medium, total internal reflection occurs, resulting in propagating waves inside the medium and evanescent waves outside the medium. When $\beta>nk_0$, there exist evanescent waves on both sides of the interface. In this case, resonant surface waves can be excited when $Re(\varepsilon)$ is negative and $Im(\varepsilon)$ is sufficiently small, where ε is the permittivity of the medium. Since the dielectric function of doped silicon cannot meet both conditions simultaneously, it is difficult to excite resonant surface plasmons in doped silicon[45]. But evanescent waves can still contribute to the near field radiation. Therefore, it is the second and third radiation modes that lead to the strong enhancement of radiative heat transfer of doped silicon in the near field.

Using the Green's tensor and FDT, the LDOS of photons in the vicinity of SiO_2 and doped silicon surfaces can be calculated[3][41]. Figures 3.1(a) and 3.1(b) show the

LDOS at a distance of 50 nm from the surfaces of arsenic-doped n-type silicon and boron-doped p-type silicon, respectively. The black curve with sharp peaks represents the LDOS at a distance of 50 nm from the surface of SiO_2. There also exists a peak in the LDOS spectrum for doped silicon. Moreover, the peak can be shifted through modifying its carrier concentration. As shown in Figure 3.1(a), when the carrier concentration is low, the peak is located at low frequencies. In this case, there is no overlap between the LDOS peaks of doped silicon and SiO_2, indicating a weak coupling between these two materials. As carrier concentration increases, the peak of doped silicon moves towards higher frequencies. The strongest enhancement of NFRHT between SiO_2 and doped silicon occurs when the peak of doped silicon overlaps with the strongest peak of SiO_2. The corresponding carrier concentration of n-type doped silicon is around $1.5\times10^{19}/cm^3$, as shown by the red curve in Figure 3.1(a). Figure 3.1(b) shows the evolution of the LDOS peak of p-type silicon versus carrier concentration. All the peaks of LDOS for p-type silicon shows a red shift for the same carrier concentrations, compared with n-type silicon. This is attributed to the difference of effective mass and scattering time between electrons and holes.

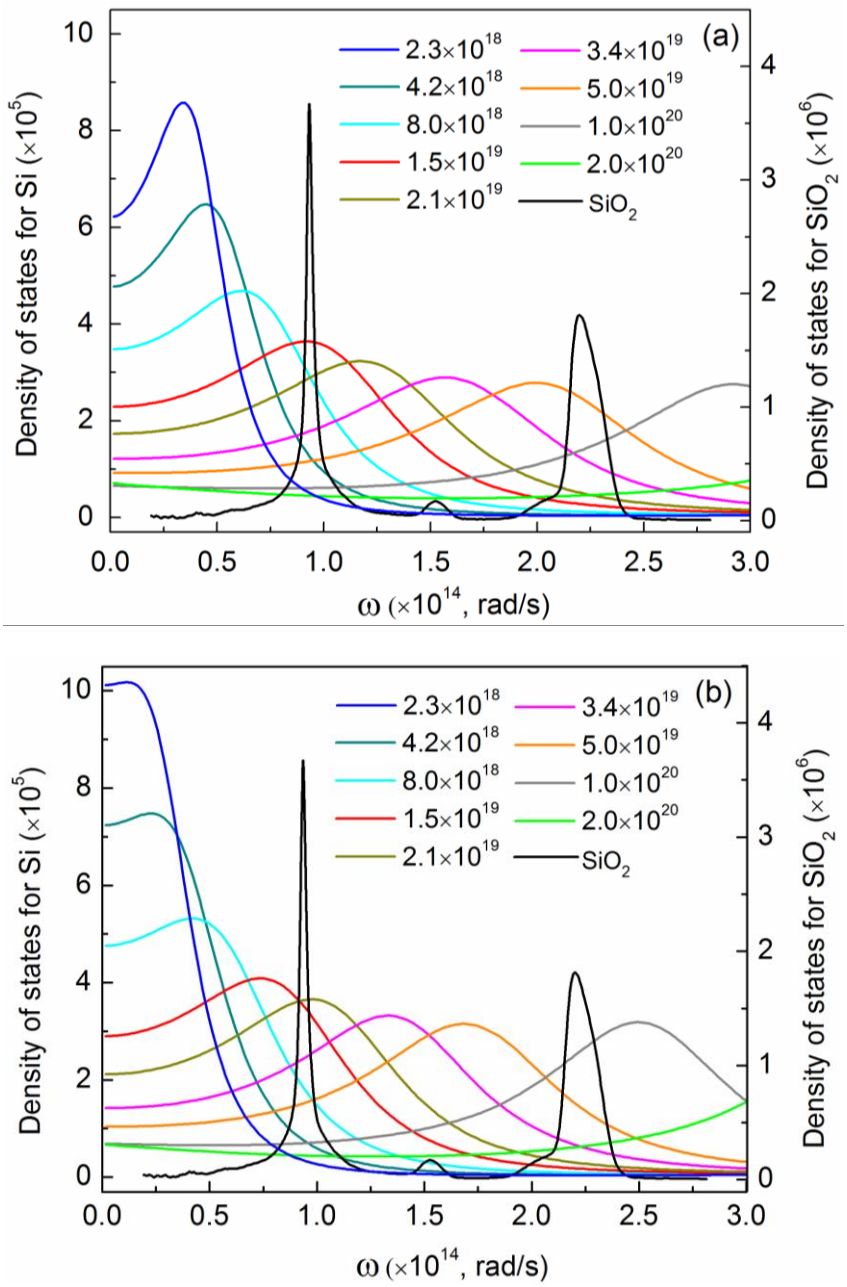

Figure 3.1: (a) Local density of states at a distance of 50 nm from the surfaces of SiO_2 (black curve) and arsenic-doped n-type silicon (all other curves) with different carrier concentrations (unit, /cm^3). (b) Local density of states at a distance of 50 nm from the surfaces of SiO_2 (black curve) and boron-doped p-type silicon (all other curves) with different carrier concentrations (unit, /cm^3).

3.5 Measurement results and discussion

Experimental details have been described in our previous publications[48]. Here, we only introduce several key points. To prepare the probe, a glass microsphere (Microspheres-Nanospheres) with a diameter of ~100 μm is attached onto the tip of a bi-material rectangle cantilever using silver epoxy)[32]. The surface roughness of the microsphere is required to be as small as possible in order to clearly define a nanoscale gap between the microsphere and the sample. The one dimensional (1D) roughness of the microsphere surface is measured to be ~4 nm (Figure 2.10). All bulk silicon samples are aligned along the edge of a copper plate and then loaded onto a 3D piezoelectric translation stage (MadCity Labs) with a step resolution of 1 nm. The piezoelectric translation stage is placed on a motorized 3D micromanipulator with a traveling distance of 25 mm in all three axes (Sutter Instrument). During our measurements, the samples can be switched conveniently by changing the height of the sample loader using the micromanipulator. The heat flow radiated by the microsphere greatly increases due to the enhancement of near field radiative heat transfer when the sphere approaches the sample. The resulting temperature change of the cantilever causes its bending. The deflection of the cantilever at the tip is monitored using an optical deflection system. The entire setup is placed on a mechanical vibration isolator, and the measurement is conducted under a vacuum level of ~1×10^{-6} Torr.

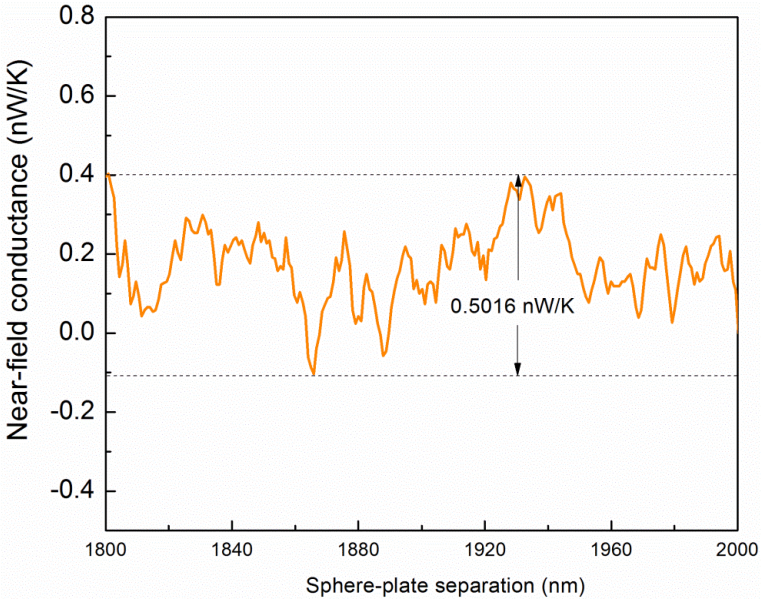

Figure 3.2: The signal oscillation during the measurement. This also complies with the result of uncertainty analysis in Chapter 2.

Table 3.1: Hall Effect measurements of five different samples

Sample	Carrier concentration	Mobility	Bulk resistivity	Type
1	$1.31\times10^{11}/cm^3$	1770 $cm^2/V\cdot s$	2.71×10^4 Ω·cm	intrinsic
2	$2.99\times10^{14}/cm^3$	1960 $cm^2/V\cdot s$	10.6499 Ω·cm	p, boron
3	$3.09\times10^{19}/cm^3$	59.7 $cm^2/V\cdot s$	0.0033 Ω·cm	p, boron
4	$1.27\times10^{19}/cm^3$	114.2 $cm^2/V\cdot s$	0.0043 Ω·cm	n, arsenic
5	$2.03\times10^{20}/cm^3$	45.4 $cm^2/V\cdot s$	0.0007 Ω·cm	p, boron

Five bulk silicon samples with different carrier concentrations are measured to demonstrate the tunability of near-field conductance. Considering the difference

between the electron and hole mobility, an n-type doped silicon sample is also included. The carrier concentrations and the mobility of all five samples are determined by Hall Effect measurements, as shown in Table 3.1. The surface charges on the microsphere and the sample are minimized by contacting them with a grounded copper plate before measurement so that the electrostatic force can be well suppressed. The near field conductance between the microsphere and the samples are calculated using the Derjaguin approximation[21]. In Figure 3.1(a), starting from the intrinsic silicon (black curve), the near field conductance of p-type doped silicon increases with the increase of carrier concentration from $3.0\times10^{14}/cm^3$ (green curve) to $3.0\times10^{19}/cm^3$ (red curve). However, if the carrier concentration is too high, e.g., $2.0\times10^{20}/cm^3$, the near field conductance drops dramatically (cyan curve). This is because the peak of LDOS for doped silicon significantly deviates from the surface phonon polariton resonance peaks of SiO_2 at such a high carrier concentration (Figure 3.1(b)).

It should be pointed out that electrostatic forces may have a dominant influence in the experiments. To minimize the surface charges on the microsphere and the doped silicon sample, a grounded copper plate is brought into contact with the microsphere and the silicon sample for a few times before carrying out the measurements. Then, we measure the influence of electrostatic force from residual charges by illuminating a very weak laser beam onto the tip of the cantilever so that the near-field radiation signal is minimized. As shown in Figure 3.3, the red curve and the black curve are the measurement results under different laser output powers (1 mW and 0.2 mW). The black curve keeps almost flat with respect to the gap size, while the red curve shows

obvious increase when the gap size decreases. The small increase at very small gaps in the black curve is mainly due to the near-field radiation caused by the laser output power of 0.2 mW, as well as the van der Waals force when the gap size is smaller than ~60 nm. The comparison between the black curve and the red curve in Figure 3.3 provides a solid proof for the suppression of the electrostatic force during our measurements.

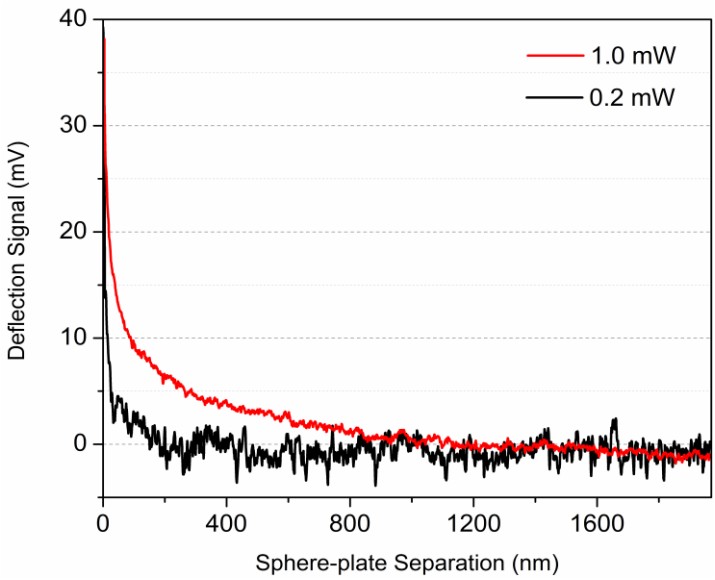

Figure 3.3: The raw deflection data from measuring the doped silicon sample with a carrier concentration of $3.09\times10^{19}/cm^3$, using different laser output power 1.0 mW and 0.2 mW.

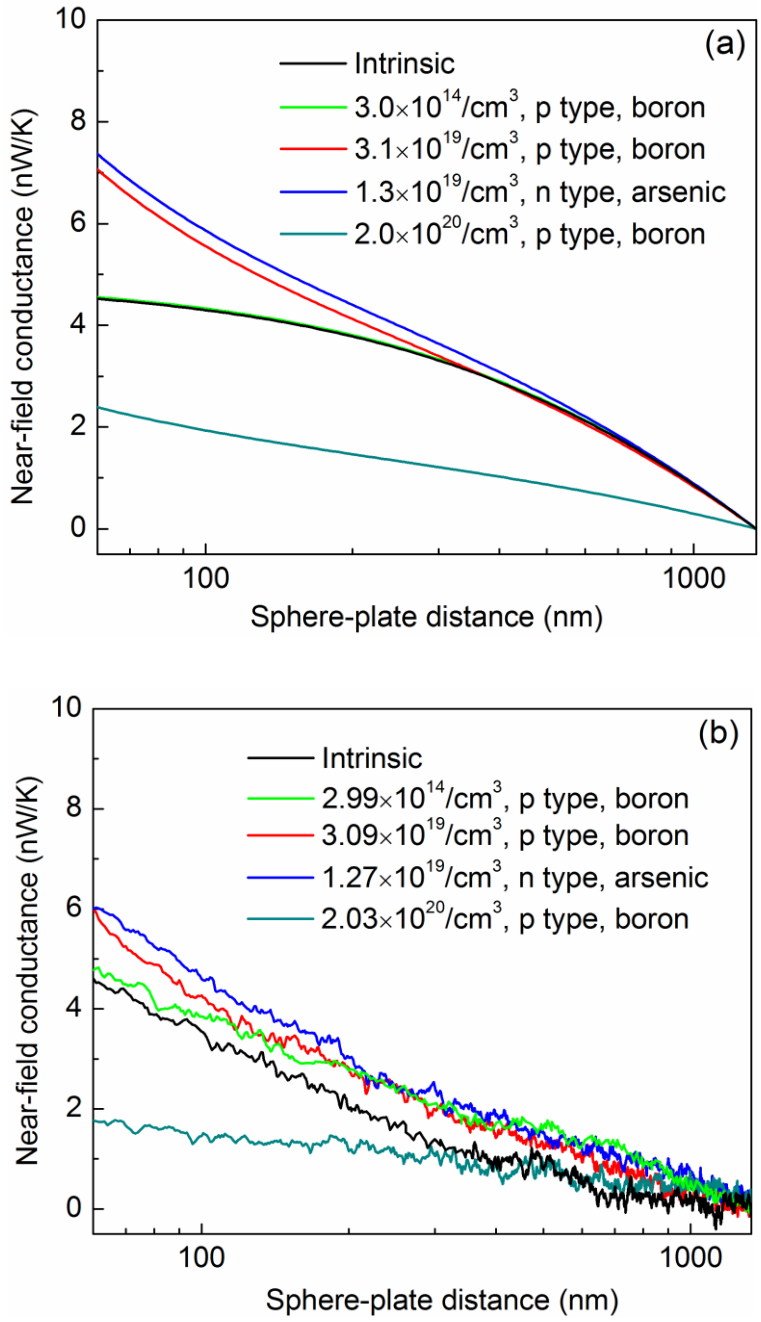

Figure 3.4: (a) Calculated near field conductance curves corresponding to the five bulk silicon samples at different carrier concentrations. (b) Measured near field conductance curves corresponding to the five bulk silicon samples. The measurement uncertainty is estimated to be ~0.5 nW/K in terms of the noise level of deflection

signals, the error in cantilever calibration, etc.

In our experiments, the directly measured signal is the deflection of the cantilever, which can be further calibrated to obtain the near field conductance[33][35] . Figure 3.4(b) shows the measured near field conductance for the five samples. The black curve is the measured near field conductance for the intrinsic silicon. For the p-type samples with carrier concentration of $2.99\times10^{14}/cm^3$ (green curve) and $3.09\times10^{19}/cm^3$ (red curve), the near field conductance is higher than that of the intrinsic silicon due to the contribution from free carriers. When the carrier concentration is as high as $2.03\times10^{20}/cm^3$ for p-type samples, a large decrease in the near field conductance is observed, as predicted in Figure 3.4(a). For the n-type sample with a carrier concentration of $1.27\times10^{19}/cm^3$ (blue curve), an enhancement of near field conductance beyond intrinsic silicon is also observed, which is consistent with the prediction in Figure 3.4(a). At a gap of ~ 60 nm, near-field conductance can be dramatically tuned from 2 nW/K to 6 nW/K by changing the doping concentration of silicon.

3.6 Summary

In this chapter, I introduced the project on tuning near radiation signal by use of doped silicon. For the discussion about this typical semiconductor, I start this chapter by recalling the semiconductor fundamentals. The purpose of introducing those fundamentals is to find the relation between doping concentration and the carrier concentration in doped silicon, which is needed in establishing the Drude model.

Considering the importance of the dielectric function during the whole calculation, special attention has been paid on introducing the Drude model for doped silicon at different carrier concentrations. After obtaining the electric properties of doped silicon, further theoretical calculation shows that the near field radiative heat transfer between doped silicon and silicon dioxide can be significantly tuned by changing the carrier concentration of silicon. Our experimental results for both n-type and p-type silicon samples agree well with theoretical predictions. The tunable near field thermal conductance may shed light on the development of thermophotovoltaic devices and advanced thermal management systems.

4 Near-field energy extraction with hyperbolic metamaterials

4.1 Overview

Control of thermal emission is important in a broad range of applications: e.g., thermal management[39], energy conversion[49], thermal barriers[50], and thermal signature control[51]. Blackbody radiation described by the well-known Planck's law[52] dictates the maximum of thermal radiation in the far-field. To enhance the far-field thermal radiation from a blackbody emitter, a "thermal extraction" scheme has recently been developed by optically contacting the emitter with a passive extraction device[53]. Although the extraction device itself is transparent for thermal radiation, its internal density of states is higher than vacuum and therefore enables more emission channels by extracting evanescent electromagnetic waves with lateral wave vector K in the range of $k_0<K<n_ek_0$, where k_0 is the wave vector in vacuum, and ne is the refractive index of the extraction device. The performance of such far-field extraction devices is limited by ne^2 times of the blackbody radiation limit. In contrast, near-field thermal extraction, where the characteristic length scale is smaller than the wavelength of thermal radiation[54], can potentially overcome this limitation by extracting a full range of evanescent waves.

In this chapter, I'll introduce our work on realizing the near field energy extraction by use of hyperbolic metamaterials (HMs)[55]. First, I will introduce briefly the

concept of HMs. Then, I'll introduce the theoretical calculation and simulation result of the near field radiation properties of HMs. After laying the basic theoretical foundation, I will switch to the experiment side to introduce in detail the fabrication procedures of nanowire array based HMs, including electrodeposition, chemical mechanical planarization (CMP), wet etching, etc. In the end, the near field radiation measurement results of those nanowire array based HMs will be introduced and discussed. It is shown that such HMs can significantly enhance near-field energy transfer by extracting evanescent waves with arbitrarily large lateral wave vectors. The realization of near-field thermal extraction has important practical implications in areas, such as thermophotovoltaic energy conversion[29], radiative cooling[56], thermal infrared imaging[57], and heat assisted magnetic recording[58].

4.2 Introduction to hyperbolic metamaterial and its near field radiation properties

4.2.1 Introduction to hyperbolic metamaterials

As a special class of indefinite media, HMs with the principal components of the permittivity tensor ϵ having opposite signs have attracted significant interest because of their unique properties, such as negative refraction and sub-wavelength imaging[59]–[62]. The dispersion relation of HMs generally satisfies a hyperbolic function (red curves in Figure 1(a))[63]:

$$\frac{k_z^2}{\epsilon_{x,y}} - \frac{K^2}{|\epsilon_z|} = k_0^2, \qquad [63]$$

where ϵ_z is the vertical component ($\epsilon_z < 0$), $\epsilon_{x,y}$ is the lateral component ($\epsilon_{x,y} > 0$) with the materials assumed to be uniaxial (i.e., $\epsilon_x = \epsilon_y = \epsilon_{x,y}$), k_z and K are the vertical and lateral components of the wave vector, respectively. If a point source is located near a HM, its emitted evanescent waves in vacuum (wave vector $k = \sqrt{k_z^2 + K^2} > k_0$) can excite propagating modes in the HM, leading to enhanced photon local density of states (PLDOS). To illustrate near-field thermal extraction, we consider radiative heat transfer between an emitter and an absorber, where a lossless HM (i.e., a real permittivity tensor ϵ) is placed between the emitter and the absorber, and is in contact with the emitter as a thermal extraction device. If the gap between the emitter and the absorber is large compared with the wavelength of thermal radiation, evanescent waves from the emitter cannot directly contribute to heat transfer because of their exponential attenuation across the gap. However, according to Equation (1), these evanescent waves can be converted into propagating waves in the HM and thus transfer energy from the emitter to the absorber. In comparison with the extraction device for far-field emission[53], an ideal HM extractor could introduce an unlimited number of energy transfer channels between the emitter and the absorber.

4.2.2 The near field radiation properties of hyperbolic metamaterials

A number of structures, such as alternating metal-dielectric layers and metal wire arrays (MWAs), have been proposed to realize HMs. In the infrared regime, metals behave like perfect electric conductors that barely emit or absorb light. Metamaterials made from MWAs are extremely low-loss and can maintain the hyperbolic dispersion in a broad frequency band[64][65]. Particularly, MWAs were demonstrated to be

broadband infrared and terahertz waveguides with a dispersion relation, $k_z = \sqrt{\epsilon_{x,y}} k_0$, which corresponds to a HM with $\epsilon_z = \infty$, reducing the hyperbolic function to two flat lines (blue dashed lines in Figure 1(a))[66]. As a result, MWAs perform as lossless waveguides that can duplicate the exact field profiles at one end and transfer them to the other end. To quantitatively evaluate the performance of MWAs as a near-field thermal extractor, we calculate the PLDOS near a slab made from MWAs. For a system at thermal equilibrium, the general formulation of PLDOS, $\rho(r,\omega)$, is expressed by[55][64]

$$\begin{aligned}\rho(r,\omega) &= \langle U(r,\omega)\rangle \Big/ \left(\frac{\hbar\omega}{\exp(\hbar\omega/k_B T)-1}\right) \\ &= \frac{\omega}{\pi c^2}\,\mathrm{Im}\,Tr\left[\overleftrightarrow{G^E}(r,r,\omega)+\overleftrightarrow{G^H}(r,r,\omega)\right]\end{aligned} \qquad [64]$$

where $\langle U \rangle$ is the local energy density of thermal radiation, G^E and G^H are the electric and magnetic dyadic Green functions of an inhomogeneous system, respectively[20]. Here, $\rho(r,\omega)$ can be understood as the average number of thermally emitted photons at location r, which includes contributions from both propagating and evanescent waves.

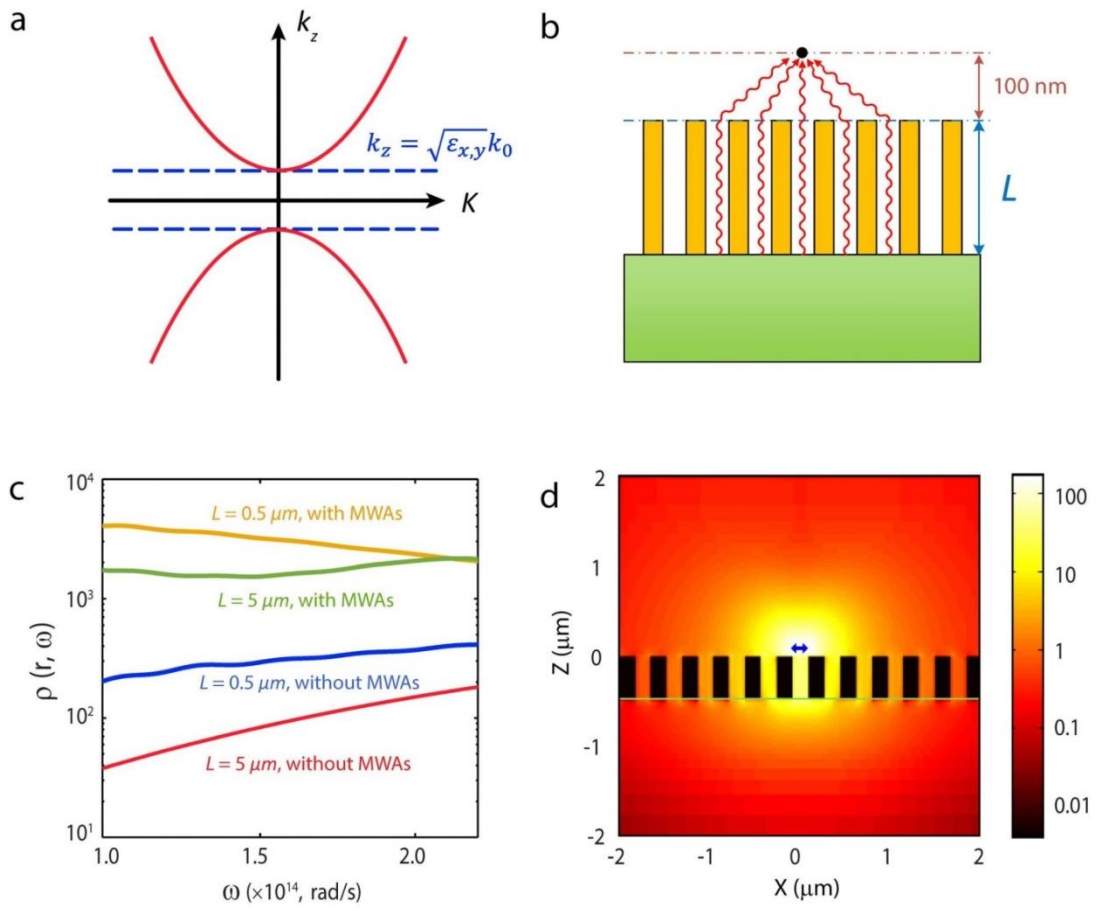

Figure 4.1: HMs mediated near-field thermal extraction. (a) Dispersion relation of typical HMs (red curves) and MWAs (blue dashed lines). (b) Schematic of the MWA-based near-field thermal extractor. (c) Calculated PLDOS at 100 nm above MWAs for different lengths L=500 nm and L=5 μm with/without the MWAs. (d) Electric field intensity excited by a dipole located at 100 nm above the 500 nm thick slab of MWAs.

As one example, a HM slab composed of MWAs is in close contact with an emitter having a refractive index $n = 1.5 + 1.5i$ (Figure 4.1(b)). The period and the radius of MWAs are set to be 350 nm and 100 nm, respectively, which ensures a hyperbolic dispersion of the MWAs in the infrared range. In Figure 4.1 (c), the

calculated PLDOS at a distance of 100 nm above the HM slab can be enhanced by one order of magnitude, compared with the PLDOS at the same location without the HM slab. Moreover, the 5 μm thick slab has similar PLDOS enhancement with the 500 nm thick slab. This is because the waveguiding properties or the HM characteristics of MWAs are almost independent of the wire length, as long as the period of the wires is much smaller than the lateral wavelength of incident photons. The HM modes in MWAs are extremely low-loss because electromagnetic energy is highly concentrated on metal wire surfaces with little penetration. The decay length of MWAs, for example, nickel wire arrays, is estimated to be ~100 μm at the wavelength of 10 μm. Figure 4.1 (d) shows the electric field profile excited by a dipole located at a 100 nm distance above the 500 nm thick slab. The uniform field distribution along the wires further confirms the wave guiding effect of MWAs.

In chapter 1, I introduced the method of calculating photon local density of states (PLDOS) using the dyadic Green's function. As I mentioned, the Green's function for some simple structures, for instance, a semi-infinite plane, parallel plane and etc., has been solved and can be easily found from relevant literatures. However, for even a little bit more complicated structures, the Green's function is not readily available and it is very difficult or even impossible to get the analytical solution of their Green's function. In order to get the Green's function of those nanowire arrays, we must use numerical method. The following paragraph introduces in detail how we calculate the Green's function and the Photon Local Density of States (PLDOS) of the geometry of nanowire arrays.

The PLDOS in Equation [64] is numerically calculated by the finite-difference time-domain (FDTD) method using commercial software (Lumerical Solutions). To evaluate the PLDOS, an electric (and magnetic) dipole polarized in different directions is placed at the distance of 100 nm above HM slabs in vacuum. Then, the FDTD simulation records the electric (and magnetic) field at the location of the dipole. As a result, the dyadic Green's function tensor can be obtained as[55]

$$G_{jj}^{E} = \frac{E_j}{\omega^2 \mu_0 p_j}$$
$$G_{jj}^{H} = \frac{H_j}{i\omega m_j} \qquad [65]$$

where $j = \{x, y, z\}$ denotes the polarization direction. p and m indicate the electric and magnetic dipole moment, respectively.

4.3 Fabrication of nanowire array based hyperbolic metamaterials

4.3.1 Electrodeposition of nanowire arrays

The AAO templates used in this experiment are the Whatman® anodisc inorganic membranes with a diameter of 21 mm. It consists of two layers: one is the active layer with the nominal pore diameter (~100 nm), the other is the supportive layer with a pore diameter of ~180 nm. The thickness of the active layer is 2 μm, while the thickness of the supportive layer is 58 μm. Before electroplating, a thin layer of nickel with a thickness of ~100 nm was sputtered onto the side of the active layer to serve as a seed layer for electrochemical deposition. The electrolyte solution used in this experiment is

the Nickel Sulfamate RTU purchased from Technic Inc.[67] In our electroplating setup[68], the sputtered template is the target, which is attached to a copper conductive tape and vertically soaked into the electrolyte solution. This serves as the cathode. To the opposite of the cathode, it hangs the anode, which is a square shaped platinum plate. A magnetic stirrer was used to keep the solution continuously agitated at a speed of 100 rpm[69]. It should be noticed that agitation is very important in increasing the copper deposition speed as well as increasing the surface uniformity. Under a constant current of 0.1A, it takes ~180 minutes to grow nickel out of the nanopores and cover the whole area of the template. The whole electroplating process was carried out at room temperature (~21 ˚C)[70]–[72].

Figure 4.2: (a) Optical image of an AAO template with a polymer support ring. (b) Optical image of the AAO template with nickel seed layer sputtered on one side. (c) Optical image of the AAO template after nickel electroplating.

4.3.2 Chemical mechanical planarization of metal nanowires/alumina composite surface

Chemical Mechanical Planarization (CMP) was initially developed at IBM for the purpose of polishing those interlayer dielectrics in the multilayer metal structure. Gradually, it has developed into today's stage, which empowers two indispensable processes during micro chip fabrication: the copper Damascene process and the shallow trench isolation (STI) process. Before the invention of CMP, aluminum was dominant metal used for interconnecting purposes although copper has a lower resistivity than aluminum. The reason for that is copper cannot be easily removed by use of reactive ion etching (RIE)[73]–[76]. The CMP technique enables the damascene process, which makes it possible to first fill the inlaid trenches with copper and later to remove the unwanted copper through CMP. After the copper Damascene process, an extremely smooth starting plate is obtained for later processes. For the STI, its invention is motivated by increasing the package density of transistor. The previous LOCal Oxidation of Silicon (LOCOS) suffers from the so called 'bird's beak' effect, which makes it incapable of continuing fueling the Moore's law. STI replace LOCOS by totally reinventing the process, which make is possible to fabricate vertical isolation between transistors so that the packaging density of transistors is greatly enhanced. The step we are using is very similar to the copper Damascene process: CMP is used to polish a surface that consists of copper nanowires/ alumina composite materials[74][77][78].

The CMP machine that we are using is the semi-automatic Strasbaugh 6EC, which is programmable through a touchscreen GUI. There are many variables in the CMP process that can affect the polishing quality including the sample protrusion height from the retaining ring, back pressure, down force, polishing pad type, slurry type[79] and flow rate, etc.[80] These parameters need to be adjusted specifically according to the sample. In our experiment, the sample is adjusted to protrude 10-20 μm from the retaining ring, ensuring that a large portion of the downward pressure is exerted on the sample. The downward pressure and the back pressure are set to be 5 psi and 4 psi, respectively. The table and chuck rotation speed is 50 rpm. The polishing pad used here is the IC1000™ made of porous polyurethane. It has typical applications in ILD CMP, STI, metal Damascene process. Due to its high hardness and stiffness, it could provide decent planarity and largely suppress the edge effect. Before each CMP run, the pad is conditioned to maintain the necessary roughness and to provide a consistent starting surface quality. Moreover, In situ conditioning was carried out throughout the polishing process so that the surface structure of the pad was maintained in good situation. Since the machine and pad have been chosen, the type of slurry has a huge impact on the final polishing results. The slurry should be carefully chosen for polishing different materials and for different processes. In our experiment we use two different types of slurries: the Fujimi Metal Polish No. 2 and the Eminess Ultra-Sol A20. Those two types of slurry result in extremely different polishing quality, which is introduced in detail in the following sections.

Table 4.1: Parameters setup for the CMP process

Back Pressure	10 psi
Down Force	4 psi
Pad Rotation Velocity	50 rpm
Table Rotation Velocity	50 rpm
Slurry Flowrate	150 mL/min
Wafer Protrusion from the Ring	10-20 μm

In the following paragraphs of this section, I'll introduce separately the CMP results using different slurries: (1) Fujimi Metal Polish No. 2. (2) Eminess Ultra-Sol A20.

The Fujimi Metal Polish No. 2 slurry was purchased in the form of powders, which consists of α-alumina crystal particles with an average diameter of 2 μm. The slurry is made directly from mixing the alumina powders and DI water with a weight ratio of 1:10. The polishing process is mainly based on the physical abrasion from the alumina particles since there are no acids or oxidizers added into the slurry. Figure 1 shows the pictures of one typical sample at different stages of CMP. Once the copper layer above the nanowires array is polished away, the nanowires array will expose, and the color of the sample will change from brown (color of copper bulk) to dark red (color of copper nanowires). After polishing, the roughness of the dark red ring-shape area and the copper covered center area of the sample (as shown in Figure 4.3(d)) is characterized by AFM, respectively. The roughness of the areas where the copper nanowires get exposed is measured to be within 50 nm (as shown in Figure 4.3 and

Figure 4.4), while the roughness of the copper covered center area is measured to be within 200 nm (as shown in Figure 4.5 and Figure 4.6).

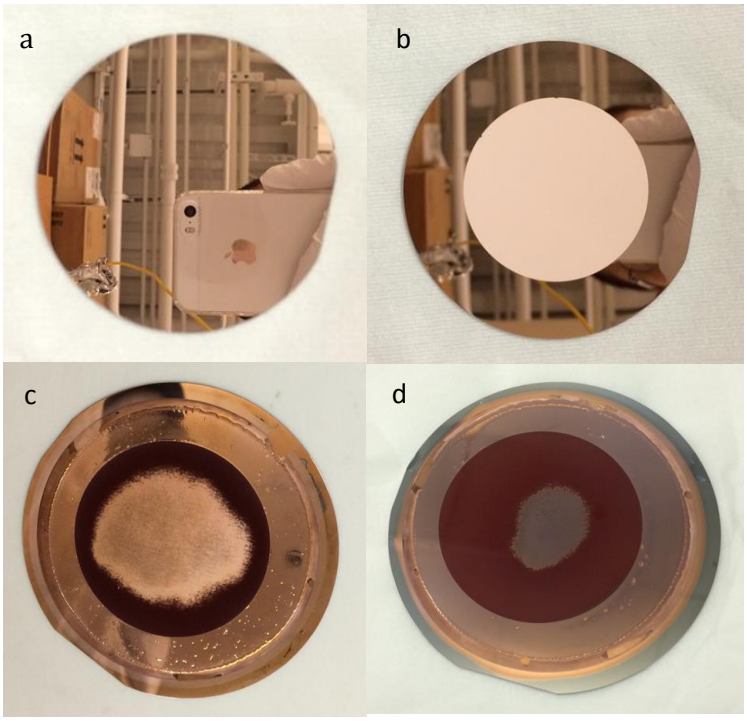

Figure 4.3: (a) The sample before CMP. (b) The sample after 10 mins of CMP using Fujimi Metal Polish No. 2. (c) The sample after 25 mins of CMP using Fujimi Metal Polish No. 2. (d) The sample after 30 mins of CMP using Fujimi Metal Polish No. 2.

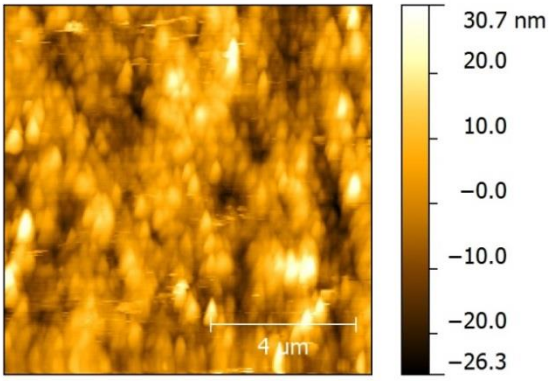

Figure 4.4: A typical AFM topography of the dark red areas of the samples shown in Figure 4.3(d).

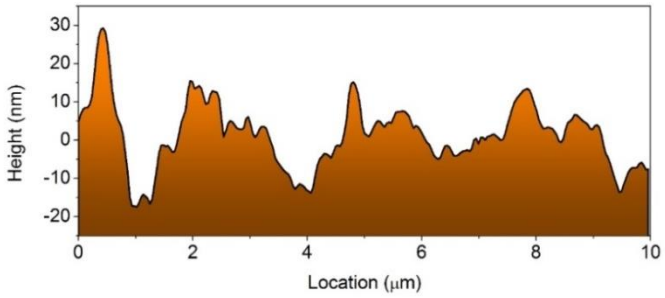

Figure 4.5: A typical one dimensional profile of the AFM topography shown in Figure 4.4.

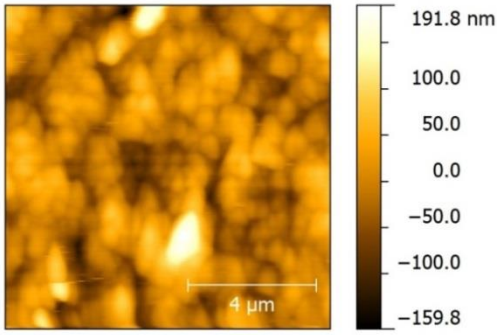

Figure 4.6: A typical AFM topography of the center areas of the samples shown in Figure 4.3(d).

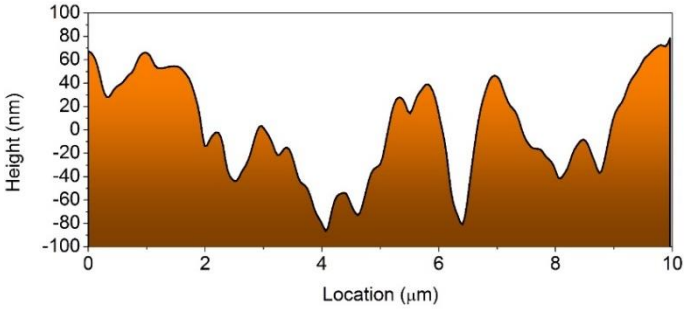

Figure 4.7: A typical one dimensional profile of the AFM topography shown in Figure 4.6.

As introduced in previous paragraphs, the surface roughness after polishing using Fujimi Metal Polish No.2 is still not satisfactory. Our goal is to polish the surface roughness to less than 10 nm. In order to further lower the surface roughness of the polished samples as well as to increase the polishing efficiency, chemical effects needs to be introduced. Meanwhile, smaller abrasive particle size should also result in lower roughness.

So, we switch to commercially available ready-to-use slurry, Ultra-Sol A20 (Eminess), which is specially developed for aggressive CMP processes of different types of metals. It also declares good performance in processes where the metal and alumina coexist in the same layer, which complies very well with the situation of our sample. The pH value of this slurry is 4.0, and the mean abrasive particle size is 240 nm. As shown in Figure 1, both the polishing efficiency and quality are visibly enhanced. After polishing, the roughness of the dark red ring-shape area and the copper covered center area of the sample (as shown in Figure 6(d)) is characterized by AFM, respectively. The roughness of the areas where the copper nanowires get exposed is measured to be within 15 nm (as shown in Figures 7 and 8), while the roughness of the copper covered center area is measured to be within 5 nm.

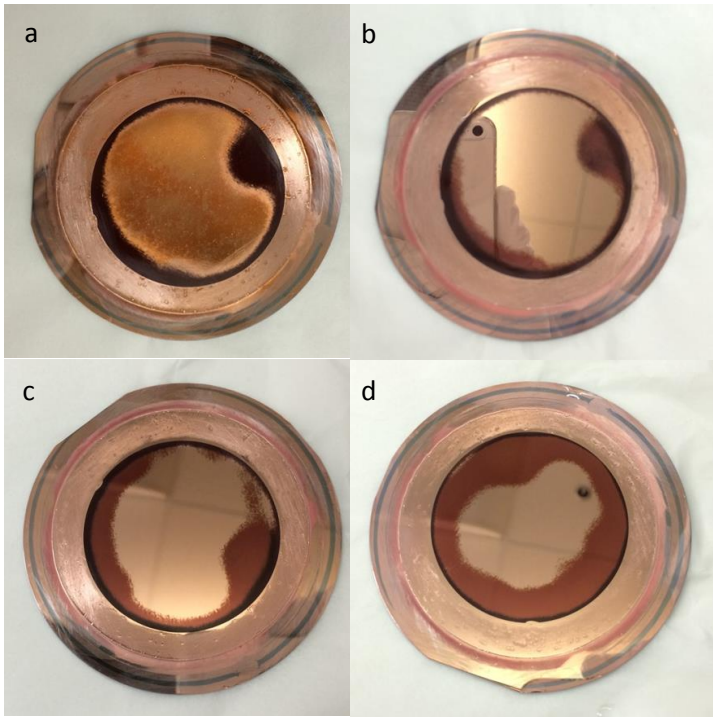

Figure 4.8: (a) The sample before CMP. (b) The sample after 2 mins of CMP using Eminess Ultra-Sol A20. (c) The sample after 7 mins of CMP using Eminess Ultra-Sol A20. (d) The sample after 12 mins of CMP using Eminess Ultra-Sol A20.

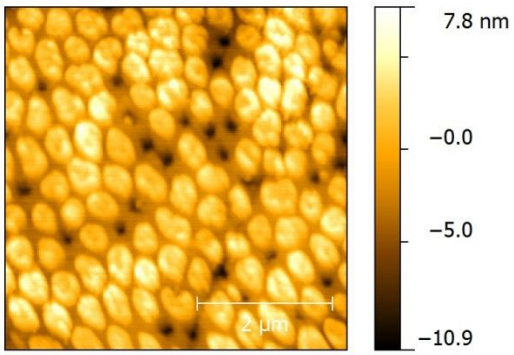

Figure 4.9: A typical AFM topography of the dark red areas of the samples shown in Figure 4.8(d).

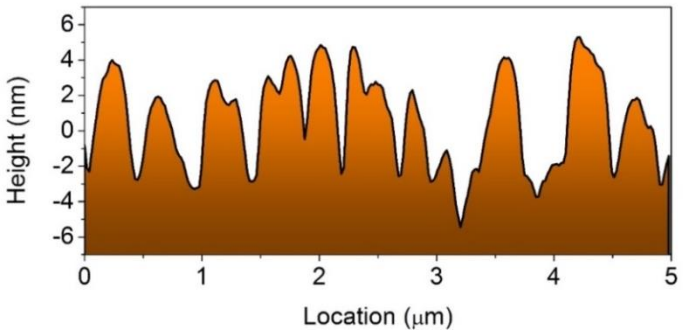

Figure 4.10: A typical one dimensional profile of the AFM topography shown in Figure 4.9.

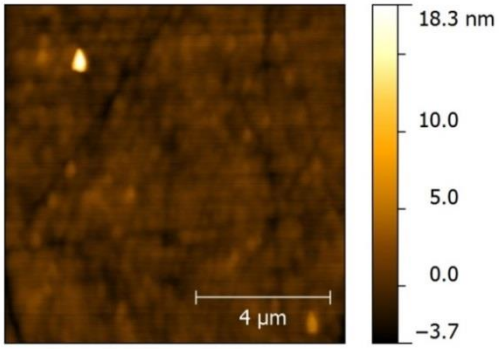

Figure 4.11: A typical AFM topography of the center areas of the samples shown in Figure 4.8(d). The white spot should be the particle from contamination.

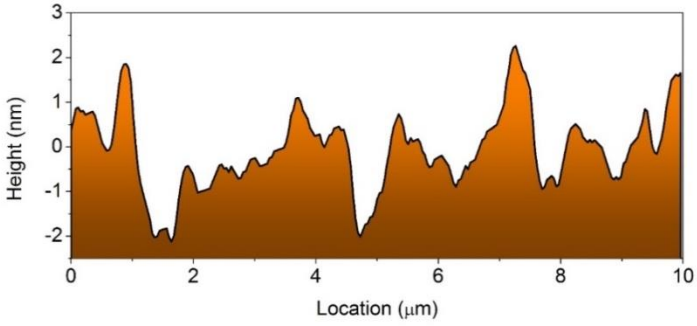

Figure 4.12: A typical one dimensional profile of the AFM topography shown in Figure 4.11.

4.3.3 Etching of the AAO templates

Because of the requirement of the experiment, structures with nanowires array protruding from the surface and structures with nanowires totally released need to be fabricated. In the following two paragraphs, I'll introduce how to carry out partial etching and complete etching of alumina template respectively.

At the very beginning, dry etching is our first choice because it provides better controllability. Considering that nickel is usually used as the mask in Reactive Ion Etching (RIE) and alumina can be etched by use of chlorine, I tried out Inductively Coupled Plasma (ICP) RIE first. A gas flow of 35 sccm Cl_2/15 sccm Ar is applied with a bias power of 100W and an ICP power of 600W. Figure 4.16 shows the SEM image of the originally polished sample surface after 300 s of ICP RIE. As shown, the nickel nanowires are severely etched, apparently the etching selectivity between the nickel and alumina is not high enough. I believe that if we keep trying different parameters, better etching selectivity can be achieved. But, it is not promising to achieve extremely high etching selectivity. Moreover, considering the fact that wet etching experiment has given us satisfactory result, ICP RIE is not continued. The procedure of wet etching will be introduced in detail in the following paragraph.

In the end, we chose controlled wet etching to partially remove the alumina template. Wet etching was conducted in the 0.5M NaOH solution at the temperature of ~30 °C. NaOH of this concentration is chosen after multiple etching test using solutions with different concentration. It turns out that: if the solution concentration

was too high, the etching rate will to fast to control; if the solution concentration is too low, the etching uniformity will deteriorate. Figures 4.14 (a) and (b) are the SEM images of nanowire arrays after being etched for 3 minutes and 5 minutes. The average lengths of the protruded nanowires are measured to be ~150 nm and ~400 nm, respectively. Since the roughness of the polished surface can normally reach < 5 nm after planarization, the height uniformity of nickel nanowires can be ensured.

The nanowire arrays can be completely released by dissolving the AAO template in a NaOH aqueous solution. Figure 4.15 is SEM image of those completely released nanowire arrays after being dried naturally in the air. As shown, nanowires fall into bundles after the natural drying process. This is attributed to the surface tension introduced by the phase change. During the usual drying process, the liquid changes into gas in a finite rate. In this process, the liquid will exert a force to pull any structure that is in contact with the liquid/gas interface. To prevent the nanowires from falling to each other, the gradual phase change process needs to be avoided. So, supercritical drying is applied to dry the completely released nanowire arrays.

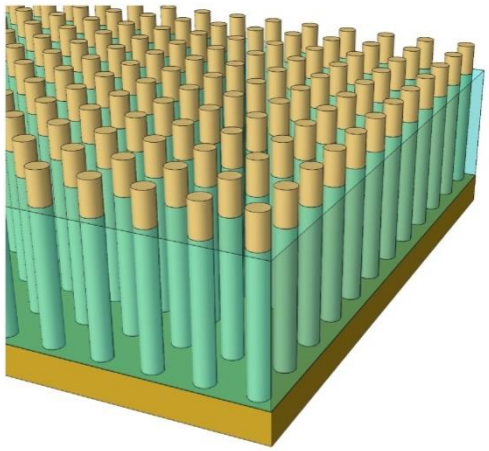

Figure 4.13: Schematic of partially released nanowire arrays. The protruded nanowires are measured to be ~400 nm from the AAO template.

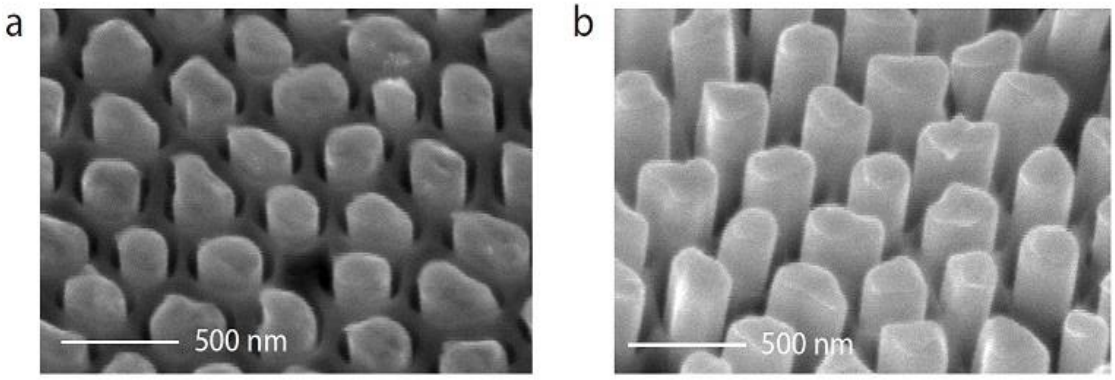

Figure 4.14: SEM images of samples after the wet etching in 0.5M NaOH solution: (a) after 3 minutes etching, and (b) after 5 minutes etching.

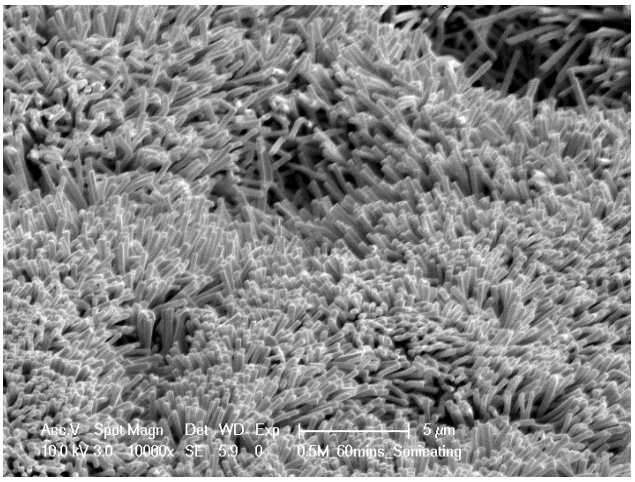

Figure 4.15: SEM images of samples after the wet etching in 0.5M NaOH solution for 2 hours and then dried naturally in the air. Nanowires bundle into each other because of the surface tension during the drying process.

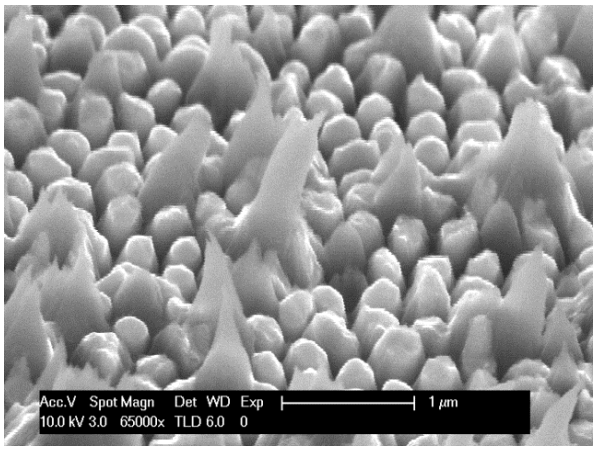

Figure 4.16: SEM images of polished sample after ICP RIE, which shows the etching selectivity between nickel and alumina is not satisfactory.

4.4 Measurement results and discussion

We demonstrate near-field thermal extraction by measuring the radiative heat transfer between a microsphere and a substrate at nanoscale gaps. To prepare the near-field thermal probe, a 100 μm diameter SiO_2 (glass) microsphere is attached to the tip of a bi-material (SiN_X/gold) atomic force microscope (AFM) cantilever, which can resolve heat power as small as 0.1 nW because of the bi-metallic effect[32][33]. A laser beam is used to measure the deflection of the cantilever and heat the microsphere to ~50 °C, whereas the sample substrate is maintained at ambient temperature. When the sphere approaches the substrate, the heat flow radiated from the microsphere to the substrate greatly increases due to near-field heat transfer[11][21]. The resulting temperature change of the sphere causes the bending of the cantilever that is further monitored and measured using an optical deflection system. In our experiment, the gap

between the sphere and the substrate is continuously reduced at a speed of 20 nm/s in order to minimize the influence of thermal drift of the AFM cantilever. The deflection signal of the cantilever, which also represents the near-field heat transfer signal, increases as the gap decreases with time. The sharp change in the slope of cantilever deflection signals indicates the mechanical contact between the sphere and the substrate, thereby providing a reference to precisely determine the substrate-sphere separation. All important details about the experiment setup have been introduced in Chapter 2.

To fabricate the MWAs based HMs, we employ anodic aluminum oxide (AAO) nanoporous templates to grow vertically aligned metal nanowires via electrochemical deposition[69][81][82]. Figures 4.17 (a) and (b) show nickel nanowire arrays embedded in an AAO template. To prove that MWAs do not participate in heat transfer as a passive waveguide, we measure the near-field radiative heat flux between the SiO_2 microsphere and bare nickel nanowire arrays in vacuum supported on a ~ 30 μm thick nickel film. The length and the diameter of the nickel nanowires are ~10 μm and ~ 300 nm, respectively. The separation between the nanowires is ~100 nm on average (Figure 4.17(c) upper left inset). The temperature difference between the SiO_2 sphere and the nickel nanowires was calibrated to be 29 K. As a polar dielectric, SiO_2 supports resonant surface phonon polariton modes and serves as a super-Planckian near-field absorber/emitter (with a very large PLDOS close to its surface)[11]. The nickel film beneath the nanowires performs as a mirror - an extremely inefficient thermal emitter/absorber.

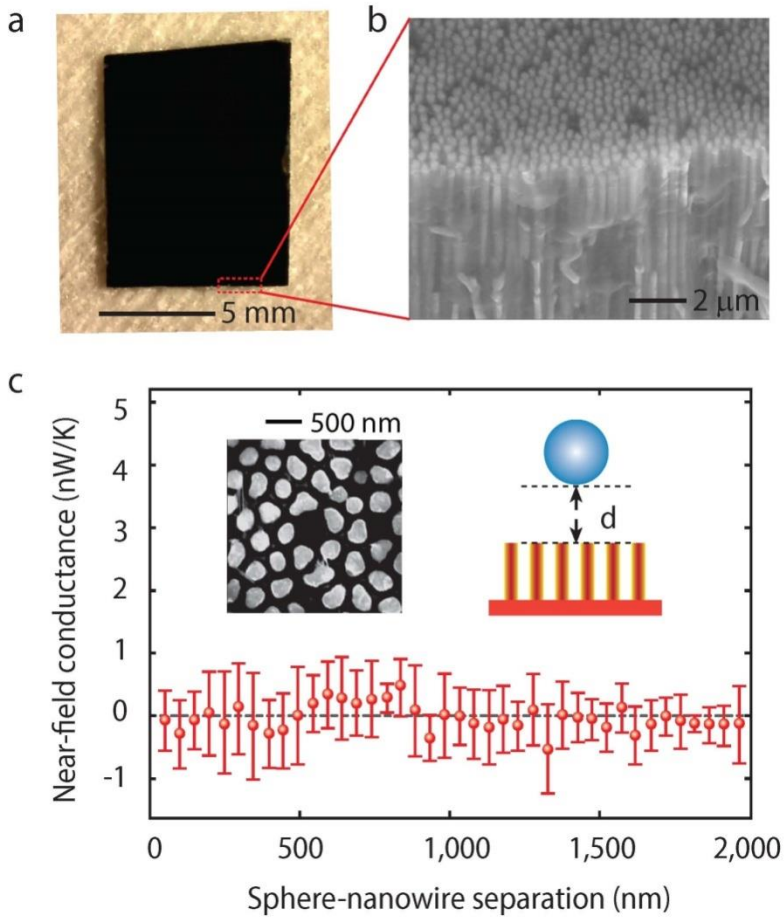

Figure 4.17: Fabrication of a HM composed of MWAs and its application as low-loss waveguides. (a) Optical image of the polished nickel nanowire-AAO composite. (b) SEM image of the side view of the polished sample shown in (a). (c) Near-field heat transfer between a SiO_2 sphere and free-standing nanowire arrays as a function of nanowire-sphere separation. The dashed line indicating zero near-field conductance is drawn for eye guidance. The upper left inset is the SEM image of the top view of free-standing nanowires, where the nanowires are well separated from each other after supercritical drying.

It has been demonstrated that the near-field heat transfer between a SiO_2 sphere and a metal surface is almost zero[11]. If substantial heat transfer occurs between the SiO_2 sphere and the nickel nanowires, it must be attributed to the contribution from the nickel nanowires rather than the 30 μm thick nickel film. However, there is no obvious heat transfer observed in Figure 4.17(c), where the measured near-field thermal conductance is plotted as a function of the separation between the nanowires and the sphere. This is because the nanowires are low-loss for thermal radiation, and therefore the propagating waves along the 10 μm long nanowires have negligible dissipation. On the other hand, when the non-decaying propagating waves reach the highly reflective nickel film at the end of the nanowires, they will be almost totally reflected. As a result, the measured near-field heat transfer is close to zero, even at a sphere-nanowire separation smaller than 50 nm. Our measurements clearly demonstrate that nickel nanowire arrays can work as a passive lossless waveguide for thermal radiation.

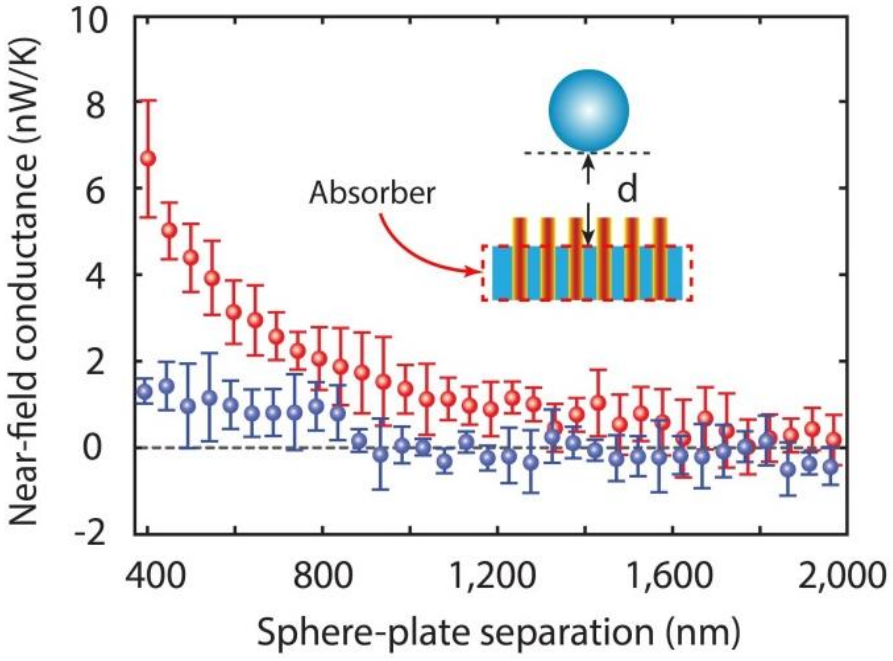

Figure 4.18: Near-field heat transfer as a function of the gap between the sphere and the AAO template with (red dots) and without (blue dots) the protruded nanowires. The dashed line indicating zero near-field conductance is drawn for eye guidance. The separation between the sphere and the substrate (AAO template) ends at ~ 400 nm because of the protruded nanowires.

We experimentally investigate near-field thermal extraction by connecting MWAs with a lossy thermal emitter/absorber instead of a metal mirror in the above case. The sample is prepared by partially etching the AAO template in a NaOH solution (as shown in Figure 4.14(b)). The rest portion of the nanowires together with the alumina template (dashed red box in Figure 4.18 inset) serves as a high-performance thermal absorber. The absorptivity of the nickel nanowire/alumina composite is mainly attributed to two effects: (1) the intrinsic surface phonon-polariton resonance of alumina leads to the strong enhancement of photon local density of states (PLDOS) at the resonance frequencies; (2) the embedded nickel nanowires provide broadband hyperbolic modes, which in general enhance the PLDOS at the non-resonating frequencies. To demonstrate near-field thermal extraction effect, we measure the near-field heat transfer with/without the protruded nickel nanowires as a thermal extractor. In Figure 4.18, where near-field thermal conductance is plotted as a function of the gap d between the SiO_2 sphere and the AAO template (substrate) (Figure 4.18 upper right inset), the HM thermal extractor (i.e., ~400 nm long nanowires) can dramatically enhance near-field heat transfer. At the smallest separation (~10 nm) between the sphere and the nanowires that corresponds to d~400 nm, the measured thermal

conductance with the protruded nanowires is ~ 7 nW/K, which is around one order of magnitude larger than the case without the protruded nanowires (~1 nW/K). This result demonstrates the excellent near-field thermal extraction performance of MWAs. It is worth to note that in order to demonstrate the near-field thermal extraction effect of MWAs, the near-field emitters and absorbers can be arbitrarily chosen. The thermal absorber made from the nanowire/alumina composite in this work only serves as one example without losing generality.

Here, we want to emphasize that near-field thermal extraction of MWAs is independent of the material properties of emitters/absorbers. For any thermal emitters/absorbers, such as a lossy AAO template or a SiO_2 sphere in this work, they all support thermally excited evanescent waves. The evanescent modes can be surface polariton modes for polar dielectrics or metals, or non-resonant evanescent modes for other materials. When the emitter and the absorber are separated by a large gap compared to the wavelength of thermal radiation, all these evanescent modes exponentially decay from surface and have no contribution to heat transfer. However, if a HM (e.g., MWAs) is optically contacted with the emitter and placed between the emitter and the absorber, the evanescent modes from the emitter can be converted into the propagating modes in the HM, and then transfer energy to the absorber via the near-field coupling between the HM and the absorber. Hence, radiative heat transfer can be greatly enhanced by the extracted evanescent modes. And the extracted evanescent wave travels along the nanowire surface in a wave guiding mode. And the electric and magnetic field of this wave guiding mode are tightly confined along the

surface of those nanowires. Although we only demonstrate near-field thermal extraction using ~400 nm long nanowires in this work, thermal extractors made from MWAs are expected to maintain good extraction performance for much longer nanowires (e.g., 10 μm long nanowires) as well because of the low-loss waveguide modes in MWAs (Figure 4.17(c)).

4.5 Summary

In summary, the concept of HMs is briefly introduced at the very beginning of this chapter. Based on that, HMs' properties which is relevant to near field radiation is investigated. After laying the necessary theoretical foundation, I introduced in detail the procedures of fabricating nanowire array base HMs, including electrodeposition, CMP, wet etching, and etc. After getting the sample prepared, the near field radiation measurement is carried out correspondingly. We successfully demonstrate a HMs mediated energy extraction device that can significantly enhance near-field heat transfer by about one order of magnitude. In particular, the HMs made from MWAs are low-loss for thermal radiation, and perform as a passive and transparent pipe guiding radiative energy. This work opens up a myriad of new thermal applications based on metamaterials. The high thermal extraction with HMs can be exploited to develop a variety of technologies ranging from thermophotovoltaic energy conversion to thermal imaging.

5 Tuning near field radiation using thin metallic film coatings

5.1 Overview

In preceding two chapters, I introduced two different schemes to realize near field energy coupling. In Chapter 3, the evanescent waves near the surface of emitters are demonstrated to couple into surface waves supported by doped silicon[41][83]. In Chapter 4, the evanescent waves are shown to couple into a continuum of propagating wave inside HMs[84][85]. Although these two different schemes provide promising solutions to increase the near field radiation, they both suffer from inherent limitations. For the case that relies on coupling into the surface wave mode, it requires that the substrate supports surface waves such as surface plasmon polaritons or surface phonon polaritons. However, only a small portion of materials in real industry can support surface polaritons. And, those surface wave enhanced near field radiation is confined in very narrow bandwidth at the resonant wavelength. For the scheme that makes use of the large propagating wave vector mode in HMs, it requires multiple nanofabrication steps to prepare the HMs. And, this method is highly costly and very difficult to fabricate structures with large areas. Motivated by the limitations of those previously mentioned methods, scientists have always been seeking for better schemes that could provide higher efficiency of near field radiation enhancement and lower requirement on fabrication. This goal still looks very difficult to reach until very recently that huge progresses have been made on the investigation of the near field

radiation properties of thin dielectric films and thin metallic films. Motivated by those progresses, I've also proposed and carried out some investigations on this topic. This chapter features on the emerging scheme of realizing the near field radiation enhancement by use of the thin metal films.

To have a better understanding of the motivation of this work as well as its position in the whole field, it is necessary to first give a brief review of recent progresses in this realm. The near field thermal radiation properties of both metal and dielectric thin films have been investigated systematically in the past decade[37][38][86][87]. M. Francoeur et al investigate the difference between a 10 nm thick SiC slab and a SiC bulk using fluctuation electrodynamics. Their calculation results show the near field radiative flux can be increased by a factor of 3.3 after coating the material with a 10 nm thick SiC thin film[88][89]. Such near field radiative enhancement is attributed to the splitting of the resonant frequency into two different frequencies. Similarly, ultrathin metal films are also shown to emit stronger near field radiation due to the splitting of the original resonance frequency[86][90]. Considering the fact that chapter 4 focuses on realizing the near field radiation using metamaterials, there is a recent theoretical publication that perfectly bridges my work introduced in Chapter 4 and the work I'm going to introduce in this chapter. The authors have compared the efficiency of using HMs and using ultrathin metallic films[90]. According to their calculation results, ultrathin metallic films can have comparable or even larger PLDOS as HMs.

Except progresses on theoretical calculation, there are already some initial progresses on the experimental side. Here, I'll introduce two recent experimental works on investigating the near field radiation properties of dielectric thin films and metallic thin films[24][91]. Bai Song et al experimentally demonstrated that thin polar dielectric films with a thickness of 50-100 nm exhibit near field radiative heat transfer comparable to bulk polar dielectrics when the distance between emitter and the thin film is comparable to the film thickness. In parallel, researchers have also carried out experimental investigation on the radiation properties of thin metallic films. Zhu Wang et al demonstrate that the far field emissivity of metal can be greatly enhanced by making the film ultrathin (2 nm)[91]. They attribute such far field radiation enhancement to the suppression of the screening effect which absorbs the internally generated electromagnetic waves so that electromagnetic waves cannot travel out of the bulk metal. However, as the counterpart of the far field radiation properties, the near field radiation properties of ultrathin metallic films still haven't been experimentally investigated, which gives me strong motivation to pursue this work.

In this chapter, I'll first introduce the theoretical foundations for calculating the near field radiation from ultrathin metal films. Then, the calculation results will be introduced and discussed. After the theoretical analysis, the procedures for sample preparation will be introduced. In the end, the measurement result will be demonstrated and discussed.

5.2 Theoretical analysis of the near field radiation from ultrathin metallic films

5.2.1 Surface plasma on the ultrathin metal films

In section 1.2, I've introduced the method of calculating the dispersion relation for surface plasmon polaritons on a single interface. Using a very similar method[12][13], the dispersion relation for surface plasmas along the ultrathin metal films can also be calculated. Here is the implicit dispersion relation that connects k_1, k_2 and k_3:

$$e^{-4k_1 a} = \frac{k_1/\varepsilon_1 + k_2/\varepsilon_2}{k_1/\varepsilon_1 - k_2/\varepsilon_2} \frac{k_1/\varepsilon_1 + k_3/\varepsilon_3}{k_1/\varepsilon_1 - k_3/\varepsilon_3} \quad [66]$$

For the case that $\varepsilon_2 = \varepsilon_3$ and $k_2 = k_3$, equation [66] will be split into two equations

$$\tanh k_1 \varepsilon_1 = -\frac{k_2 \varepsilon_1}{k_1 \varepsilon_2} \quad [67]$$

$$\tanh k_1 \varepsilon_1 = -\frac{k_1 \varepsilon_2}{k_2 \varepsilon_1} \quad [68]$$

By applying Equation [67] and Equation [68] to the cases of IMI (insulator /metal/insulator) and MIM (metal/insulator/metal) structures, the dispersion relation of the two split modes of surface plasmon polariton can be obtained respectively. One mode has frequencies higher than the plasmon frequency for a single interface, and it corresponds to the odd mode; the other mode has lower frequencies than the plasma frequencies for a single interface, and it corresponds to the even mode. The following

two equations gives the frequencies of the odd mode and even mode of the coupled plasmon polaritons[12].

$$\omega_+ = \frac{\omega_p}{\sqrt{1+\varepsilon_2}}\sqrt{1+\frac{2\varepsilon_2 e^{-2\beta a}}{1+\varepsilon_2}} \quad [69]$$

$$\omega_- = \frac{\omega_p}{\sqrt{1+\varepsilon_2}}\sqrt{1-\frac{2\varepsilon_2 e^{-2\beta a}}{1+\varepsilon_2}} \quad [70]$$

The splitting of one plasmon frequency to two frequencies could potentially provide more near field radiation channels. For ultrathin metallic films, the frequency of the even mode will be dramatically lowered when compared with the original frequency for the single interface case. In our experiment, since the surface phonon polariton is usually in the infrared range, a lower frequency of the even mode might lead to stronger energy coupling between the surface phonon polariton of the microsphere and surface plasmon polariton of the ultrathin metallic films.

5.2.2 Results of the theoretical calculation

In Chapter 1, it is already introduced in detail that the Dyadic Green's Functions method and the fluctuation dissipation theorem can be used to calculate the near field radiative heat flux. However, instead of dealing with semi-infinite plane, here we are dealing with more complicated multilayer structure (SiO_2/Vacuum/Pt/Si). In the case of such one-dimensional multilayer geometry, a general method to obtain the Dyadic Green Function(DGF) is to use a plane wave representation[92][93]:

$$\bar{G}(r, r', \omega) = \int_{-\infty}^{\infty} \frac{dk_\rho}{2\pi^2} \bar{g}(k_\rho, z_c, z', \omega) e^{ik_\rho (R-R')} \quad [71]$$

where $k_\rho = k_x\vec{x} + k_y\vec{y}$, $dk_\rho = dk_x dk_y$, $R = x\vec{x} + y\vec{y}$, and $\bar{g}$ is the Weyl component of the DGF. The Weyl component of the DGF can be conveniently calculated by use of the Scattering Matrix Method[94][95].

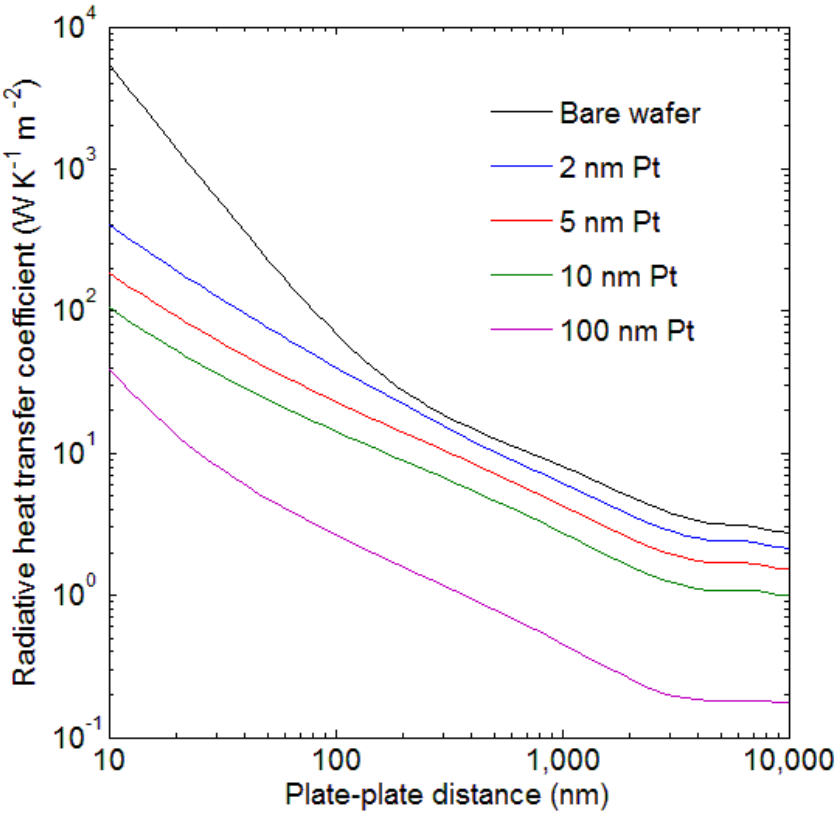

Figure 5.1: Calculated radiative heat transfer coefficient curves corresponding to doped silicon substrate without coating and with Pt coatings of different thickness (2 nm, 5 nm, 10 nm and 100 nm). *Courtesy of Francisco Ramirez.*

Figure 5.1 shows the radiative heat transfer coefficient versus the gap size between two parallel semi-infinite plates. It turns out that the doped silicon substrate

provides the strongest near field radiation signal when interacting with SiO_2. When the Pt film becomes thicker (from 2nm to 5nm until 100 nm), you can see a clear decreasing trend of the radiative heat transfer coefficient. This can be explained by the screening effect. Pt film here serves as a near field radiation attenuator: the thicker the film, the more attenuated the near field radiation. By applying the Derjaguin approximation, the radiative heat transfer coefficient can be easily converted to the near field conductance between the SiO_2 microsphere and the sample plate (as shown in Figure 5.2).

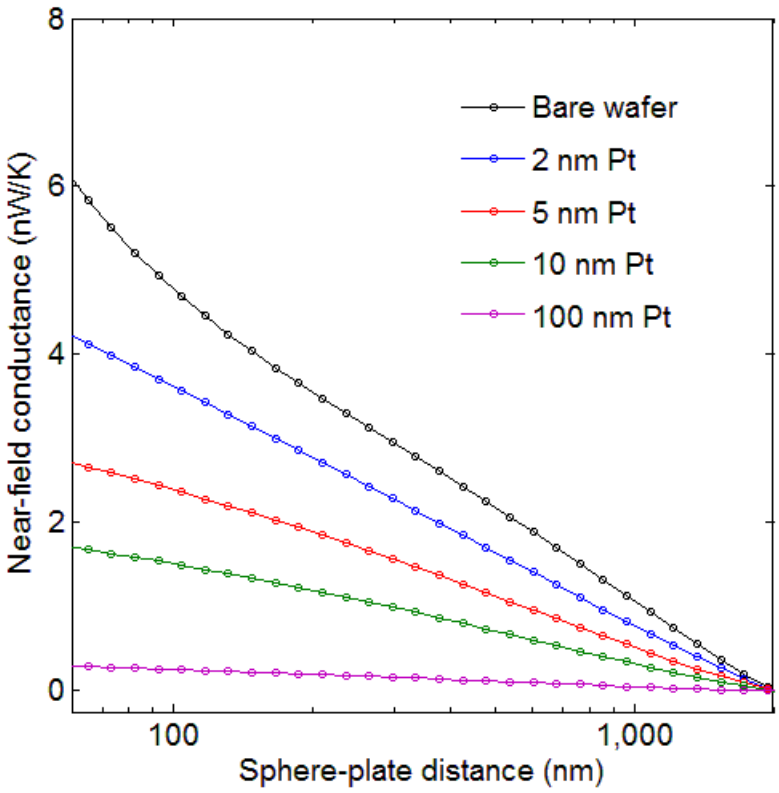

Figure 5.2: Calculated near-field conductance curves corresponding to doped silicon substrate without coating and with Pt coatings of different thickness (2 nm, 5 nm, 10 nm and 100 nm). *Courtesy of Francisco Ramirez.*

5.3 Sample preparation

Since the near field radiation measurement system is already set up, to carry out the experiment, ultrathin metallic films with a thickness as thin as 2 nm need to be prepared. Due to the ultrathin film thickness, it requires that the deposition must be a slow process. Sputtering, Electron beam physical vapor deposition (EBPVD) and atomic layer deposition (ALD) are all good candidates for depositing ultrathin metal films. Although in the end I chose sputtering, I spent some time investigating different options. Here, I'd like to give some brief comments on those three techniques for future reference.

ALD is one of the best choices for thin film deposition in the range of 1-200 nm, which is a two-step self-limiting process[94][95]. Ideally, by adjusting the ALD cycle times, it could provide the film thickness controllability down to the single atom layer thickness. A large number of thin-film materials can be grown by ALD. However, it does not provide many choices on metal except W, Cu, Pt, etc. Lots of common metals, such as Au, Al, Ni, are not available for ALD due to the unavailability of proper precursors. The CMU cleanroom possesses one ALD system (Cambridge Nanotech Fuji ALD system). However, they only provide oxide deposition such as Al_2O_3, SiO_2, HfO_2, and TiO_2. Even Pt deposition is not available.

For EBPVD, one of the most important characteristics is its deposition rate can be adjusted in a broad range, which can be as low as 1 nm per minute and as high as few micrometers per minute. The deposition material of EBPVD is not confined by the

availability of the precursors as in ALD, so EBPVD provides more metal choices: gold, silver, copper, nickel, chrome are all available.

Similar to EBPVD, sputtering also provides lots of choices for metal deposition[98]. The operation of sputtering is more convenient when compared with EBPVD, and it has lower requirement on the vacuum level compared with EBPVD. It should be pointed out that EBPVD can produce samples with higher purity. Considering the accessibility of the facilities, the Perkin Elmer 6J sputtering system was used in this experiment. By lowering the plasma power, the deposition rate of Pt can be adjusted to be as low as 1-2 Å/s. Rate run is carried out before the real sputtering. Kapton tape was applied on top of the bare wafer before the rate run sputtering so that it will create a step for the profilometer measurement after the sputtering. With an argon bleed pressure of 5 mTorr and a plasma power of 15 W, the deposition rate of Pt is measured to be 1.37 Å/s[95][96]. After obtaining the deposition rate, the deposition time for the required film thickness can be calculated, for example, it takes ~22 seconds to deposit a Pt film with a thickness of 3 nm, which is long enough for time control.

In order to obtain a metal film with extremely low roughness, a substrate with extremely low roughness is preferred. Here, a boron doped silicon wafer with a hole concentration of $\sim 3.1\times10^{19}/cm^3$ is chosen as the substrate. And its surface has been well polished. Figure 5.3(a) shows the surface topography before sputtering. Considering that there could be ~1 nm thick native oxide layer on top of the silicon

wafer, buffered oxide etching (BOE) was applied to remove the native oxide layer before the sputtering[101]–[103]. Figure 5.3 (b)-(d) show the topographies of the sample after being sputtered with Pt with a thickness of ~2.7 nm, ~5.5 nm, and ~100 nm. The Pt film thicknesses of the first two samples are all measured using XRR[104], which is consistent with the thickness estimation from deposition rate obtained from the rate run.

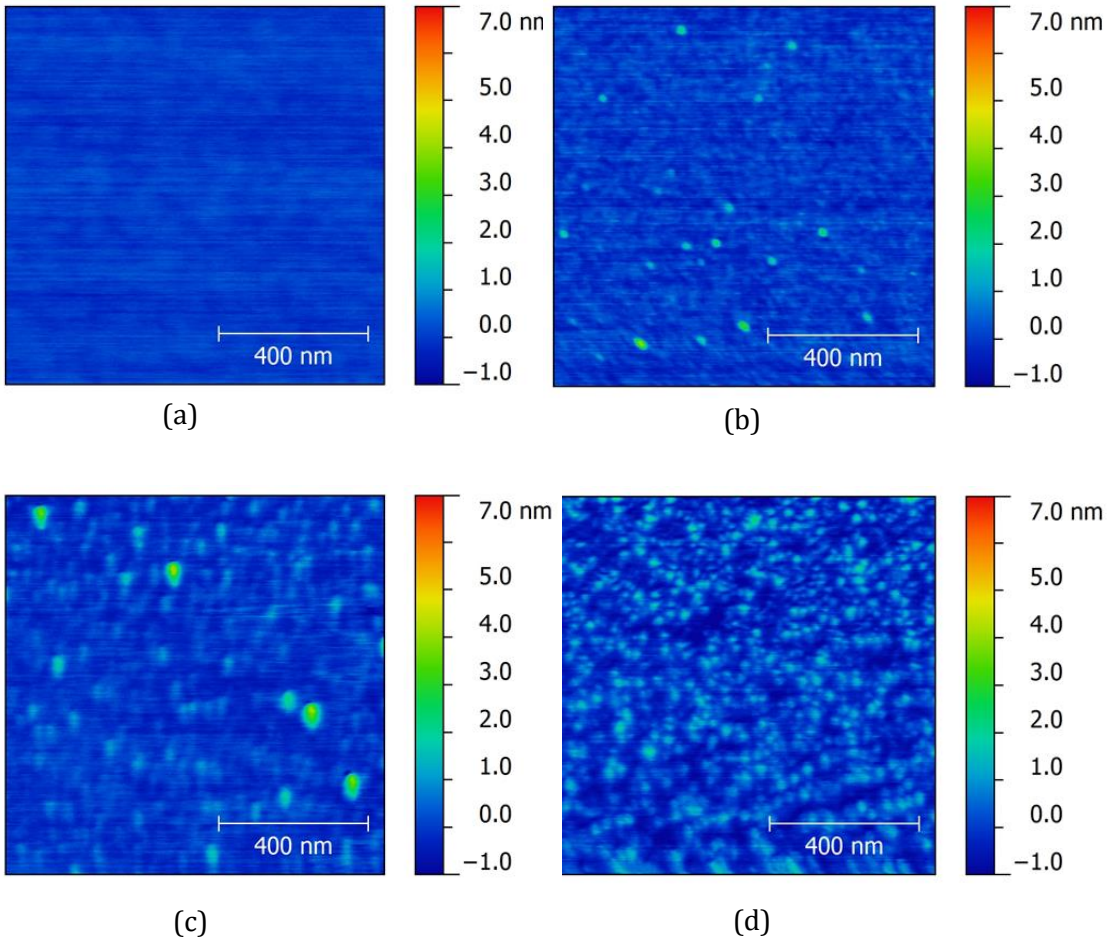

Figure 5.3: (a) Surface topography of polished bare wafer. (b) Surface topography, after being coated with ~2.7 nm thick Pt. (c) Surface topography, after being coated

with ~5.5 nm thick Pt. (d) Surface topography, after being coated with ~100 nm thick Pt.

5.4 Measurement results and discussions

After the deposition of Pt films, the wafers are cracked into small squares, and those small square samples are attached on to a copper plate using silver epoxy. All samples are aligned vertically along the edge of the copper plate. Then the copper plate is loaded into the near field radiation measurement setup, which is already introduced in detail in Chapter 2.

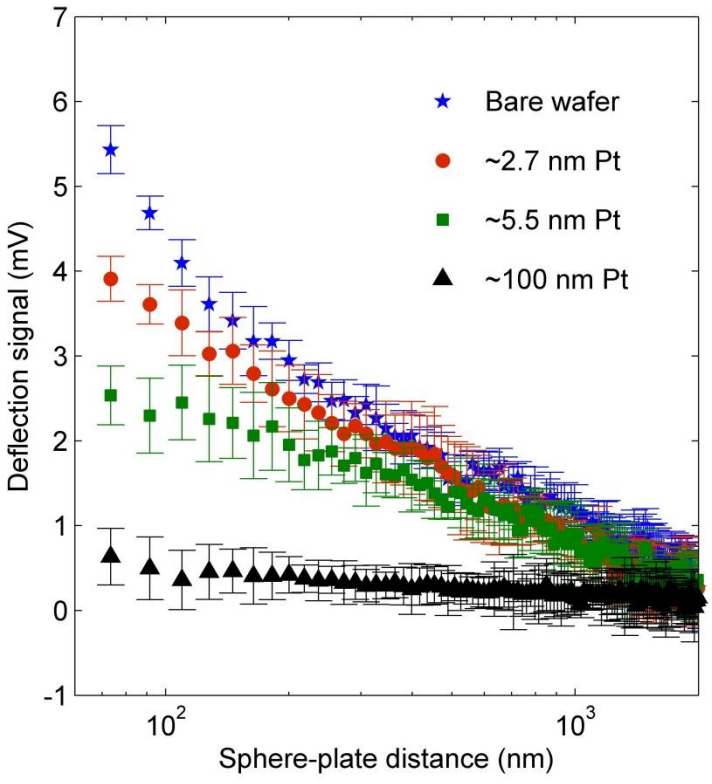

Figure 5.4: Cantilever deflection signal corresponding to doped silicon substrate without coating and with Pt coatings of different thickness (~2.7 nm, ~5.5 nm and ~100 nm).

Figure 5.4 shows the cantilever deflection signal between the SiO_2 microsphere and the doped silicon substrate without coating or with Pt coatings of different thicknesses (~2.7 nm, ~5.5 nm and ~100 nm). It is observed that the thicker the Pt coating, the weaker the near-field radiation. The doped silicon wafer substrate provides the strongest near field radiation signal. After depositing a ~2.7 nm thick Pt film, the near field radiation is reduced (red dots). By further increasing the Pt film thickness to ~5.5 nm, the near field radiation is further reduced (green dots). When the Pt film is as thick as ~100 nm, the optical properties of film can be considered as that of Pt bulk, so its near field radiation signal is very weak (black dots).

One apparent conclusion we can draw from the above measurement result is: ultrathin metallic film coatings can be applied to tune the near field radiation, and the tuning extent can be adjusted by changing the film thickness. The thinner the metallic film, the stronger the near field radiation signals. This might be attributed to the screening effect of metals. Metals have very strong absorption to electromagnetic waves. The thicker the metallic film, the better it could block the near field radiation signal from the doped silicon substrate. Another possible explanation for the near field radiation enhancement from reducing the thickness of metallic films is related to mode splitting of the surface plasmon polaritons along the ultrathin metallic films. Since

metals have very strong screening effect to electromagnetic waves, it is highly possible that even an ultrathin metallic film as thin as ~2.7 nm is already able to block most of the electromagnetic waves from the substrate. In this case, the near field radiation enhancement in the process of reducing the film thickness from ~100 nm to ~5.5 nm and 2.7 nm can be mainly attributed to the mode splitting of the surface plasmon polaritons along the thin metallic film. For future experiment, in order to solidly verify the above explanations, it is necessary to carry out experiments on a substrate with lower near field radiation signal, so that the contribution from the ultrathin metallic film can stand out.

6 Summary and outlook

6.1 Conclusion and contributions

It has been proved that the near field radiation can break the blackbody radiation limit, so the radiation efficiency can be greatly enhanced. Researches in this realm have already had or might have huge impact in a variety of technologies, e.g., thermophotovoltaics, radiative cooling, thermal infrared imaging, and heat assisted magnetic recording (HAMR)[105][106]. My major research focus, as presented by the thesis, focuses on tuning the near field radiation by nanophotonic materials, which could pave the wave for real application.

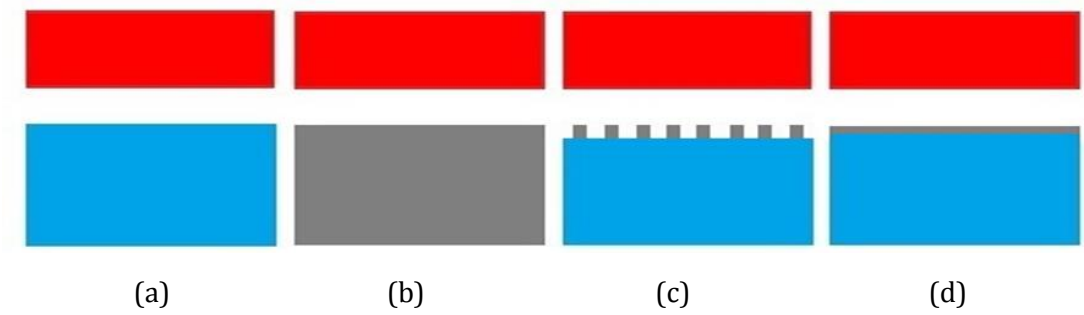

Figure 6.1: Near field radiation between surfaces made of different materials and with different topographies: (a) between dielectric and dielectric, (b) between dielectric and metal, (c) between dielectric and metal nanowires arrays, (d) between dielectric and ultrathin metallic films.

Figure 6.1 can best summarize the contribution of this thesis. I have tried different materials as well different structures to reach the goal of tuning the near field radiation.

As shown in Figure 6.1 (a) and (b), researchers have carried out the investigation of near field radiation properties of dielectric (SiC, SiO_2, etc) and metals, but the ability of tuning the intensity of the near field radiation is still extremely limited, which is the major motivation of my researches introduced in this thesis.

For the first project, I investigated both theoretically and experimentally the near field radiation properties of doped silicon at different doping concentrations. The surface plasmon polaritons of doped silicon can be adjusted by changing the carrier concentration of doped silicon. The peak of the PLDOS will shift dramatically at different doping concentrations, so the energy coupling between the doped silicon and other materials can be tuned by changing the doping concentrations. Considering the importance of silicon in semiconductor industry and the emerging importance of nanoscale thermal management in silicon based nanostructure, this research lays a solid foundation for applications in relevant realms.

In the second project, as shown in Figure 6.1 (c), the near field radiation properties of MWAs based HMs are investigated. HMs has an amazing property that its dispersion relation could accommodate infinitely large propagating wave vectors. In this project, electroplating was used to grow vertically aligned metal nanowires arrays from the AAO template. Then, CMP is employed to make the sample surface smooth and flat. In the end, wet etching is carried out to partially remove the AAO template so that nanowires could protrude from the template without falling to each other. The measurement results show that MWAs based HMs could serve as an efficient near field energy extraction device.

Considering the complicated steps and the high cost of fabricating nanostructure on the surface of the materials, I was motivated to investigate the near field radiation properties of ultrathin metallic films. The split surface plasmon polariton modes of the ultrathin metallic film are expected to have the effect of enhancing the near field radiative heat transfer. Magnetron sputtering was applied to deposit Pt films with different thickness on top of doped silicon substrate. Proper sputtering recipe has been tried out to deposit ultrathin Pt films. The experiment results show that the near field radiation can be tuned by changing the thickness of the Pt film. Further calculation and measurement are necessary to reach robust results.

6.2 Future research directions

Talking about future research directions, in my opinion, there are three major directions that are worth pursuing:

(1) Development of standard near field radiation measurement setups. For the present optical deflection based measurement setup, it is always a headache to adjust the setup in order to eliminate or suppress the electrostatic force, which occupies a big chunk of my experiment time. It's happy to see that, recently, Bai Song et al[24] made a big step forward to improve the measurement setup. But still, the system is not very user friendly. Moreover, all those sphere-plate based setups always involve a microsphere, which has become a major limitation of these setups. It is necessary to keep pushing the development of near field radiation measurement setups. The final goal should be that one day it will become a standard technique like AFM and SEM.

(2) Investigate near field radiation properties of new materials and develop materials or structures with new near field radiation properties. At the present stage, the near field radiation properties of lots of materials or structures are still unknown or unconfirmed, which is still a pretty active research realm. However, it should be noticed that there is apparently a transition from simply investigating or measuring the near field radiation to controlling and designing the near field radiation. On this recently emerged research topic, I believe there will be lots of interesting and meaningful development on the way

(3) Bring the near field radiation based technology to real life. This has been a long term struggle for researchers in this realm. Up to this point, except the application in HAMR and some initial application in thermophotovoltaics, there is very limited application of near field radiation in real life. With the development of other new technologies, I believe that there would be larger chance for near field radiation to make a bigger impact in real applications.

In the end, for the short term research plan, further calculation and measurement is still necessary to investigate the near field radiation properties of ultrathin metallic films. The emphasis would be to suppress the background radiation signal from the substrate, which can be potentially achieved by changing the substrate from doped silicon to other materials with much lower near field radiation signal.

APPENDICES

Appendix A: Weyl Components for layered media

In general, the Weyl components for a traveling wave detected inside the layer l at z_c, and generated from a point source at z' inside the layer s, are given by

$$\bar{\bar{g}}_{sl}^{E}(k_\rho, z_c, z', \omega)$$

$$= \frac{i}{2k_{zs}}\left[\begin{array}{l}\left(A_l^{TE}\,\hat{s}\hat{s} + A_l^{TM}\hat{p}_l^{+}\hat{p}_s^{+}\right)e^{i[k_{zl}(z_c - z_l) - k_{zs}z']} + \left(B_l^{TE}\,\hat{s}\hat{s} + B_l^{TM}\hat{p}_l^{-}\hat{p}_s^{+}\right)e^{i[-k_{zl}(z_c - z_l) - k_{zs}z']} \\ +\left(C_l^{TE}\,\hat{s}\hat{s} + C_l^{TM}\hat{p}_l^{+}\hat{p}_s^{-}\right)e^{i[k_{zl}(z_c - z_l) + k_{zs}z']} + \left(D_l^{TE}\,\hat{s}\hat{s} + D_l^{TM}\hat{p}_l^{-}\hat{p}_s^{+}\right)e^{i[-k_{zl}(z_c - z_l) + k_{zs}z']}\end{array}\right]$$

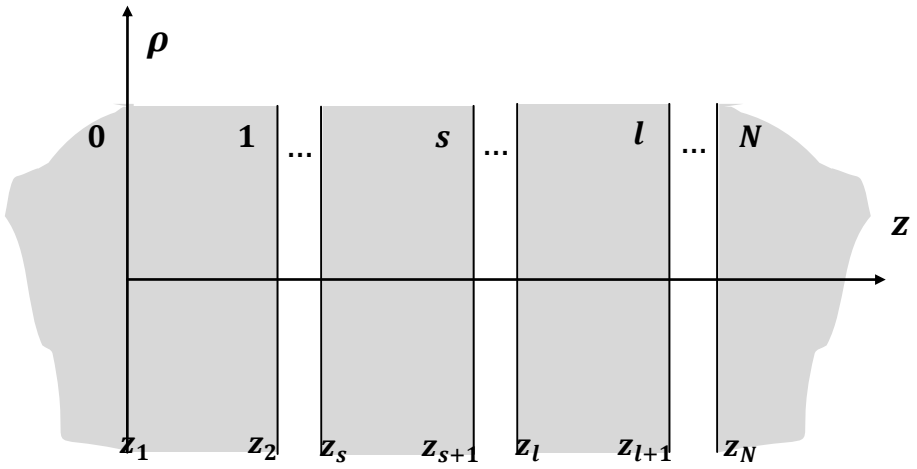

This general form consider waves of unit amplitudes that are emitted both in the forward ($-k_{zs}z'$) and backward direction ($+k_{zs}z'$). The coefficients A and B denote the amplitudes of forward and backward traveling waves, respectively, arising from a source emitting in the forward direction. Similarly, the coefficients C and D represent,

respectively, the amplitudes of forward and backward traveling waves generated by a source emitting in the backward direction. $\hat{p}$ and $\hat{s}$ represent the unit vectors of the TE and TM polarized waves, respectively.

Thus, the term $A_l^{TM}\hat{p}_l^+\hat{p}_s^+$, means that the forward traveling wave with polarization $\hat{p}_l^+$ and amplitude A_l^{TM} is observed in layer l due to a forward traveling wave emitted in layer s with polarization $\hat{p}_s^+$; the rest of the terms have a similar interpretation.

The magnetic Weyl representation of the DGF is found by $\bar{g}^H = \nabla \times \bar{g}^E$

$$\bar{g}_{sl}^H(k_\rho, z_c, z', \omega) = \frac{k_l}{2k_{zs}}\begin{bmatrix} \left(A_l^{TE}\,\hat{p}_l^+\hat{s} - A_l^{TM}\hat{s}\hat{p}_s^+\right)e^{i[k_{zl}(z_c-z_l)-k_{zs}z']} + \left(B_l^{TE}\,\hat{p}_l^-\hat{s} - B_l^{TM}\hat{s}\hat{p}_s^+\right)e^{i[-k_{zl}(z_c-z_l)-k_{zs}z']} \\ +\left(C_l^{TE}\,\hat{p}_l^+\hat{s} - C_l^{TM}\hat{s}\hat{p}_s^-\right)e^{i[k_{zl}(z_c-z_l)+k_{zs}z']} + \left(D_l^{TE}\,\hat{p}_l^-\hat{s} - D_l^{TM}\hat{s}\hat{p}_s^+\right)e^{i[-k_{zl}(z_c-z_l)+k_{zs}z']} \end{bmatrix}$$

These two expressions are valid whenever the point z_c lies outside the source ($l \neq s$).

The expression for the monochromatic radiative heat flux at z_c along the z direction in terms of the Weyl components of the DGF is:

$$q_{\omega,sl}(z_c) = \frac{k_v^2\theta(\omega, T_s)}{\pi^2}\,\mathrm{Re}\left\{i\varepsilon'' \int_0^\infty k_\rho dk_\rho \int_{z_s}^{z_{s+1}} dz'\,\mathrm{Tr}\left[\left(\bar{g}_{sl}^E \times \hat{z}\right)\cdot \bar{g}_{sl}^H\right]\right\}$$

BIBLIOGRAPHY

[1] F. P. Incropera, D. P. DeWitt, T. L. Bergman, and A. S. Lavine, *Fundamentals of Heat and Mass Transfer*, vol. 6th. John Wiley & Sons, 2007.

[2] S. Basu, Z. M. Zhang, and C. J. Fu, "Review of near-field thermal radiation and its application to energy conversion," no. April, pp. 1203–1232, 2009.

[3] K. Joulain, J.-P. Mulet, F. Marquier, R. Carminati, and J.-J. Greffet, *Surface Electromagnetic Waves Thermally Excited: Radiative Heat Transfer, Coherence Properties and Casimir Forces Revisited in the Near Field*, vol. 57, no. February 2008. 2005.

[4] A. Kittel, "Nanophotonics: Probing near-field thermal radiation," *Nature Photonics*, vol. 3, no. 9. pp. 492–494, 2009.

[5] K. Joulain, J.-P. Mulet, F. Marquier, R. Carminati, and J.-J. Greffet, *Surface Electromagnetic Waves Thermally Excited: Radiative Heat Transfer, Coherence Properties and Casimir Forces Revisited in the Near Field*, no. February 2008. 2005.

[6] A. J. Huber, B. Deutsch, L. Novotny, and R. Hillenbrand, "Focusing of surface phonon polaritons," *Appl. Phys. Lett.*, vol. 92, no. 20, 2008.

[7] A. Huber, N. Ocelic, D. Kazantsev, and R. Hillenbrand, "Near-field imaging of mid-infrared surface phonon polariton propagation," *Appl. Phys. Lett.*, vol. 87, no. 8, 2005.

[8] D. ~W. Pohl, "Near-Field Optics and the Surface Plasmon Polariton," *Near-f. Opt. Surf. Plasmon Polaritons, Ed. by Satoshi Kawata, Top. Appl. Physics, vol. 81, pp.1-13*, vol. 13, no. 81, pp. 1–13, 2001.

[9] A. V. Zayats, I. I. Smolyaninov, and A. A. Maradudin, "Nano-optics of surface plasmon polaritons," *Physics Reports*, vol. 408, no. 3–4. pp. 131–314, 2005.

[10] W. L. Barnes, "Surface plasmon–polariton length scales: a route to sub-wavelength optics," *Journal of Optics A: Pure and Applied Optics*, vol. 8, no. 4. pp. S87–S93, 2006.

[11] S. Shen, A. Narayanaswamy, and G. Chen, "Surface phonon polaritons mediated energy transfer between nanoscale gaps.," *Nano Lett.*, vol. 9, no. 8, pp. 2909–13, Aug. 2009.

[12] S. A. Maier, *Plasmonics: Fundamentals and applications*. Springer US, 2007.

[13] D. J. Griffiths, *Introduction to Electrodynamics*, Fourth. Pearson, 2013.

[14] J. D. Jackson, *Classical Electrodynamics*, Third., vol. 0. Wiley India Pvt. Limited, 2007.

[15] O. Benson, "Assembly of hybrid photonic architectures from nanophotonic constituents.," *Nature*, vol. 480, no. 7376, pp. 193–9, Dec. 2011.

[16] K. M. Van Vliet, "Derivation of the fluctuation-dissipation theorem," *Phys. Rev.*, vol. 109, no. 4, pp. 1021–1022, 1958.

[17] J. Weber, "Fluctuation dissipation theorem," *Phys. Rev.*, vol. 101, no. 6, pp. 1620–1626, 1956.

[18] R. Kubo, "The fluctuation-dissipation theorem," *Reports on Progress in Physics*, vol. 29, no. 1. pp. 255–284, 2002.

[19] C. Kittel, *Introduction to Solid State Physics*, vol. 11. Wiley, 2004.

[20] K. Joulain, R. Carminati, J.-P. Mulet, and J.-J. Greffet, "Definition and measurement of the local density of electromagnetic states close to an interface," *Phys. Rev. B*, vol. 68, no. 24, p. 245405, Dec. 2003.

[21] E. Rousseau, A. Siria, G. Jourdan, S. Volz, F. Comin, J. Chevrier, and J.-J. Greffet, "Radiative heat transfer at the nanoscale," *Nat. Photonics*, vol. 3, no. 9, pp. 514–517, Aug. 2009.

[22] L. Hu, A. Narayanaswamy, X. Chen, and G. Chen, "Near-field thermal radiation between two closely spaced glass plates exceeding Planck's blackbody radiation law," *Appl. Phys. Lett.*, vol. 92, no. 13, p. 133106, 2008.

[23] R. S. Ottens, V. Quetschke, S. Wise, a. a. Alemi, R. Lundock, G. Mueller, D. H. Reitze, D. B. Tanner, and B. F. Whiting, "Near-Field Radiative Heat Transfer between Macroscopic Planar Surfaces," *Phys. Rev. Lett.*, vol. 107, no. 1, p. 014301, Jun. 2011.

[24] B. Song, Y. Ganjeh, S. Sadat, D. Thompson, A. Fiorino, V. Fernández-Hurtado, J. Feist, F. J. Garcia-Vidal, J. C. Cuevas, P. Reddy, and E. Meyhofer, "Enhancement of near-field radiative heat transfer using polar dielectric thin films.," *Nat. Nanotechnol.*, vol. 10, no. 3, pp. 253–8, Mar. 2015.

[25] R. St-Gelais, B. Guha, L. Zhu, S. Fan, and M. Lipson, “Demonstration of Strong Near-Field Radiative Heat Transfer between Integrated Nanostructures.,” *Nano Lett.*, vol. 14, no. 12, pp. 6971–5, Dec. 2014.

[26] P. J. van Zwol, K. Joulain, P. Ben-Abdallah, and J. Chevrier, “Phonon polaritons enhance near-field thermal transfer across the phase transition of VO_{2},” *Phys. Rev. B*, vol. 84, no. 16, p. 161413, Oct. 2011.

[27] P. J. van Zwol, L. Ranno, and J. Chevrier, “Tuning Near Field Radiative Heat Flux through Surface Excitations with a Metal Insulator Transition,” *Phys. Rev. Lett.*, vol. 108, no. 23, p. 234301, Jun. 2012.

[28] V. B. Svetovoy, P. J. Van Zwol, and J. Chevrier, “Plasmons enhance near-field radiative heat transfer for graphene-covered dielectrics,” no. 2, pp. 1–5, 2012.

[29] R. Messina and P. Ben-Abdallah, “Graphene-based photovoltaic cells for near-field thermal energy conversion.,” *Sci. Rep.*, vol. 3, p. 1383, Jan. 2013.

[30] P. J. van Zwol, S. Thiele, C. Berger, W. a. de Heer, and J. Chevrier, “Nanoscale Radiative Heat Flow due to Surface Plasmons in Graphene and Doped Silicon,” *Phys. Rev. Lett.*, vol. 109, no. 26, p. 264301, Dec. 2012.

[31] O. Ilic, M. Jablan, J. D. Joannopoulos, I. Celanovic, H. Buljan, and M. Soljačić, “Near-field thermal radiation transfer controlled by plasmons in graphene,” *Phys. Rev. B*, vol. 85, no. 15, p. 155422, Apr. 2012.

[32] J. R. Barnes, R. J. Stephenson, C. N. Woodburn, S. J. O’Shea, M. E. Welland, T. Rayment, J. K. Gimzewski, and C. Gerber, “A femtojoule calorimeter using micromechanical sensors,” *Rev. Sci. Instrum.*, vol. 65, no. 12, pp. 3793–3798, Dec. 1994.

[33] A. Narayanaswamy and N. Gu, “Heat Transfer From Freely Suspended Bimaterial Microcantilevers,” *J. Heat Transfer*, vol. 133, no. 4, p. 042401, 2011.

[34] S. Shen, “Probing Extraordinary Nanoscale Energy Transfer Using Bimaterial Microcantilevers,” 2010.

[35] S. Shen, A. Narayanaswamy, S. Goh, and G. Chen, “Thermal conductance of bimaterial microcantilevers,” *Appl. Phys. Lett.*, vol. 92, no. 6, p. 063509, 2008.

[36] S. Biehs, P. Ben-Abdallah, F. S. S. Rosa, K. Joulain, and J.-J. Greffet, “Nanoscale heat flux between nanoporous materials,” *Opt. ...*, vol. 19 Suppl 5, no. May, pp. A1088–103, 2011.

[37] M. Francoeur, M. P. Mengüç, and R. Vaillon, "Near-field radiative heat transfer enhancement via surface phonon polaritons coupling in thin films," *Appl. Phys. Lett.*, vol. 93, no. 4, p. 043109, 2008.

[38] S. Basu and M. Francoeur, "Maximum near-field radiative heat transfer between thin films," *Appl. Phys. Lett.*, vol. 98, no. 24, p. 243120, Jun. 2011.

[39] C. R. Otey, W. T. Lau, and S. Fan, "Thermal Rectification through Vacuum," *Phys. Rev. Lett.*, vol. 104, no. 15, p. 154301, Apr. 2010.

[40] S. -a. Biehs and J.-J. Greffet, "Influence of roughness on near-field heat transfer between two plates," *Phys. Rev. B*, vol. 82, no. 24, p. 245410, Dec. 2010.

[41] J. Shi, P. Li, B. Liu, and S. Shen, "Tuning near field radiation by doped silicon," *Appl. Phys. Lett.*, vol. 102, no. 18, p. 183114, May 2013.

[42] B. Zeghbroeck, *Principles of Semiconductor Devices*. 2011.

[43] T. K. Gaylord, "A method for calculating Fermi energy and carrier concentrations in semiconductors," *Am. J. Phys.*, vol. 44, no. 4, p. 353, Apr. 1976.

[44] S. Rytov, *Theory of electric fluctuations and thermal radiation.* Bedford Mass.: Electronics Research Directorate Air Force Cambridge Research Center Air Research and Development Command U.S. Air Force., 1959.

[45] C. J. Fu and Z. M. Zhang, "Nanoscale radiation heat transfer for silicon at different doping levels," *Int. J. Heat Mass Transf.*, vol. 49, no. 9–10, pp. 1703–1718, May 2006.

[46] D. F. Edwards, *Handbook of optical constants of solids*, E. D. Pali. New York: Academic Press, 1998.

[47] and R. D. P. W. E. Beadle, J. C. C. Tsai, *Quick Reference Manual for Silicon Integrated Circuit Technology*. NewYork: John Wiley & Sons, 1985.

[48] A. Narayanaswamy, S. Shen, and G. Chen, "Near-field radiative heat transfer between a sphere and a substrate," *Phys. Rev. B*, vol. 78, no. 11, p. 115303, Sep. 2008.

[49] S. J. Byrnes, R. Blanchard, and F. Capasso, "Harvesting renewable energy from Earth's mid-infrared emissions.," *Proc. Natl. Acad. Sci. U. S. A.*, vol. 111, no. 11, pp. 3927–32, Mar. 2014.

[50] N. P. Padture, M. Gell, and E. H. Jordan, “Thermal barrier coatings for gas-turbine engine applications.,” *Science*, vol. 296, no. 5566, pp. 280–4, Apr. 2002.

[51] P. Ben-Abdallah and S.-A. Biehs, “Near-Field Thermal Transistor,” *Phys. Rev. Lett.*, vol. 112, no. 4, p. 044301, Jan. 2014.

[52] R. Siegel and J. Howell, *Thermal Radiation Heat Transfer*. London: Taylor & Francis, 2001.

[53] Z. Yu, N. P. Sergeant, T. Skauli, G. Zhang, H. Wang, and S. Fan, “Enhancing far-field thermal emission with thermal extraction.,” *Nat. Commun.*, vol. 4, p. 1730, Apr. 2013.

[54] S.-A. Biehs, E. Rousseau, and J.-J. Greffet, “Mesoscopic Description of Radiative Heat Transfer at the Nanoscale,” *Phys. Rev. Lett.*, vol. 105, no. 23, p. 234301, Dec. 2010.

[55] J. Shi, B. Liu, P. Li, L. Y. Ng, and S. Shen, “Near-Field Energy Extraction with Hyperbolic Metamaterials.,” *Nano Lett.*, vol. 15, no. 2, pp. 1217–1221, Jan. 2015.

[56] B. Guha, C. Otey, C. B. Poitras, S. Fan, and M. Lipson, “Near-field radiative cooling of nanostructures.,” *Nano Lett.*, vol. 12, no. 9, pp. 4546–50, Sep. 2012.

[57] Y. De Wilde, F. Formanek, R. Carminati, B. Gralak, P.-A. Lemoine, K. Joulain, J.-P. Mulet, Y. Chen, and J.-J. Greffet, “Thermal radiation scanning tunnelling microscopy.,” *Nature*, vol. 444, no. 7120, pp. 740–3, Dec. 2006.

[58] W. A. Challener, C. Peng, A. V. Itagi, D. Karns, W. Peng, Y. Peng, X. Yang, X. Zhu, N. J. Gokemeijer, Y.-T. Hsia, G. Ju, R. E. Rottmayer, M. A. Seigler, and E. C. Gage, “Heat-assisted magnetic recording by a near-field transducer with efficient optical energy transfer,” *Nat. Photonics*, vol. 3, no. 4, pp. 220–224, Mar. 2009.

[59] A. Poddubny, I. Iorsh, P. Belov, and Y. Kivshar, “Hyperbolic metamaterials,” *Nat. Photonics*, vol. 7, no. 12, pp. 948–957, Nov. 2013.

[60] J. Yao, “Light Propagation and Imaging in Indefinite Metamaterials,” 2010.

[61] J. Yao, Z. Liu, Y. Liu, Y. Wang, C. Sun, G. Bartal, A. M. Stacy, and X. Zhang, “Optical negative refraction in bulk metamaterials of nanowires.,” *Science*, vol. 321, no. 5891, p. 930, Aug. 2008.

[62] F. J. Garcia-Vidal, L. Martín-Moreno, and J. B. Pendry, "Surfaces with holes in them: new plasmonic metamaterials," *J. Opt. A Pure Appl. Opt.*, vol. 7, no. 2, pp. S97–S101, Feb. 2005.

[63] Y. Guo, C. L. Cortes, S. Molesky, and Z. Jacob, "Broadband super-Planckian thermal emission from hyperbolic metamaterials," *Appl. Phys. Lett.*, vol. 101, no. 13, p. 131106, Sep. 2012.

[64] B. Liu and S. Shen, "Broadband near-field radiative thermal emitter/absorber based on hyperbolic metamaterials: Direct numerical simulation by the Wiener chaos expansion method," *Phys. Rev. B*, vol. 87, no. 11, p. 115403, Mar. 2013.

[65] S. -a. Biehs, M. Tschikin, and P. Ben-Abdallah, "Hyperbolic Metamaterials as an Analog of a Blackbody in the Near Field," *Phys. Rev. Lett.*, vol. 109, no. 10, p. 104301, Sep. 2012.

[66] G. Shvets, S. Trendafilov, J. Pendry, and A. Sarychev, "Guiding, Focusing, and Sensing on the Subwavelength Scale Using Metallic Wire Arrays," *Phys. Rev. Lett.*, vol. 99, no. 5, p. 053903, Aug. 2007.

[67] S. W. Lin, S. C. Chang, R. S. Liu, S. F. Hu, and N. T. Jan, "Fabrication and magnetic properties of nickel nanowires," *J. Magn. Magn. Mater.*, vol. 282, pp. 28–31, Nov. 2004.

[68] J. Dini and S. Dexter, "Electrodeposition of copper," in *Modern Electroplating*, Fifth., John Wiley & Sons, Inc., 2010, pp. 33–78.

[69] K. Nielsch, F. Müller, A.-P. Li, and U. Gösele, "Uniform Nickel Deposition into Ordered Alumina Pores by Pulsed Electrodeposition," *Adv. Mater.*, vol. 12, no. 8, pp. 582–586, Apr. 2000.

[70] M. E. Toimil-Molares, "Characterization and properties of micro- and nanowires of controlled size, composition, and geometry fabricated by electrodeposition and ion-track technology.," *Beilstein J. Nanotechnol.*, vol. 3, no. 1, pp. 860–83, Jan. 2012.

[71] R.-L. Zong, J. Zhou, Q. Li, B. Du, B. Li, M. Fu, X.-W. Qi, L.-T. Li, and S. Buddhudu, "Synthesis and Optical Properties of Silver Nanowire Arrays Embedded in Anodic Alumina Membrane," *J. Phys. Chem. B*, vol. 108, no. 43, pp. 16713–16716, Oct. 2004.

[72] N. Kanani, *Electroplating- basic principles, processes, and practice*. 2004.

[73] R. K. Singh and R. Bajaj, "Advances in Chemical-Mechanical Planarization," *MRS Bull.*, vol. 27, no. 10, pp. 743–751, Jan. 2011.

[74] *Chemical-mechanical planarization of semiconductor materials*. Springer, 2004.

[75] A. E. Miller, P. B. Fischer, A. D. Feller, and T. N. Andryushchenko, *Chemical-mechanical planarization for semiconductors*. 2003.

[76] *Chemical-mechanical planarization : symposium held April 22-24, 2003, San Francisco, California, U.S.A.* Materials Research Society, 2003.

[77] J. M. Steigerwald, S. P. Murarka, and R. J. Gutmann, *Chemical Mechanical Planarization of Microelectronic Materials*. John Wiley & Sons, 2008.

[78] J. M. Steigerwald, "Chemical mechanical polish: The enabling technology," in *Technical Digest - International Electron Devices Meeting, IEDM*, 2008.

[79] Y. L. Wang, W. T. Tseng, and S. C. Chang, "Chemical-mechanical polish of aluminum alloy thin films: Slurry chemistries and polish mechanisms," *Thin Solid Films*, vol. 474, no. 1–2. pp. 36–43, 2005.

[80] D. G. Thakurta, C. L. Borst, D. W. Schwendeman, R. J. Gutmann, and W. N. Gill, "Pad porosity, compressibility and slurry delivery effects in chemical-mechanical planarization: modeling and experiments," *Thin Solid Films*, vol. 366, no. 1–2, pp. 181–190, 2000.

[81] J. Yao, Y. Wang, K.-T. Tsai, Z. Liu, X. Yin, G. Bartal, A. M. Stacy, Y.-L. Wang, and X. Zhang, "Design, fabrication and characterization of indefinite metamaterials of nanowires.," *Philos. Trans. A. Math. Phys. Eng. Sci.*, vol. 369, no. 1950, pp. 3434–46, Sep. 2011.

[82] R. Chen, M.-C. Lu, V. Srinivasan, Z. Wang, H. H. Cho, and A. Majumdar, "Nanowires for enhanced boiling heat transfer.," *Nano Lett.*, vol. 9, no. 2, pp. 548–53, Feb. 2009.

[83] H. Morawitz and M. R. Philpott, "Coupling of an excited molecule to surface plasmons," *Phys. Rev. B*, vol. 10, no. 12, pp. 4863–4868, 1974.

[84] B. Liu and S. Shen, "Broadband near-field radiative thermal emitter/absorber based on hyperbolic metamaterials: Direct numerical simulation by the Wiener chaos expansion method," *Phys. Rev. B*, vol. 87, no. 11, p. 115403, Mar. 2013.

[85] H. N. S. Krishnamoorthy, Z. Jacob, E. Narimanov, I. Kretzschmar, and V. M. Menon, "Topological Transitions in Metamaterials," *Science (80-.).*, vol. 336, no. 6078, pp. 205–209, 2012.

[86] S.-A. Biehs, D. Reddig, and M. Holthaus, “Thermal radiation and near-field energy density of thin metallic films,” *Eur. Phys. J. B*, vol. 55, no. 3, pp. 237–251, Feb. 2007.

[87] S.-A. Biehs, “Thermal heat radiation, near-field energy density and near-field radiative heat transfer of coated materials,” *Eur. Phys. J. B*, vol. 58, no. 4, pp. 423–431, Sep. 2007.

[88] M. Francoeur, M. P. Mengüç, and R. Vaillon, “Spectral tuning of near-field radiative heat flux between two thin silicon carbide films,” *J. Phys. D. Appl. Phys.*, vol. 43, no. 7, p. 075501, Feb. 2010.

[89] M. Francoeur, M. P. Mengüç, and R. Vaillon, “Spectral tuning of near-field radiative heat flux between two thin silicon carbide films,” *J. Phys. D. Appl. Phys.*, vol. 43, no. 7, p. 075501, Feb. 2010.

[90] O. D. Miller, S. G. Johnson, and A. W. Rodriguez, “Effectiveness of Thin Films in Lieu of Hyperbolic Metamaterials in the Near Field,” *Phys. Rev. Lett.*, vol. 112, no. 15, p. 157402, Apr. 2014.

[91] Z. Wang, T. S. Luk, Y. Tan, D. Ji, M. Zhou, Q. Gan, and Z. Yu, “Tunneling-enabled spectrally selective thermal emitter based on flat metallic films,” *Appl. Phys. Lett.*, vol. 106, no. 10, p. 101104, 2015.

[92] M. Ohtsu, *Principles of Nanophotonics*. Taylor & Francis, 2008.

[93] W. Cai and T. Yu, “Fast calculations of dyadic Green’s functions for electromagnetic scattering in a multilayered medium,” *J. Comput. Phys.*, vol. 165, no. 1, pp. 1–21, 2000.

[94] D. Whittaker and I. Culshaw, “Scattering-matrix treatment of patterned multilayer photonic structures,” *Phys. Rev. B*, vol. 60, no. 4, pp. 2610–2618, 1999.

[95] M. Francoeur, M. Pinar Mengüç, and R. Vaillon, “Solution of near-field thermal radiation in one-dimensional layered media using dyadic Green’s functions and the scattering matrix method,” *J. Quant. Spectrosc. Radiat. Transf.*, vol. 110, no. 18, pp. 2002–2018, 2009.

[96] S. M. George, “Atomic layer deposition: An overview,” *Chem. Rev.*, vol. 110, no. 1, pp. 111–131, 2010.

[97] M. Leskelä and M. Ritala, “Atomic layer deposition (ALD): From precursors to thin film structures,” *Thin Solid Films*, vol. 409, no. 1, pp. 138–146, 2002.

[98] P. . Kelly and R. . Arnell, “Magnetron sputtering: a review of recent developments and applications,” *Vacuum*, vol. 56, no. 3, pp. 159–172, 2000.

[99] M. Kawamura, T. Mashima, Y. Abe, and K. Sasaki, “Formation of ultra-thin continuous Pt and Al films by RF sputtering,” *Thin Solid Films*, vol. 377–378, pp. 537–542, 2000.

[100] T. Michely and G. Comsa, “Temperature dependence of the sputtering morphology of Pt(111),” *Surface Science Letters*, vol. 256, no. 3. p. A537, 1991.

[101] G. S. Higashi, R. S. Becker, Y. J. Chabal, and a J. Becker, “Comparison of Si(111) surfaces prepared using aqueous solutions of NH[sub 4]F versus HF,” *Appl. Phys. Lett.*, vol. 58, no. 15, pp. 1656–1658, 1991.

[102] M. Morita, T. Ohmi, E. Hasegawa, M. Kawakami, and M. Ohwada, “Growth of native oxide on a silicon surface,” *J. Appl. Phys.*, vol. 68, no. 3, pp. 1272–1281, 1990.

[103] H. Angermann, T. Dittrich, and H. Flietner, “Investigation of native-oxide growth on HF-treated Si(111) surfaces by measuring the surface-state distribution,” *Appl. Phys. A*, vol. 59, no. 2, pp. 193–197, 1994.

[104] M. Yasaka, “X-ray thin-film measurement techniques,” *V. X-ray reflectivity Meas. Rigaku J.*, 2010.

[105] M. H. Kryder, E. C. Gage, T. W. Mcdaniel, W. a. Challener, R. E. Rottmayer, G. Ju, Y. T. Hsia, and M. F. Erden, “Heat assisted magnetic recording,” *Proc. IEEE*, vol. 96, no. 11, pp. 1810–1835, 2008.

[106] W. a. Challener, C. Peng, a. V. Itagi, D. Karns, W. Peng, Y. Peng, X. Yang, X. Zhu, N. J. Gokemeijer, Y.-T. Hsia, G. Ju, R. E. Rottmayer, M. a. Seigler, and E. C. Gage, “Heat-assisted magnetic recording by a near-field transducer with efficient optical energy transfer,” *Nat. Photonics*, vol. 3, no. 5, pp. 303–303, 2009.